Technische Universität München
TUM School of Natural Sciences

Search for Supernova R-process Actinides in Fossilized Reservoirs

Iuliana Madalina Stanciu

Vollständiger Abdruck der von der TUM School of Natural Sciences der Technischen Universität München zur Erlangung des akademischen Grades einer

Doktorin der Naturwissenschaften (Dr. rer. nat.)

genehmigten Dissertation.

Vorsitz:

Prof. Dr. Nora Brambilla

Prüfende der Dissertation:

1. Prof. Dr. Elisa Resconi
2. Prof. Dr. Laura Fabbietti

Die Dissertation wurde am 25.11.2022 bei der Technischen Universität München eingereicht und durch die TUM School of Natural Sciences am 15.12.2022 angenommen.

To SHAWN

Thesis Advisor: Prof. Shawn Bishop Iuliana Madalina Stanciu

Abstract

A recently time-resolved, ^{60}Fe signal, has been putatively assigned to Core Collapse Supernova (CCSN) origin. That the ^{60}Fe signal is now time-resolved, with an onset beginning around 2.6 Ma, ending around 1.6 Ma, and peaking at 2.1 Ma, allows for targeted choice, in the same geological time domain, of reservoirs suited to include r-process only isotopes.

Within the framework of this thesis, we search for ^{244}Pu coincident in time with ^{60}Fe in 2Ma old samples collected from Turkana Basin, Kenya. The samples are carbonate rich fossilized reservoirs formed through biological activity, in which the mass concentration of actinides we found to be 10^3-10^2 times higher than that within the aquatic environment in which these fossilized reservoirs formed. The geological materials were chemically processed and searched for ^{244}Pu with the most sensitive method currently available, Accelerator Mass Spectrometry (AMS).

During the advance of the AMS measurements, the results revealed the importance of studying the anthropogenic contribution of Plutonium isotopes, because, in terms of AMS it is everywhere in the environment. Plutonium produced during the nuclear weapon tests can be used to determine a biological uptake factor of Plutonium for the old stromatolites by deriving it from modern stromatolites, that were growing around 1960 in Argentina. Together with the stromatolites, a sediment core was sampled from sallow lacustrine environments within the Argentinian Andes and analysed by AMS, and it was found a fluence for anthropogenic ^{239}Pu of 172.4 ± 17.1 (10^7 atoms/cm^2).

To extract Pu from large carbonate samples complex chemical procedures were developed, starting from a few kg of material and obtaining a final target material in the form of a mixture of iron oxide and niobium that has a mass of around 5mg, the final concentration enhancement is in the order of $\sim 10^5$. Additionally, it was proved the 0 background when analysing mass 244 by Accelerator Mass Spectrometry and a total measurement efficiency of 10^{-4}, meaning that the minimum quantity of ^{244}Pu detectable is $\sim$10 atto-grams (10^{-17}g).

Nonetheless, when processing big quantities of Turkana stromatolites with an age of 2-1.9Ma, high count rates of ^{239}Pu compared to ^{244}Pu are obtained, and any extra-terrestrial ^{244}Pu gets diluted and therefore lost. Most of the results were obtained using the 1MV Accelerator from HVE installed at IFIN-HH, Romania but also, for confirming some aspects important for the measurement, experiments were carried out at CIRCE, Italy by using the 3MV Accelerator from NEC.

For one sample that was cleaned using a ultrasound bath with ultrapure water and its surface was leached away, an isotopic ratio ^{244}Pu/^{239}Pu of $3.84^{+9.07}_{-3.15}(\cdot 10^{-3})$ was obtained, while the ratio obtained for a stromatolite of Holocene age, (an age well outside the Supernova window) is $0.83^{+0.81}_{-0.53}(\cdot 10^{-4})$. When comparing these results, the Turkana stromatolite shows an excess of ^{244}Pu that can be interpreted as the incorporation of extra-terrestrial material from core-collapse SN, the excess being coincident in time with the already well-known, ^{60}Fe signal.

Keywords: ^{244}Pu, r-process, Stromatolite, AMS.

Thesis Advisor: Prof. Shawn Bishop Iuliana Madalina Stanciu

Zusammenfassung:

Ein kürzlich zeitaufgelöstes ^{60}Fe-Signal wurde vermutlich dem Ursprung einer Kernkollaps-Supernova (CCSN) zugeordnet. Die Tatsache, dass das ^{60}Fe-Signal nun zeitaufgelöst ist, mit einem Beginn um 2.6 Ma, einem Ende um 1.6 Ma und einem Höhepunkt bei 2.1 Ma, ermöglicht eine gezielte Auswahl von Reservoiren im gleichen geologischen Zeitbereich, die geeignet sind, nur r-Prozess-Isotope zu enthalten.

Im Rahmen dieser Arbeit suchen wir nach ^{244}Pu, das zeitlich mit ^{60}Fe zusammenfällt. 2Ma alte Proben wurden im Turkana-Becken in Kenia gesammelt. Bei den Proben handelt es sich um fossile Reservoirs, die durch biologische Aktivität entstanden sind und in denen die Massenkonzentration der Aktiniden 10^3-10^2 Mal höher ist als in dem Wasserbecken, in dem sich diese fossilen Reservoirs gebildet haben, wobei wir davon ausgehen, dass die Geologie des Gebiets in den letzten 2 Millionen Jahren unverändert geblieben ist. Die geologischen Materialien wurden chemisch aufbereitet und mit der empfindlichsten derzeit verfügbaren Methode, der Beschleuniger-Massenspektrometrie (AMS), auf ^{244}Pu untersucht.

Im Verlauf der AMS-Messungen wurde deutlich, wie wichtig es ist, den anthropogenen Beitrag von Plutoniumisotopen zu untersuchen, denn im Sinne der AMS ist es überall in der Umwelt vorhanden. Das während der Kernwaffentests produzierte Plutonium kann zur Bestimmung eines biologischen Aufnahmefaktors für Plutonium für die fossilen Stromatolithen verwendet werden, indem man ihn von modernen Stromatolithen ableitet, die in den argentinischen Anden beprobt wurden. Zusammen mit den Stromatolithen wurde ein Sedimentkern entnommen und mittels AMS analysiert, wobei eine Fluenz für anthropogenes ^{239}Pu von 172.4 ± 17.1 ($\cdot 10^7$ Atome/cm^2) festgestellt wurde.

Um Pu aus großen Karbonatproben zu extrahieren, wurden komplexe chemische Verfahren entwickelt, bei denen ausgehend von einigen Kilogramm Material ein endgültiges Zielmaterial in Form eines Gemischs aus Eisenoxid und Niob mit einer Masse von etwa 5 mg erhalten wird, wobei die endgültige Konzentrationserhöhung in der Größenordnung von $\sim 10^5$ liegt. Darüber hinaus wurde bei der Analyse der Masse 244 mittels Beschleuniger-Massenspektrometrie ein Hintergrund von 0 und eine Gesamteffizienz der Messung von 10^{-4}

nachgewiesen, was bedeutet, dass die minimal nachweisbare Menge von ^{244}Pu ~10 Atto-Gramm (10^{-17}g) beträgt.

Bei der Verarbeitung großer Mengen von Turkana-Stromatolith mit einem Alter von 2-1.9 Ma werden jedoch hohe Zählraten von ^{239}Pu im Vergleich zu ^{244}Pu erzielt, und jegliches extraterrestrische ^{244}Pu wird verdünnt und geht daher verloren. Die meisten Ergebnisse wurden mit dem 1MV-Beschleuniger von HVE am IFIN-HH in Rumänien erzielt, aber zur Bestätigung einiger für die Messung wichtiger Aspekte wurden auch Experimente am CIRCE in Italien mit dem 3MV-Beschleuniger von NEC durchgeführt.

Bei einer Probe, die in einem Ultraschallbad mit Reinstwasser gereinigt und deren Oberfläche ausgelaugt wurde, ergab sich ein Isotopenverhältnis ^{244}Pu/^{239}Pu von $3.84^{+9.07}_{-3.15}(\cdot 10^{-3})$ erhalten, während das Verhältnis für den holozänen Stromatolithen, dessen Alter weit außerhalb des Supernova-Fensters liegt, $0.83^{+0.81}_{-0.53}(\cdot 10^{-4})$ beträgt. Beim Vergleich dieser Ergebnisse zeigt der Turkana-Stromatolith einen Überschuss an ^{244}Pu, der als Einlagerung von extraterrestrischem Material aus Kernkollaps-SN interpretiert werden kann, wobei der Überschuss zeitlich mit dem bereits bekannten ^{60}Fe-Signal zusammenfällt.

Schlüsselwörter: ^{244}Pu, r-Prozess, Stromatolith, AMS.

Contents

1. Introduction

The nucleosynthesis of the heavy elements takes place in nature in explosive environments in stars. The precise sites are still unknown and finding where it occurs is one of the most outstanding questions to be answered in nuclear astrophysics. The mechanism by which at least half of the elemental abundances greater than iron are produced in the universe is the rapid neutron capture process (r-process).

Present theoretical candidate sites are core collapse supernovae (CCSNe) (Sukhbold et al., 2016) and binary neutron star mergers (Hotokezaka et al., 2015; Cowperthwaite et al., 2017), but also, other more exotic scenarios are investigated, like magneto-rotationally driven (MHD) supernovae (Winteler, 2012), collapsar disk winds that is formed around a massive progenitor that undergo collapse (McLaughlin and Surman 2005; Siegel et al., 2018), another scenario within the scientific literature is that there can be a primordial black hole captured by a neutron star (Fuller et al., 2017).

Even though GW170817 and the associated kilonova from a neutron-star merger were detected in August 2017 (Abott et al., 2017), the sites of r-process remain an open question, including core-collapse supernovae or special kinds of it, because as discussed in (Kabayashi, Karakas & Lugaro, 2020) it is not possible to explain the evolution of r-process elements by considering only Neutron Star Mergers, therefore the motivation to search for supernova-produced actinides still exist.

The publications of Korschinek et al. (1996) and Ellis et al. (1996) pave the way for "Supernova Archaeology" (credit to Brian Field) where several cosmogenic radionuclides like ^{10}Be, ^{26}Al, ^{36}Cl, ^{53}Mn, ^{60}Fe, and ^{59}Ni, as well as the longer-lived ^{129}I, ^{146}Sm, and ^{244}Pu, could be used to identify a nearby supernova by searching them in terrestrial archives.

In the last decades, the research activities have been focused on the ^{60}Fe radioisotope, which was found on earth between 2.6 and 1.6Ma. ^{60}Fe signal has been putatively assigned to CCSN origin and it was found by investigating various types of reservoirs, such as deep-sea ferromanganese crust (Knie et al., 1999), magnetofossils in two Pacific Ocean sediment cores (Ludwig et al., 2016), ocean sediments, crust, and nodules (Wallner et al., 2016). Additionally, lunar regolith (Fimiani et al., 2016) was found to contain the radioactive isotope of iron, and

freshly synthesized ^{60}Fe has been found in cosmic ray mass spectrum (Binns et al., 2016) and in recent layers of Antarctic snow (Koll et al. 2019).

Given that the ^{60}Fe signal is now time resolved, peaking at 2.1 Myr ago, allows for targeted selection, within the right geological time, of reservoirs suited to contain r-process only isotopes. A finding on Earth of ^{244}Pu coincident in time, at 2 Myr ago, with previously discovered supernova-produced ^{60}Fe would show that the r-process occurs in CCSNe.

Goriely and Janka (2016) presents supernova neutrino wind calculations, made to fit the solar r-process abundance distribution and the results suggest a range of ^{244}Pu yields of $2.37 \cdot 10^{-8} M_{\odot}$ to $2.75 \cdot 10^{-7} M_{\odot}$. The ^{60}Fe yield, averaged over progenitor masses, from the supernova models presented in Sukhbold et al., (2015) is $2.70 \cdot 10^{-5} M_{\odot}$. From these model calculations, a theoretical range in the ratio $^{244}\mathrm{Pu}/^{60}\mathrm{Fe} = [8.8 \cdot 10^{-4}, 1.0 \cdot 10^{-2}]$ is derived.

Fimiani et al. (2016), Wallner et al. (2016) and Ludwig et al. (2016) found a ^{60}Fe terrestrial fluence ϕ_{60} in the range of $4.0 \cdot 10^{5}$ and $3.5 \cdot 10^{7}$ $atoms/cm^2$. By using this information, it can be inferred for the terrestrial fluence of ^{244}Pu an upper limit of $35 \cdot 10^{4}$ and a lower limit of 35 $atoms/cm^2$.

Therefore, the scientific challenge is daunting as the production factor of ^{244}Pu compared to ^{60}Fe could be 3 to 4 orders smaller. Means must be found to overcome this difficulty, and this work makes the case that such a means has been found in the form of a unique biologically formed reservoir in which a ^{244}Pu mass concentration enhancement larger than these orders should have occurred.

The reservoirs targeted are stromatolites, which are aquatic colonies of bacteria which thrived in the past and have grown in high-salinity shallow lakes. The shapes they form tend to be spheroids and mats, in which layers of bacteria grow, creating a macroscopically sized object. The bacteria within these objects, through means of chemical reactions, can precipitate dissolved metals out of solution from the water. Contemporary stromatolites can mass-concentrate the rare earth elements and actinides up to 4 to 6 orders over what was in the water (Anderson et al., 2003). The precipitate formed by the bacteria has a mass concentration of these elements up to 1 million times higher than the mass concentration that was in the water from which the bacteria got these elements.

To overcome the otherwise daunting reduction in ^{244}Pu production factor relative to ^{60}Fe in CCSN models, we intended to exploit this feature of past microbial activity by performing a search for ^{244}Pu by Accelerator Mass Spectrometry in 2-million-year-old fossilized stromatolites sampled from the

Turkana Basin, Kenya and in 4 -million-year-old fossilized stromatolites sampled from the Atacama Desert, Chile.

Since it is expected extremely low concentration when investigating such peculiar radioisotope an ultrasensitive detection method must be used. Accelerator mass spectrometry is the most suitable technique for attempting the measurement for the detection of trace amounts of long-lived radioisotopes. Because when measuring actinides by AMS, it suffices to determine the mass of a nuclide to identify it, since isobars with comparably long lifetimes that interfere with the detection of the other element rarely occur and the use of a tandem accelerator and the formation of positive charge states of the ions where no molecules exist is ideally suited for actinide measurements.

Regrettably, for many reasons, plutonium isotopes were also produced on earth by mankind by developing and testing the nuclear weapons. The main source of anthropogenic plutonium in the environment was the atmospheric nuclear tests, conducted primarily in the northern hemisphere between 1945 and 1980. The isotopes mainly produced were: ^{238}Pu ($T_{1/2}$ = 87.7 a), ^{239}Pu ($T_{1/2}$ = 24110 a), ^{240}Pu ($T_{1/2}$ = 6564 a), ^{241}Pu ($T_{1/2}$ = 14.29 a), ^{242}Pu ($T_{1/2}$ =3.75·10^{5}a) and ^{244}Pu ($T_{1/2}$=80.6·10^{6}a). After ^{239}Pu, the most abundant isotope produced is ^{240}Pu because it is next on the mass scale. These two isotopes are the most studied when is investigated the nuclear pollution in environment. In this work, they were analysed together with the ^{244}Pu isotope, to quantify the anthropogenic contamination of the fossilised materials used, because of their permanent exposure on the Earth surface. Given their different half-lives, only the isotope with mass 244 is common to both events, nuclear bomb tests and, possibly, core collapse supernovae from 2.6-1.6Ma, while $^{239 \text{ and } 240}$Pu (if produced) already decayed to undetectable levels.

All plutonium determinations were conducted using 1 MV Tandetron Accelerator System installed at the Horia Hulubei National Institute for R&D in Physics and Nuclear Engineering (IFIN-HH) in Bucharest, Romania (Stan-Sion et al., 2015; Stanciu et al., 2017; Enachescu et al., 2018, 2019; Pacesila et al., 2020) and later during the project, experiments were performed also at the CIRCE Laboratory, Caserta, Italy (De Cesare et al., 2010, 2013, 2015) using the 3 MV AMS Tandem System.

The outline of the thesis is as follows. In chapter 2 the physical principles of synthesis and transport of actinides from CCSNe and the role of ^{244}Pu in astrophysics, leading to its incorporation into fossilised reservoirs like stromatolites or microbialites are presented. In the same chapter the description

of these biologically formed materials and the description of the geological setting of the places from where they were sampled are given. In chapter 3 are described Inductively Coupled Plasma Mass Spectrometry measurements and the results about the concentration of rare earth elements and natural actinides like thorium and uranium in the targeted samples. These measurements check if our samples have mass concentration enhancement relative to water samples from the same geological areas. In chapter 4, the chemical procedures that were developed specially for ^{244}Pu AMS measurements are described and discussed in terms of chemical yields. An extensive description of the AMS technique and system are presented in chapter 5 together with methodological and technical details involved in plutonium determination. Afterward, the AMS results, their interpretation, and an outlook on planned further measurements are explained in Chapter 6, followed by a short conclusion in chapter 7.

2. From Supernovae to stromatolites

The means of producing new nuclei in the universe are called nucleosynthesis. If any new synthesized live ^{244}Pu arrived on earth, it would have travelled a long way through interstellar space until its arrival on earth. Here it would land directly on geological strata or would have gotten incorporated into carbonaceous structures by alive special algae, structures that over millions of years are transformed into fossilized reservoirs. Investigating this journey requires a multidisciplinary approach that includes information from various fields like nuclear and atomic physics, astrophysics, geology, biology, and chemistry.

2.1. Stellar Nucleosynthesis

The first half of the last century was crucial for the interdisciplinary branch of nuclear physics that is called nuclear astrophysics and the review papers, which are explaining the Hydrogen and Helium quiescent and hot burning, and the nucleosynthesis beyond Iron, were published in 1957 by E. M. Burbidge, G. R. Burbidge, W. A. Fowler, F. Hoyle (1957) and independently by A. G. W. Cameron (1957) are considered the basis of modern nuclear astrophysics. These authors stated nuclear reactions are responsible for both energy production and the creation of the elements and they already summarize all the work that was done before as they highlighted the main environments for nucleosynthesis:

- Cosmological nucleosynthesis: creation in the Big Bang of H, He and Li,
- Stellar nucleosynthesis
    - Synthesis of elements by fusion in stars,
    - Explosive nucleosynthesis: synthesis of elements by neutron and proton capture reactions in supernovae,
    - Galactic nucleosynthesis: synthesis of elements by cosmic ray spallation reactions.

Figure 2.1 (taken from Kobayashi et al., 2020) shows the sources of elements in the Solar System, each element being color-coded by the relative contribution of each source. In the same paper is again stated the origin of H, He and Li as being the Big Bang.

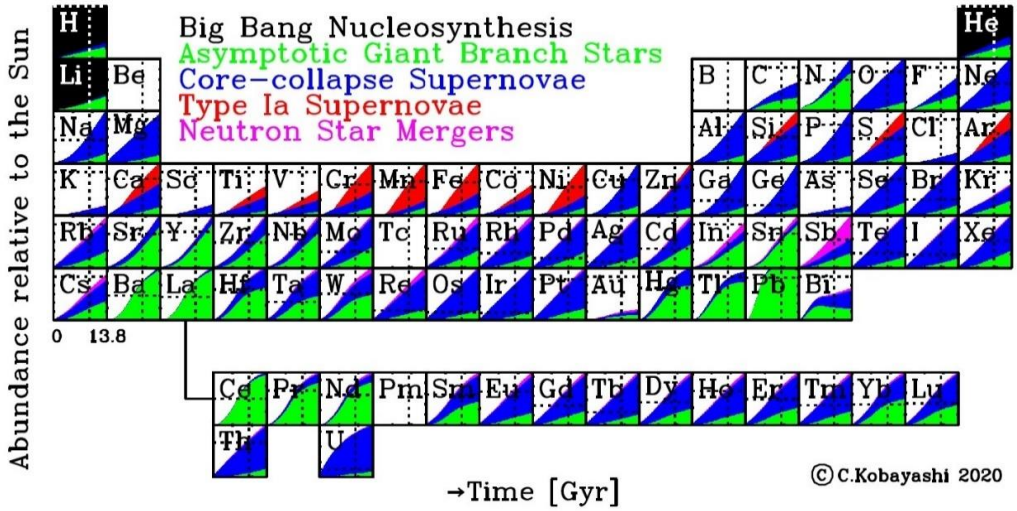

Figure 2.1. Source contributions for the nucleosynthesis of elements. Big Bang nucleosynthesis (black), AGB stars (green), core-collapse supernovae (blue), SNe Ia (red) and NSMs (magenta) (taken from Kobayashi et al., 2020)

Regarding the source marked with blue, the core-collapse supernovae is including SNe II - normal core-collapse supernovae–explosion of massive stars ($M > 10\ M_{\odot}$), HNe – hypernovae with $M \geq 20 M_{\odot}$, ECSNe - electron-capture supernovae the result of the explosion of high-mass super-AGB stars, and MRSNe - magneto-rotational supernovae.

In connection with the investigation of stellar environments, astrophysics is seeking to explain the shape of the abundance curve of elements in our solar system, which is presented in figure 2.2 (Cameron, 1982). The first point that can be noticed is that the Big Bang nucleosynthesis did not go beyond lithium. This is essentially because of the lack of stable nuclei with mass number 5 or 8 and also because of the rapid decrease in temperature and density that didn't allow for the nucleosynthesis to go on after the first 10 minutes.

The stellar of nucleosynthesis started after about 400Ma, when massive stars were formed by action of gravity. The starting point of stellar nucleosynthesis is the production of "metals". The 3 alpha ($3\alpha \rightarrow {}^{12}C$) process is the most probable scenario.

Starting from carbon, nucleosynthesis takes place in stars and staggering in abundances was observed so that was deeply studied during the beginning of the last century and now it became a rule that is called Oddo-Harkins rule. More specific it was found that from carbon the elements are produced by alpha particles capture and ion-ion fusion and we have an alternating larger abundance of even nuclei with respect to the odd ones. This behaviour is essentially connected to the pairing in the nuclei, which makes even Z nuclei more stable.

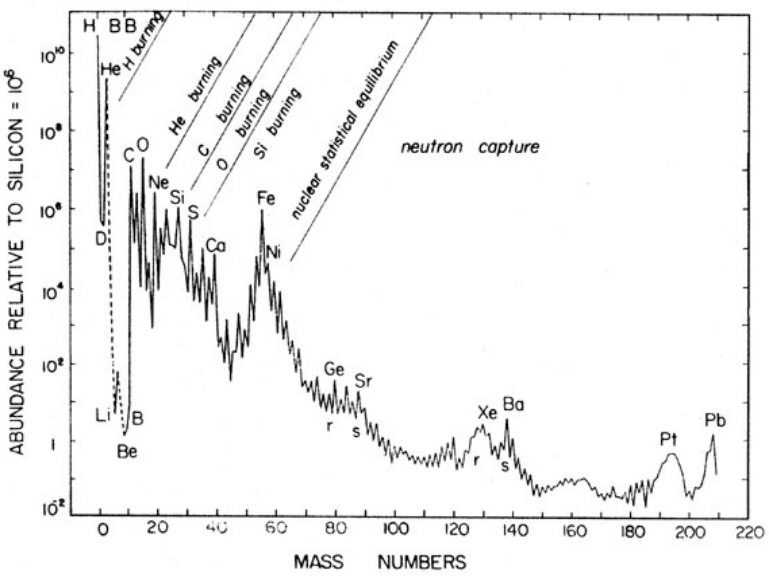

Figure 2.2. Abundance Curve of elements in the Solar system as a function of atomic number (Cameron, 1982)

Another specific feature of the abundance curve is that peaks are presented in correspondence with the magic numbers that are nuclei with a certain combination of the value of Z (protons) and N (neutrons) and this happens clearly for oxygen, calcium, iron. Beyond iron, something else happens and the concentrations drop abruptly because of the largest binding energy for this nucleus, such that all the reactions which take place in stars up to iron produce energy. After iron is produced, there cannot be added more alpha particles or protons to the seed nuclei or ion-ion fusion, therefore other nuclear processes are taking place to build up the heavy elements, these are neutron capture processes.

2.1.1. Neutron capture processes and ^{244}Pu

Elements heavier than the iron group are no longer formed by fusion in stars since iron has the maximum binding energy per nucleon. Therefore, energy is no longer gained in the fusion of two lighter nuclides into a nucleus heavier than iron.

The synthesis of all of the heavier elements is based on the addition of neutrons to existing nuclei to form more neutron-rich isotopes: in the s-process, the slow capture of neutrons and in the r-process, the rapid capture of neutrons. A neutron capture leads to an unstable isotope that can either β (beta) decay or capture another neutron, depending on the specific conditions.

The s-process is a process that happens in medium conditions with neutron densities ranging from 10^6 to 10^{11} neutrons/cm^3 and neutron capture timescales up to thousands of years (Iliadis, C., 2007).

If a nuclide formed in this way is unstable, because of the low neutron flux, the newly formed nuclei decay back to a stable nucleus and it usually takes place before further neutrons are attached to the radionuclide. This process keeps the nucleosynthesis close to the valley of stability. As a result, a neutron in the nucleus is converted into a proton, and an element with a higher atomic number is created in which the accumulation of further neutrons can continue. In addition to the fusion processes during slow neutron capture at stable nuclei, half of heavy elements, including lead and bismuth, are produced in the stars. The other half is produced in r-process. At high neutron density repeated neutron capture is more probable than β^- decay.

The production of actinides, more specifically of the isotope of interest for this work–^{244}Pu, this process–slow capture of neutrons is not suitable, because the elements between bismuth and thorium decay too quickly via β^- decay. Thus, a higher neutron flux is required for the production of actinides than is available during normal stellar burning, the conditions needed are met under extreme conditions with high temperatures in the order of Giga Kelvin and neutron densities up to 10^{22} neutrons/cm^3 (Iliadis, C., 2007), given these conditions, the rapid neutron capture proceeds further from the stability valley, allowing the synthesis of heavier radioisotopes before their decay to stable nuclides.

As shown by Ratzel et al. (2004), the s-process proceeds and ends in lead 208 (figure 2.3) so the s-process cannot reach the actinides region, consequently producing actinides involves the rapid neutron capture.

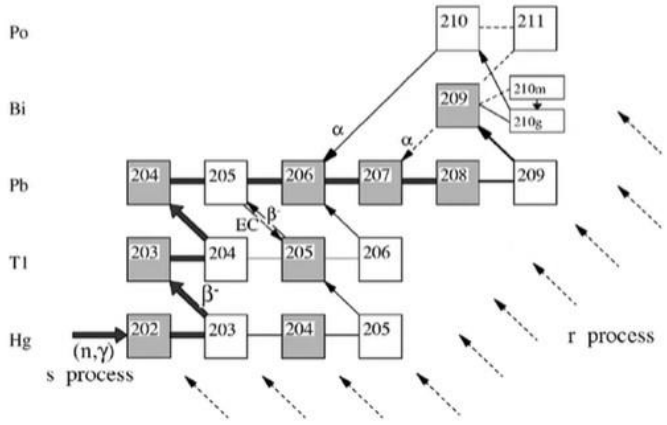

Figure 2.3. The s and r processes paths along the valley of stability (taken from Ratzel et al., 2004)

In scientific literature there are profs of r-process elements outside Earth. For example, Donelly et al. (2012) revealed the detection of Pu and Cm in cosmic rays by analysing the stacks of Lexan sheets from satellite missions.

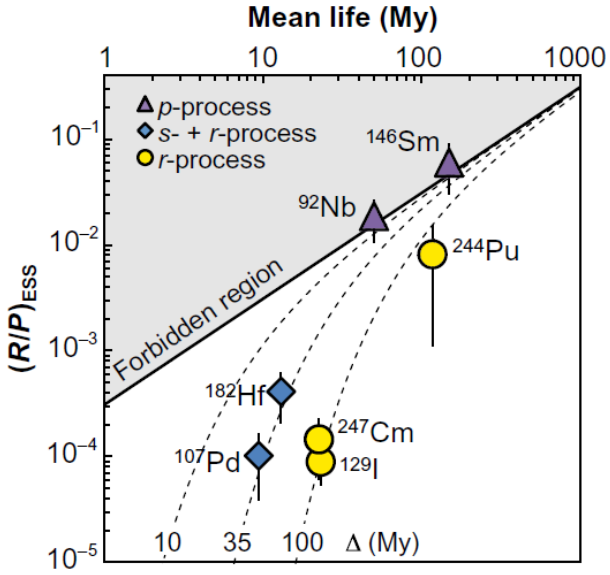

Figure 2.4. Meteoritic abundance ratios of extinct radionuclides to stable nuclides produced by the same process (taken from Tissot et al., 2016)

In another case, an excess of uranium 235 which is a trace of ^{247}Cm (half-life 15.6 Ma) was detected in a sample of Allende meteorite, figure 2.4 (Tissot et al., 2016) shows the model fit of new initial ^{247}Cm abundance combined with the Early Solar System (ESS) initial ^{129}I and ^{244}Pu, all isotopes being produced by r-process, all abundance fit to a model curve of a common "free decay interval", which represents the time interval between last nucleosynthetic event producing these elements and their subsequent entrainment into ESS objects, such as the analysed meteorite.

The results from other measurements targeting ^{244}Pu from extra-terrestrial sources are presented in Wallner et al. (2015; 2021). There is a higher level of ^{244}Pu than the one produced during the nuclear tests (a subject that is discussed in the following sub-sections) was found in deep-sea crust and sediments pointing out an extra-terrestrial nucleosynthesis source.

Given the rarity of this plutonium nuclide with the highest half-life, the measurement technique mostly employed in astrophysics motivated studies is the Accelerator Mass Spectrometry for the investigation of ^{244}Pu in marine sediments (Paul et al., 2001; 2007) or iron-manganese deposits (Wallner C. et al., 2000; 2004). For the same purpose, this nuclide has been searched in samples that

originated outside the Earth, like Moon samples (Hutcheon et al., 1972; Reed et al., 1983) or meteorites (Fahey et al., 1987; Lewis et al., 1987).

Wallner C. et al. (2000; 2004) made one attempt to measure ^{244}Pu by alfa spectrometry is mentioned and after 546 days of counting only an upper limit on ^{244}Pu could be deduced to be 13μBq/kg of sediment, then the Pu-electro-deposited layer was dissolved, and Pu fraction was extracted and measured for 3.5 hours by AMS method. During the measurement time, only one count of ^{244}Pu was counted that corresponds to 3 x 10^5 atoms in the cathode. This work also shows the definitive usefulness of the accelerator mass spectrometry when attempting to do ultrasensitive detection of ^{244}Pu in environmental samples.

All the information described above corroborated with the signature of a two-million-year-old supernova in the spectrum of cosmic rays presented in Kachelrieß et al., 2015 indicates that the supernovas can be a source of r-process elements.

2.1.2. Core-Collapse Supernovae

The interstellar medium, after the Big Bang, has been enriched with heavy elements through cycles of forming and exploding or merging stars. The calculations that are trying to explain this recycling process are called galactic chemical evolution. The sites of r-process are not known, but CCSN and neutron star mergers are considered best candidates.

It has been over 30 years now since the evolution of very low metallicity stars is a topic of debate. Taking into consideration the metallicity, given by the Fe/H ratio, of star statistical simulations were elaborated and the results seemed to point to the stars that end their life as supernovas to be the source for r-process elements (Mathews and Cowan, 1990, Argast et al., 2004). The reason for this is that a supernova evolves faster than neutron star mergers because it takes more time to produce a neutron star and it takes time for those neutron stars to merge and produce enough heavy elements.

Supernova simulations showed it might produce r-process nuclei via a neutrino-driven wind mechanism. Neutrinos that are released from the proto-neutron star are carrying around 99% of the binding energy (Woosley and Janka, 2005, Panov and Janka, 2008). When they are in the densest region, that matter is actually opaque to neutrinos, so it is going to interact with different species that are present and it is through weak interactions ($\nu_e + n \rightarrow p + e^-$ and $\bar{\nu}_e + p \rightarrow p + e^+$) that the neutron to proton ratio is going to change or adjust the

nucleosynthesis output, also the influence the weak interactions depends on the neutrino luminosities and their average energies.

Only if neutrino interactions achieve to establish sufficiently neutron-rich and sufficiently high-entropy conditions, the production of heavy r-process elements and of the actinides becomes possible. In present CCSN models, this is not the case. However, the theoretical predictions of the spectrum of the emitted neutrinos and of the exact conditions in the neutrino wind are subject to various uncertainties, e.g. connected to the incomplete knowledge of the neutrino opacities of neutron-star matter, the possible role of sterile neutrinos or of other non-standard particle and neutrino physics, or the influence of strong magnetic fields if a magnetar is born in the stellar collapse (Goriely and Janka, 2016).

Briefly, the stellar collapse and supernova stages, as described by Burrows (1990) and Janka (2012), start with a massive progenitor star that has the so-called onion shell structure (Figure 2.5) with layers of nuclear material ashes from previous burning stages. At the center of the evolved star is the iron core, and it becomes unstable gravitationally when microphysical processes like electron capture on protons mostly found in nuclei set in and the photodisintegration of iron nuclei by the high temperatures.

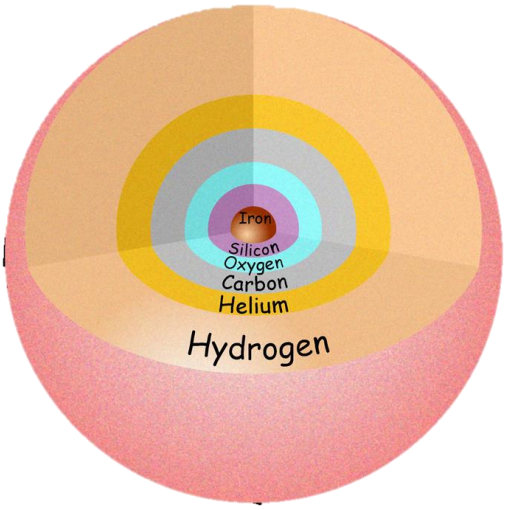

Figure 2.5. Onion Shell structure of a star with the elements neosynthesised in hydrostatic equilibrium

The collapse of the core happens within a fraction of a second and it forms a neutron star, the nuclear matter densities are reached and a shockwave that leads to a successful supernova explosion. The neutron star left behind is radiating neutrinos and maybe accreting more matter from the inner layers of the progenitor star that is still falling towards the neutron star. The neutrinos cool the neutron

star on a timescale of several seconds so that it finally becomes a cold neutron-rich star that is transparent to neutrinos.

2.1.3. The Evolution of a Supernova Remnant and Interplanetary Transport

During the expansion of an SN remnant after the explosion, interstellar medium is swept together, and at the same time the expanding gases cool. The explosion leaves behind an almost empty bubble containing only very hot, low-density gas. The expansion of the SN shell can go through three phases as described in Wallner (2000) and reference therein.

In the first expansion phase, the mass of the interstellar material swept up by the shock front is still smaller than the mass of the SN shell m_0. The speed of the expanding envelope remains approximately constant in this phase and corresponds to the speed at the start of the explosion of around 10,000 km/s. Assuming a spherically symmetric expansion, the radius of the shock front is denoted by r, so the mass of material collected is given by $\frac{4\pi}{3}\rho_{ISM}r^3$, where ρ_{ISM} is the density of the ISM. The end of the first phase is reached when the mass of the material swept up roughly corresponds to the mass of the shell that was blasted off. Assuming 10 $M_\odot$ for the shell mass and ISM for the density 1 proton cm^{-3}, which is about 0.025 $M_\odot pc^{-3}$, gives a transition radius of about 4 pc.

From the second expansion phase onwards, the mass of the swept-up matter dominates the mass of the shock wave. The expansion of the shock wave is done by the thermal energy of the gas in the sphere, which has a temperature of up to 10^9 K, and the wave expands adiabatically. This phase ends when the temperature of the expanding gas cools to below 10^6 K and the thermal energy of the gas can no longer drive the expansion, which is the case at about 10 pc.

In the third expansion phase, the expansion movement is only driven by the inherent momentum of the material of the wave. In this phase, the velocity of the shock front decreases due to the conservation of momentum as its mass increases.

At the end of the third phase, the velocity of the wave expansion period of about 1Ma at about 50 pc has decreased to about 10 km/s and then begins to mix with the surrounding ISM.

According to Wasserburg et al. (1996), the time needed for the mixing of the ISM within the galaxy is approximately given as the duration of a galactic year of 300 Ma, a mixing within a radius of about 100 pc can take place in a period of about 10 Ma.

Due to the length of these periods, the shorter-lived SN-generated radionuclides in particular, such as ^{60}Fe with $T_{1/2} = 2.61 \pm 0.04$ Ma (Ludwig et al., 2016), decay for the most part before they mix with the surrounding ISM. As a result, Fe can be assumed to be locally concentrated in relatively young SN clouds. Conversely, even more mixing in the ISM can be expected for longer-lived nuclides such as ^{244}Pu with $T_{1/2} = 80.6$ Ma. The half-life $T_{1/2} = 15.6$ Ma of ^{247}Cm is exactly in the range of the assumed mixing periods, whereby measurement of the frequencies of the three differently long-lived SN - generated radionuclides in terrestrial archives may provide information about the local mixing of the ISM. While a finding of ^{244}Pu on Earth coincident in time with ^{60}Fe, already found in terrestrial archives, would prove that both isotopes had the same production site, namely Core Collapse Supernova and they went through the same processes to arrive into the Solar System and subsequently stored in geological reservoirs on Earth.

2.1.4. Dust formation and Solar System environment

Assuming that most of the heavy elements released during explosive scenarios, from iron onwards and above will condense into dust (Evans, 1994, Bromley et al., 2014) and thus enter the solar system more easily than the gaseous components of the ISM, which are prevented from entering interplanetary space by the solar wind and radiation pressure. Dust condensation has been already observed following the SN 1987A event (Evans, 1994).

The environment of our solar system moves at a speed of about 30 km/s (Grun et al., 1994) through a local interstellar cloud that has a temperature of about 10^4 K and a density of about 0.1H atoms cm^{-3}, consisting of neutral and ionized gas and dust particles, which together are known as the local ISM. The movement of the solar system occurs almost in an elliptical direction (Grun et al., 1994), which is the plane of the planetary motion.

The space that our solar system occupies is called the heliosphere. The boundary of the heliosphere, the boundary of our solar system ends far outside the planetary orbits, is formed by a boundary layer, the so-called heliopause, where the solar wind and the ISM meet. A part of the ISM, like the wave produced by a moving ship, is deposited around the heliospheres (Linde and Gombosi, 2000). Especially interstellar gas and small, partly charged dust particles are kept from entering the solar system. This is caused by the solar wind, the radiation pressure of the sun, interstellar magnetic fields, etc. (Wallis, 1987). On the other hand, a

large portion of the dust in which the radionuclides of interest can penetrate the solar system.

2.1.5. Atmospheric Transport

Due to the motion of our solar system almost parallel to the ecliptic plane, the input of ISM onto the Earth's surface is not isotropic. The flux is greater in the region of the equator and decreases towards the poles, but with very close SNe whose shock wave can sweep over the Earth perpendicular to the direction of motion, and in this situation the greatest input is to be expected in the polar region. According to (Flynn, 1997), the large mass fraction of interstellar matter in the form of dust and micrometeorites that has reached the Earth will not burn up in the Earth's atmosphere but will only be slowed down and then sediment to the Earth's surface.

Due to the continuous rotation of the earth, it can be assumed that the incident ISM is distributed homogeneously over one latitude. Furthermore, the exchange times between the latitudes are only a few weeks, so it can be assumed that the ISM is distributed almost homogeneously over the entire surface of the earth. Specifically, for the transport of plutonium in the atmosphere, there is an observation from a satellite accident in 1964, during the transport of the SNAP 9A power generator that uses the heat generated by the α-radiation of ^{238}Pu to produce electricity. The satellite was loaded with approx. 1kg of ^{238}Pu when an error occurred in the rocket control system and caused the dispersion of the plutonium isotope in the atmosphere in the southern hemisphere (Hardy, 1973; Harley, 1980). Because of its rare use, this plutonium isotope, if detected on the Earth's surface, can very well be attributed to the satellite accident. In 1970, more than 95% of the ^{238}Pu had already reached the Earth's surface and could be detected at various measuring points distributed over a wide area of the Earth's surface. Similarly, plutonium from the surface and atmospheric nuclear weapons tests of the 1950s and 1960s can be detected relatively homogeneously over the entire surface of the Earth (Bowen et al., 1980; Livingston and Anderson, 1983).

2.2. Anthropogenic ^{244}Pu on earth

According to the UNSCEAR Report from 1982, 0.33PBq ^{238}Pu, 7.8 PBq ^{239}Pu, 5.2 PBq ^{240}Pu, and 170 PBq ^{241}Pu were released during the atmospheric nuclear weapons tests. These radioactivities correspond to several tons of $^{239,\ 240}$Pu.

Besides the global fallout, there were accidents with bomb-carrying aircraft, as in Palomares in 1966 or Thule in 1968, or leaks in industrial plants for plutonium production that led mainly to local contamination.

The isotopic composition of the atomic weapons fuel is determined by two factors: the design of the nuclear weapon and the form of production of the ^{239}Pu. The experimental results seem to indicate that the isotopic composition of this plutonium is very limited. Specifically, the ratio of ^{240}Pu / ^{239}Pu in number of atoms varies from 0.028 for plutonium of Russian origin produced in Mayak (Beasley et al., 1998) to 0.058 for plutonium released in the Palomares accident (Chamizo et al., 2010).

In the case of plutonium released in a nuclear detonation, it is the power of the bomb or, which is the same, the neutron flux involved in the fission chain, which determines the final isotopic composition. The higher the neutron flux, the higher the consumption of ^{239}Pu and the wider the spectrum of higher mass isotopes and transuranic elements produced by its neutron activation. For example, for the plutonium released in the first American thermonuclear test (Mike), an isotopic ratio for ^{240}Pu/ ^{239}Pu of 0.36 was measured, well above the average associated with the global fallout in the Northern Hemisphere, of 0.179 ± 0.012 (Kelley et al., 1999). The effect is completely different in tests associated with conventional fission bombs, in which the released plutonium retains virtually the isotopic composition of the original fuel. Thus, ^{240}Pu/ ^{239}Pu ratios in the 0.017 – 0.082 range have been measured at the Nevada nuclear site (Hicks and Barr, 1984). Also, a low isotopic ratio has been obtained in Nagasaki nuclear waste of 0.028 ± 0.002 (Saito Kokubu et al., 2008). Similar values (0.039 – 0.046) have been measured in Semipalatinsk (Yamamoto et al., 2001).

Regarding the isotope of interest for astrophysics, the needed conditions to produce ^{244}Pu were met during the nuclear weapon tests, while during nuclear accidents it is not produced because the short-lived nuclide ^{243}Pu (T1/2=4.96h) decays in a reactor before ^{244}Pu is produced. In a nuclear explosion, however, in which all nuclear reactions happen on a time scale of microseconds, ^{244}Pu can be produced directly via neutron captures on plutonium isotopes and subsequent decays after the explosion (Winkler, 2007; Wendel et al., 2013). Some works focused their investigations on the plutonium isotopes in connection with global or local fallout, for example in (Lachner et al., 2010) an isotopic ratio for ^{244}Pu/^{239}Pu for sediments from Bikini Atoll varies from 2.8 to 5.7 x 10^{-4} was measured, values that can help us to identify the source that produced the isotopes, another example one can find is in (Wendel et al., 2013) where a value of 1.44 x

10^{-4} for the global fallout in the northern hemisphere is given.

2.3. Microbialite, Stromatolites and Oncolites

Particular attention in this work is dedicated to ^{244}Pu incorporation and enhancement into biogenically formed carbonate-rich structures, such as microbialites, stromatolites, or oncolites.

Microbialites are organosedimentary deposits formed by the participation of microbial communities that trap detrital sediment and are responsible for inducing mineral precipitation. The term microbialite comes from Burne and Moore (1987) and has been widely used to describe carbonated stromatolites, and similar structures that occur with domic or columnar shapes in shallow waters of lacustrine and marine environments. Also, oncolites are included, given their laminated concentric structure and their microbial origin. In general, the term microbialite can be applied to different authigenic accumulations where microbes are locally abundant, such as tufas, travertines speleothems, or deposits generated from springs or fumaroles (Riding, 2002).

The starting hypothesis is that the rare earth elements (REEs) are immensely mass concentrated by these biological systems and that, via similar aqueous chemistry, so too should be the actinides. The ionic radii of lanthanides and actinides are similar to calcium therefore they can be substituted and uptake in the carbonate matrix (Anderson et al., 2003, Takahashi et al., 2005, Johannesson et al., 2014).

2.3.1. The oldest forms of life on Earth

Cyanobacteria are bacteria known as blue-green algae because of their colouring also known as cyanophytes. Cyanobacteria are photosynthesizing organisms, capable of processing solar energy and converting it into chemical energy. Cyanobacteria share with some other bacteria the ability to use atmospheric N_2 as a source of nitrogen, which facilitates the precipitation of calcium carbonate and gives rise to organo-sedimentary structures known as stromatolites. They represent an indicator of the beginning of life on earth, the oldest data found in Warrawoona (Australia) are stromatolite fossils from 3.45 billion years ago (Lowe, 1980; Hofmann et al., 1999). The presence of cyanobacteria is of great importance for the history and diversification of life on earth. In the early days, the proto atmosphere was rich in carbon dioxide,

cyanobacteria captured the carbon dioxide and transformed it into oxygen, thus the ozone layer began to form, and the environment began to evolve paving the way for the emergence of multicellular organisms. However, life existed without oxygen as there is evidence that bacterial reduction of sulfates, iron reduction and oxidation, and methanogenesis were already active and important metabolisms in the early biosphere.

The role of microbes, mainly bacteria and microscopic algae, in relation to the formation of microbialites refers to three main aspects: their performance as substrates for mineral nucleation or precipitation, the trapping of suspended particles, and chemical changes or processes linked to physiological activity, both in autotrophic organisms (eg , cyanobacteria) and heterotrophic organisms (eg , sulfate-reducing bacteria) (Lowe 1994; Merz - Preiß and Riding; 1999; Grotzinger and Rothman 1996; Dupraz et al., 2009; Spadafora et al., 2010).

Thus, various components and processes are involved in the formation of microbialites, linked to the presence of bacteria and small algae: mucilages or EPS (extracellular polymeric substances), secreted by the microbes, and which accumulate on the outside of the cells to form an adhesive matrix that traps and fixes the microbes to the substrate (Riding and Awramik, 2000).

Initially, EPS produced by cyanobacteria and other microorganisms bind Ca^{2+} cations that inhibit $CaCO_3$ precipitation (Dupraz & Visscher, 2005). However, three alterations of EPS have been proposed that favor $CaCO_3$ precipitation, as shown in figure 2.6, by microbial degradation of EPS (1) (Dupraz et al., 2004) through oxidation of the organic layer accumulated on the substrate generating alkalinity, which leads to carbonate precipitation, biomineralization (2) (Trichet et al., 2001) and by saturation of the binding capacity (3) (Arp et al., 2003). When the system is saturated with Ca^{2+} precipitation can start.

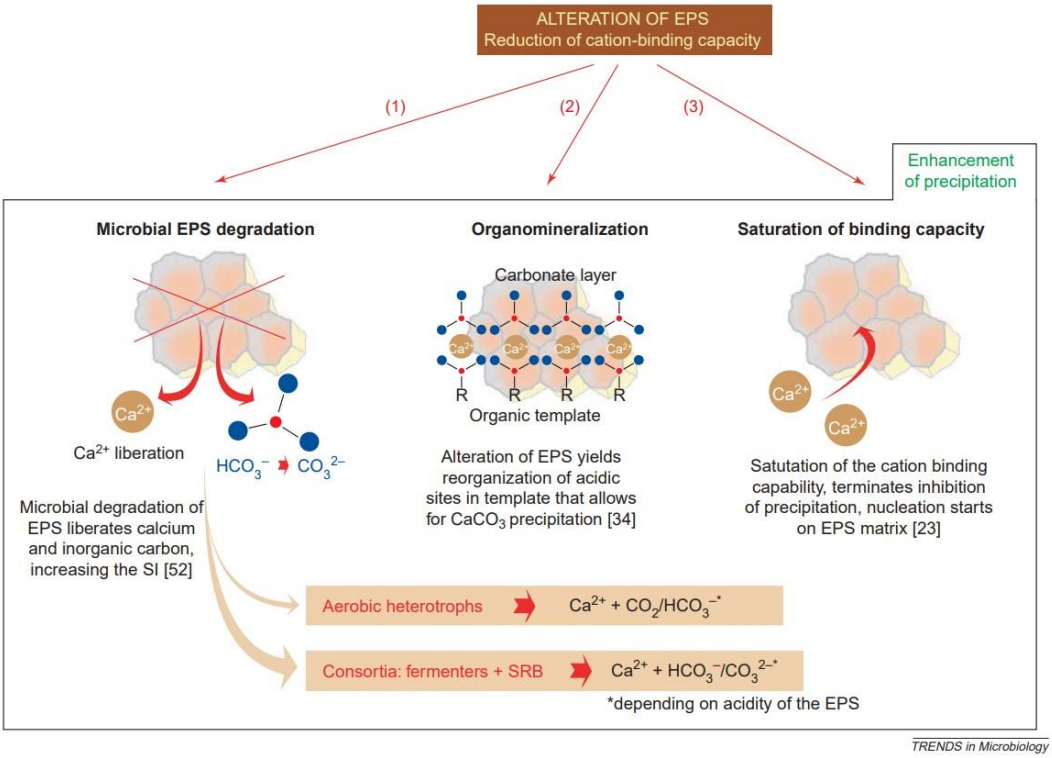

Figure 2.6. The three microbial pathways that enable calcium carbonate precipitation (taken from Dupraz and Visscher, 2005)

During the three processes described before, calcium ions can be replaced by other cations that are solubilized in the water, although they need to fulfill a necessary condition such as similar ionic radii.

As mentioned previously, EPS plays a major role in the structure and stabilization of microbial mats and biofilm. It should be noted that a microbial mat is the accumulation of lamellar biofilms that overlap each.

Hence microbial carbonates are considered indicators, not only of changes in microbial communities but also of changes in atmospheric chemistry and ocean saturation, which have influenced microbial metabolism and water saturation status marine (Riding and Liang, 2005). Microbes occupy a very wide spectrum of environments, including waters that have truly diverse chemistry and composition, and their involvement in sedimentation is equally varied (Riding, 2011). Many microbialites have a carbonated composition, mostly calcitic, but there are also aragonite or dolomite (Feldman and Mckenzie, 1997; Sanz-Montero et al., 2008).

Therefore, microbial carbonate deposits are produced by the interaction of microbial growth and metabolism, by the participation of mucilage (EPS) together with mineral precipitation and entrapment of detrital grains (Riding 2011).

Plutonium is likely to occur in aqueous environments in the III or IV valency oxidation state. Depending on which of these states the plutonium is present, it behaves in a similar way to the lanthanides or to the naturally occurring actinides, thorium and uranium. Nevertheless, all these cations, because of their atomic number, have an ionic radius similar to Ca^{2+} and if they are present in water, they can replace it during the carbonate precipitation.

2.4. Samples and experimental motivation

The scientific objective of this work fully depends on analysing fossilized material that can contain extra-terrestrial ^{244}Pu, such as microbialites or stromatolites of an age ranging between 2.6 to 1.6 Ma ago.

One site of suitable microbialites, occurring at the so-called" Vilama Formation", sits inside the Chilean part of the Atacama Desert. Evenstar et al., 2015 present the geological strata, and Naranjo et al., 1994 mention an age of 2 ± 0.9 Ma for it. In December 2016, Prof. Shawn Bishop and his collaborators carried out a geological field expedition in the region surrounding San Pedro de Atacama and collected a few tens of kilograms of the targeted fossilized reservoirs; the sampling area is presented in figure 2.7.

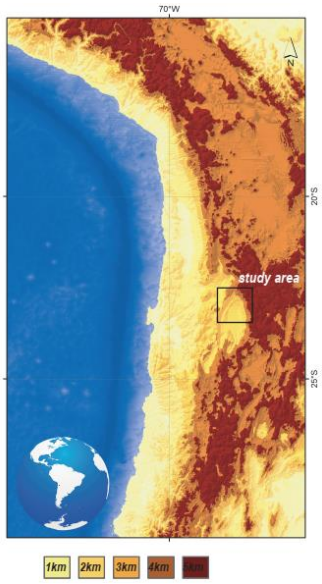

Figure 2.7. The sampling area, highlighted with black rectangle, of the microbialites from Salar de Atacama, Chile

The original choice to pursue the sampling of these stromatolites was based on a paper from 1994 (Naranjo et al., 1994) which reported the presence of them and provided a K/Ar dating of 2 ± 0.9 Ma age. During the fieldwork, however, and subsequent study of the stratigraphy made by Chilean geologists, it appears that these fossils are perhaps as much as 5 Ma old as it is shown in figure 2.8. In this figure the blue layer represents the new stratigraphic position of the stromatolite layer. The ages

in the left column have been obtained from literature and placed in this stratigraphic resume based on the SERNAGEOMIN (2016) maps and checked in the field by Geologist A. Cabre.

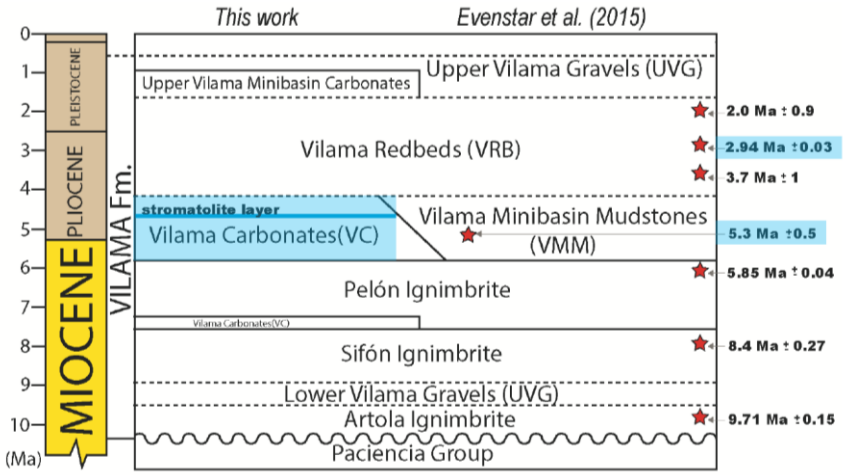

Figure 2.8. Stratigraphic units defined in Evenstar et al. (2015) against the new stratigraphic units of geologist Albert Cabré

If this is the case, such an age would place these fossils several millions of years prior to the arrival of the supernova material on Earth (the supernova ^{60}Fe signal spans 2.6 to 1.6 Ma ago and its maximum occurs at ~ 2 Ma ago). It is therefore physically impossible for these fossils to contain any material from the same supernova. It was, consequently, extremely vital to the original purpose of this work that viable bio-fossils be found, preferably as close as possible to 2 Ma age, situated in the geological strata within the supernova time window.

Lake Turkana, Kenya is the world site for the most important and significant hominid fossil discoveries, which have revealed the most scientific wealth on the evolution of *Homo Sapiens* and our evolutionary ancestors (Walker et al., 1986; Roche et al., 1999; Spoor et al., 2007; Robinson et al., 2017).

As a result of decades of anthropological fieldwork at Lake Turkana, the geological strata of the lake region have a very detailed geochronology dataset because when the anthropology community discovers new hominid fossils, accurate constrains of timing of sedimentation of the fossils is of paramount importance.

As a result, the geological history recorded in the strata surrounding the Lake Turkana basin, are extremely well-dated over the time window from the present to 4 or 5 Ma before present. It is, thus, an ideal location for sampling fossilized bio-systems, situated in the supernova time window.

The scientific literature review confirmed that such bio-systems exist in the Lake Turkana Basin geological strata situated at an age of around 1.9 Ma (Abell et al., 1982; Feibel et al., 1989; Joordens et al., 2013), as highlighted in figure 2.9. Geological material was sampled in December 2018 together with Prof. Shawn Bishop and collaborators.

From Turkana Basin we also sampled Holocene (<10 ka) stromatolites (Abell et al., 1982; Hargrave et al., 2014). The simultaneous AMS measurement of them will allow the quantification of anthropogenic plutonium, that could have been transported into the 2Myr stromatolite horizon.

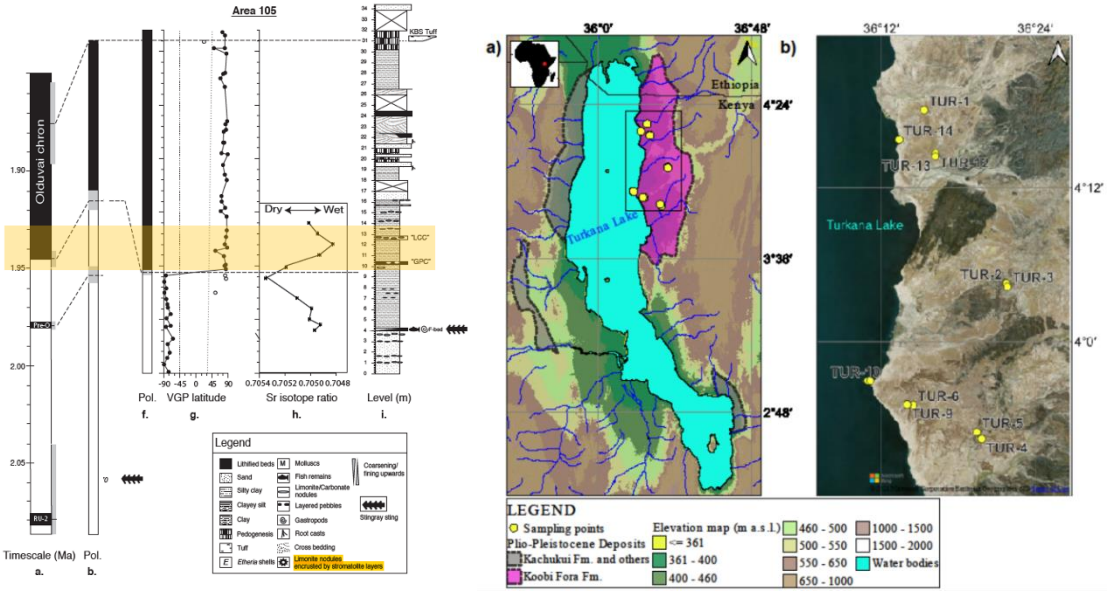

Figure 2.9. Stratigraphic units as presented in Joordens et al. (2013) and sampling location of the stromatolites from The Turkana Basin

Additionally, contemporary stromatolites and sediment cores (Farias et al., 2013) were sampled (Figure 2.10) from around the volcanic lake Laguna Negra in Argentina. These recent biological structures should have uptaken atmospheric Pu isotopes released during the Cold War bomb testing.

Figure 2.10. Stromatolites on the south-eastern shore of Laguna Negra, Argentina. Image: Shawn Bishop

Using the global fallout distribution measurements in the literature, the amount of Pu detected within the contemporary stromatolites could then be used to determine the ^{244}Pu biological uptake factor of stromatolites. Under the assumption that the organisms have not undergone radical evolutionary changes to their uptake mechanism over the past 2 Myr, this uptake factor could then be used to determine the fluence of ^{244}Pu from the supernova event.

Stromatolite or microbialites samples from all sites were used in this work to detect ^{244}Pu by means of Accelerator Mass Spectrometry. To keep a simpler track, each sampling site has a code: MFQB for the Atacama Desert, TUR for Turkana Basin, and EST for materials from Argentina.

To gain more knowledge about the samples as biologically formed structures, different types of analysis were employed. For example, for Atacama microbialite Gamma spectrometry measurement was employed for quantifying the natural radioisotopes and the daughters resulting from their decay chains, this measurement is allowing us to judge if the system remained closed over time or if it went under diagenesis processes like solubilization and reprecipitation of recent carbonates.

Scanning electron microscopy and X-ray diffraction were used to examine the microstructure and the mineralogical composition of the samples, while Inductively Coupled Plasma Mass Spectrometry was used to test the hypothesis of mass-concentration enhancement of trace elements.

3. Mass Concentration Enhancement

The starting hypothesis that the rare earth elements (REEs) are immensely mass concentrated by these biological systems and that, via similar aqueous chemistry, so too should be the actinides. In the following sections are described the sample preparation and the measurement procedure of REEs, thorium, and uranium inside our fossils and in water samples from the same geological areas by Inductively Coupled Plasma - Mass Spectrometry (ICP-MS).

3.1. Sample preparation

Sampling, digestion, and ICP-MS testing were done in a class ISO 8 cleanroom by using Teflon PTFE reusable labware.

Sample preparation consists of a matrix digestion step using an adequate method (reagents, digestion temperature, pressure conditions), e.g. in a microwave oven/reactor. It's important that: the analyte's concentration range be within the instrument's work domain, which can be adjusted by carefully diluting the sample. One batch of digested samples, for any type of sample consisted of two replicates from the sedimentary sample, two replicates of positive control, containing the sedimentary sample, and a known quantity of a multielement standard solution traceable to NIST SRMs; and negative control (QC-BD, digestion blank).

The samples MFQB R36 and TUR2 which are mostly carbonates with an amount of hard residue (silicates) were digested in two steps, for each sample the two components were measured separately and then summed up according to their concentration.

During the first step, an initial digestion at 250 °C with a mixture of ultrapure reagents: nitric acid 60% (5 mL) and hydrochloric acid 30% (1mL) only the carbonate part was solubilized. Approximately 500 ± 50 mg of sample (solid, homogenous powder) were weighted in 15 mL Teflon (PTFE) vials, mounted in a rack for a 1 L digestion tank (all PTFE), in a closed system, and pressurized with nitrogen to eliminate cross-contamination.

After the first digestion, the white residue (mostly silicates) was separated and washed 3 times with ultrapure water and centrifuged and the liquid was discarded. After drying it at 60^{o}C for 24 hours the samples and 1 mL of acid solution (5% HNO3, 0.5% HCl) or 1 mL of standard solution was homogenized using an ultrasound bath for 20 minutes. To solubilize the silicates 0.7 mL $HClO_4$ (70%) and

2.1 mL HF (48%) was added, and the solution was kept for one hour at 70°C, then all the vials were shake for 24h. Finally, the digested samples were evaporated to dryness and the residue was re-dissolved in 5% HNO_3 and 0.5% HCl solution, during this step most of the silicon was lost due to the evaporation of the fluoride compound formed.

The volcanic ash samples (MFQB42, MFQB46, and MFQB48) were digested also in two steps, because the first digestion of the samples, microwave-assisted, was done in a mixture of nitric acid and hydrofluoric acid. By using HF in excess the rare earth elements precipitated, the recoveries off them in the liquid part were all less than 3%. This situation implied the analysis of the precipitate. First, it was separated, washed with ultrapure water 3 times, centrifuged, and dried at 70°C. To solubilize the precipitate a second microwave-assisted digestion, was done in an acid mixture of 5% HNO_3 and 0.5% HCl.

The water samples from Chile (Teben, Ojossal and Rvila) and from Kenya (TUR10, TUR11, and TUR14) were collected in cleaned PFA bottles, filtered with 0.4 μm Millipore filters and acidified to pH < 2 with ultrapure Nitric Acid (60%) and analysed.

3.2. ICP-MS measurement

The elemental analysis of the samples was done with an ICP-MS 7700s from Agilent Technologies USA (figure 3.1.) (Serban et al., 2021) equipped with an ESI SC-4DX autosampler, the instrument parameters are listed in the table 3.1.

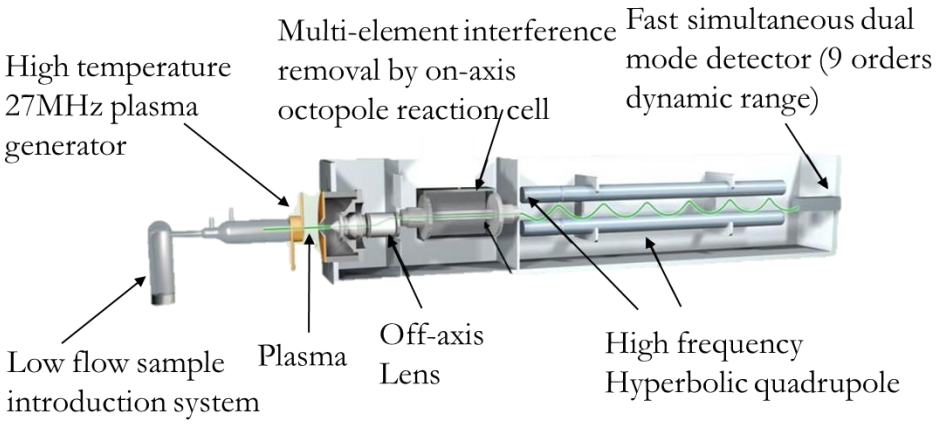

Figure 3.1. Main components of the ICP-MS 7700s system adapted from https://www.agilent.com/cs/library/brochures/5990-4025EN.pdf

Table 3.1. Instrument parameters

RF Power	1500 W
Sample Depth	9.4 mm
Plasma Gas (Ar) flow	15 $L \cdot min^{-1}$
Carrier Gas (Ar) flow	0.7 $L \cdot min^{-1}$
Makeup Gas (Ar) flow	0.5 $L \cdot min^{-1}$
Collision Gas (octupole reaction cell, He)	3 $L \cdot min^{-1}$
Nebulizer Pump speed	0.1 rps
Oxide level (CeO^+/Ce^+)	< 1 %
Double charged level (Ce^{2+}/Ce^+)	< 2 %

Mass interferences represent a major problem in mass spectrometry, e.g., isobar species, polyatomic or molecular interferences which overlap on the mass signal of interest, but by utilizing a collision/reaction cell with He, ppt level (µg/kg) quantitative results can be obtained.

The mass spectrometer tuning was done according to the manufacturer's specifications, with a multielement standard solution – called tuning solution (5 elements in a 2 % nitric acid matrix: Li, Co, Y, Ce, Tl, 1 ppb each) – in both "no gas" and "He" modes (in the collision cell – an octupole), calibrating the mass axis in 3 points for small, medium and high masses; and optimizing the ion optics for the best signal to noise ratio.

Calibration standards required to represent the calibration curves for each isotope monitored are: 0.01 µg/kg, 0.05 µg/kg, 0.1 µg/kg, 0.5 µg/kg, 1 µg/kg, 10 µg/kg, 100 µg/kg, 500 µg/g, 5000 µg/kg.

Samples were afterwards analysed, running 2-3 wash blanks between two consecutive samples to prevent "memory effects" (carry-over). Also, to monitor the stability of the system during the measurement an Internal Standard was used – Indium solution with a concentration of 20 µg/kg.

3.2.1. REEs plots

The samples analysed from the Atacama Desert, Chile, were: MFQB R36 - microbialites, as well as Teben, Ojossal, Rvila - water samples, and from the Turkana Basin, Kenya, the samples were: TUR2 – stromatolites, as well as TUR10, TUR11, TUR14 - water samples. The plots for REEs are presented in Figure 3.2. and 3.3., and the concentrations for the natural actinides (uranium and thorium) are

listed in Table 3.2. For all determinations, the measurement relative standard deviation for all the elements is between 1 and 2%.

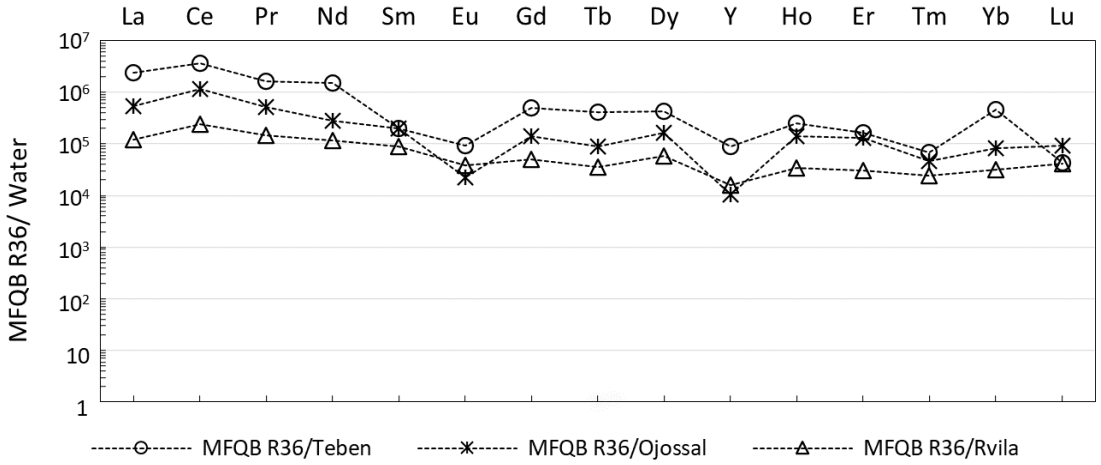

Figure 3.2. REEs concentrations of microbialite normalized to water samples from Atacama Desert, Chile

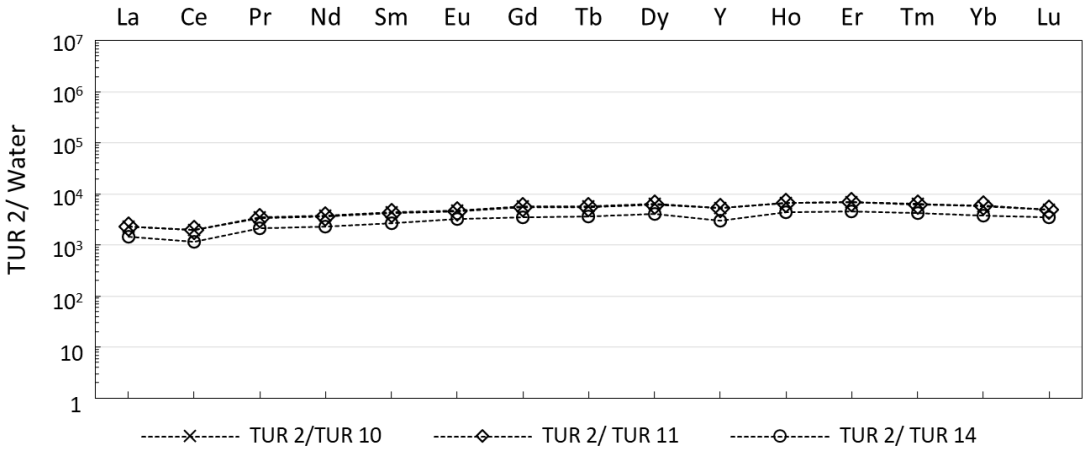

Figure 3.3. REEs concentrations of stromatolites normalized to water samples from Turkana Basin, Kenya

As shown in figure 3.2. the mass concentration enhancement for the Atacama Desert sample for REEs is ranging from 10^4 to 10^7 and for the Kenya Basin sample is ranging from 10^3 to 10^4. For thorium and uranium, the mass concentrations are ranging from 10^3 to 10^4 for Atacama microbialites and from 10^2 to 10^3 for the Turkana stromatolites. The measured concentrations for the natural actinides are presented in table 3.2.

Table 3.2. Thorium and uranium concentrations

Sample	*Atacama Desert, Chile*				*Turkana Basin, Kenya*			
	Microbialite		*Water*		*Stromatolite*		*Water*	
	MFQBR.36	*Teben*	*Ojossal*	*Rvila*	*TUR2*	*TUR10*	*TUR11*	*TUR14*
Th [µg/kg]	948.5	0.00027	0.00019	0.00555	1362.18	1.05	1.00	1.54
U [µg/kg]	3222.8	0.42	2.04	4.1	865.07	10.97	10.06	8.74

In nature an overall property of the REEs group is that it can be divided into two conventional named groups: light REEs from Lanthanum to Europium and Heavy REEs from Gadolinium to Lutetium, Yttrium being usually assigned to the heavy REEs due to physical and chemical resemblance with Holmium. This property results from the lanthanide contraction phenomenon whereby the ionic radii of REEs decreases with increasing atomic number and is the main attribute that governs the subtle differences in the REEs geochemical behaviour. The elements with larger ionic radii are generally more incompatible, that is, they cannot easily substitute for the major cations in rock-forming minerals, than their equivalents with smaller ionic radii (Heavy REEs).

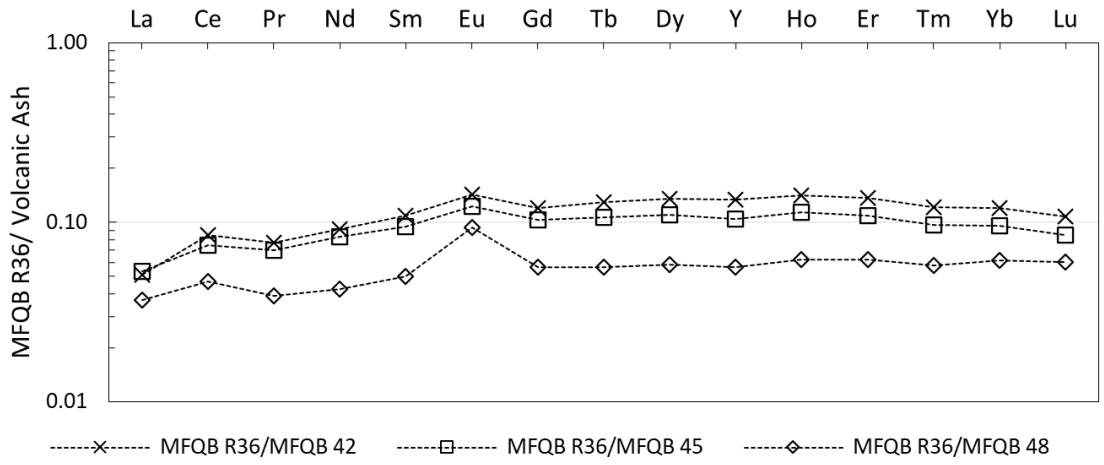

Figure 3.4. REEs concentrations of MFQB R36 - Atacama microbialite normalized to volcanic ash

In figure 3.4 is shown the REEs behaviour described, namely, the heavy REEs substituted calcium (and/or magnesium) in the carbonate lattice of the microbialite, pointing out that the volcanic ashes are leached by the water where the microbialites are growing.

4. AMS Sample production

The structure of this chapter corresponds to the target preparation for the AMS measurement of plutonium, which was developed at the RoAMS laboratory in IFIN-HH, Romania and it will be discussed in detail in the following sections.

In AMS, the concentrations of isotopes with long half-lives are usually measured in a matrix of stable isotopes of the same element, e.g., the radioactive carbon isotope (^{14}C) versus the stable isotopes $^{12, 13}C$. However, since actinides do not have stable isotopes, a certain amount of a reference isotope of the same element is added before the chemical preparation of a sample, e.g., ^{242}Pu as the reference isotope for a measurement of ^{244}Pu. To produce the cathodes for the AMS measurement of plutonium from natural materials three main steps must be followed and it starts with obtaining the solution ready to undergo column extraction chromatography, which implies sample digestion and, eventually, sequential removal of matrix elements. The second step is the Pu separation and extraction using the TEVA special resin and finally to obtain the target material by co-precipitation of plutonium isotopes with iron hydroxide.

4.1. Plutonium extraction

In the following paragraphs the specific details of sediments digestion, extensively used for the preparation of the IAEA (International Atomic Energy Agency) reference materials like sediments from Bikini Atoll and from Pacific Ocean, as well as for the sediments sampled from Laguna Negra, Argentina are presented. Another important part of this work is the extraction of plutonium from stromotolite with sample mass up to 10kg. In this case, several other steps were implied to remove the major matrix constituents like calcium, magnesium, aluminium, iron and titanium as indicated in (Maxwell et al., 2006; 2011; 2014 and 2015). In figure 4.1 an overall procedure for plutonium extraction from stromatolites for AMS measurement is presented and in the following sections the procedure is detailed.

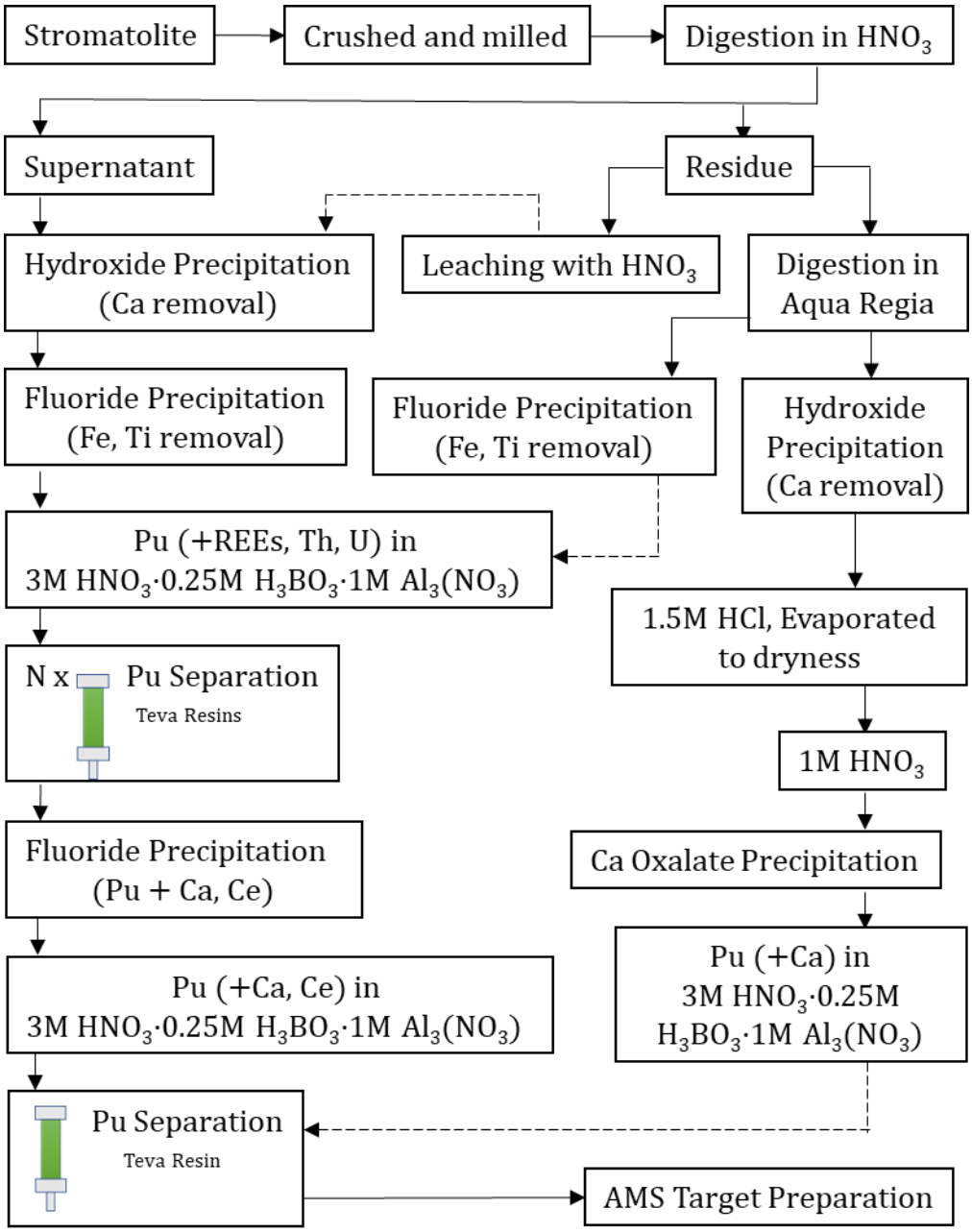

Figure 4.1. Flow diagram of the chemical procedure used to extract plutonium from Stromatolites

4.1.1. Sample digestion – sediments

An environmental sample is digested following the method described in (Chamizo et al., 2011). The sediment is first dried in a muffle furnace by calcination for 8 hours at 550ºC to remove organics that may be present in the sediment aliquot, and then transferred in Teflon beakers with 20 milliliters of concentrated Nitric Acid and 10 mL of concentrated hydrochloric acid.

The beaker is kept on hot plate for three hours and is heated near their boiling point. The solution together with the undissolved solids were transferred to polypropylene tubes and centrifuged for 5 minutes at 4000 rpm. After this step the supernatant is separated and stored using another tube and the residue is transferred back to the initial beaker. Twenty milliliters of nitric acid and fifteen milliliters of hydrofluoric acid are added. The sample is evaporated to dryness on the hotplate. This step is done twice and is followed by the addition of 10 milliliters of 7% perchloric acid. The sample is again evaporated to dryness and the supernatant that was separated previously was added to each beaker and 10 milliliters of concentrated nitric acid is added and evaporated to dryness, this step being performed two times. Finally, the residues were dissolved in 10 milliliters of warm 3M HNO_3 · 0.25M H_3BO_3, 14mL of 7M HNO_3 and 14mL of 2M $Al(NO_3)_3$.

4.1.2. Sample digestion – microbialites and stromatolites

Even if the chosen fossilised materials for the ^{244}Pu search show mass concentration enhancement, to improve our chances to detect, if it is present, the r-process isotope the starting quantity of material is in the order of a few kg.

The chemical procedure starts with crushing (using the Retsch jaw crusher in Figure 4.2) the microbialites or the stromatolites into pieces with dimensions ranging from 3 to 6 cm. After that the pieces are milled two times, first is to achieve a granulometry of around 1mm and the second one to obtain a fine powder.

Figure 4.2. The Retsch jaw crusher and milled samples

The sample powder is digested with several litters of nitric acid solution (~32%) using a custom-made Teflon Tank (Figure 4.3). The material choice for the construction of the tank was based on the reaction conditions, the reaction

between carbonates and nitric acid is a strong exothermic one, Teflon or Polytetrafluoroethylene is a suitable material, very stable from the chemical point of view.

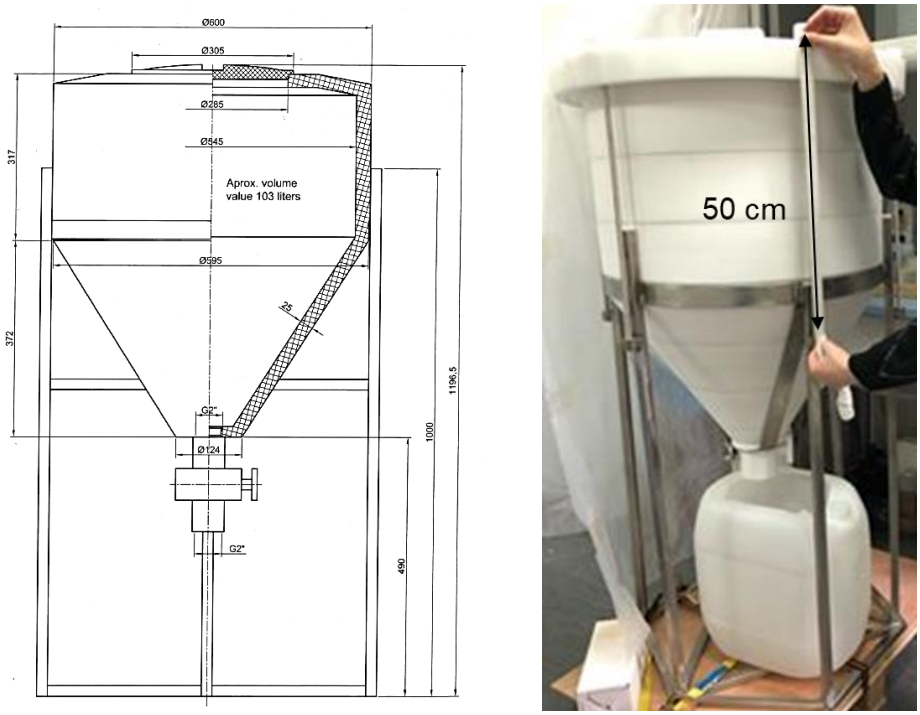

Figure 4.3. Custom-made Teflon Tank

After the reaction, the mixture containing soluble Nitrates and undissolved residue is released from the tank by using the faucet at bottom of the tank in 30L HDPE (high density polyethylene) barrels and left to settle for several days.

Figure 4.4. Barrels with the sample mixture after the initial reaction and recovery of the supernatant

Once the undissolved residue is well separated from the supernatant, the liquid is transferred in another barrel. The principle of communicating vessels was used by filling a tube with ultrapure water and one end was introduced into the sample being very careful not to reach the area where the residue is (Lopez-Lora, 2014). At the same time the other end is positioned inside another barrel at a lower height so that, due to the difference in pressure between the ends of the tube, the liquid begins to flow towards the area of lower pressure, thus extracting the supernatant liquid (Figure 4.4).

4.1.3. Chemical processing of the Supernatant

The following paragraphs describe plutonium preconcentration with sequential separation of matrix components, which is carried out using an iron and /or titanium precipitation, depending on the specific composition of each type of sample, with hydroxide precipitation followed by a fluoride precipitation step. During each precipitation, the new major component is able to attract, among others, the lanthanides, uranium, thorium and plutonium present in the sample matrix.

To separate the major component of the solution, which in our case is calcium; we perform the co-precipitation of iron/titanium hydroxides with the trace elements present in the sample matrix. Depending on the sample matrix, to ensure a similar quantity of hydroxide precipitate, the pH of the supernatant is adjusted by slowly adding ammonia solution (aqueous NH_3) to 4 or 8, with continue stirring and pH monitoring; the first value is used when the sample contains a large quantity of titanium, while the latter was targeted when iron predominated as a minor component. calcium is avoided under these conditions, as it precipitates as hydroxide at pH 10. Once the desired pH value was reached, the sample was shaken to promote colloid formation and allowed to stand for at least 48 hours for complete settling.

Subsequently, the precipitate is recovered again using the principle of communicating vessels, and to further separate the liquid, the hydroxides are centrifuged using 200 ml bottles at 4300 rpm for 20 minutes. The precipitate is recovered with ultrapure water and dissolved with a solution of 9M HCl, and the added volume is calculated to give a final concentration of 1.5M.

Figure 4.5. Hydroxides precipitation and recovery

At this point in the procedure, the iron and/or titanium have changed from minor to major components and need to be further separated from trace elements. Since it is quite difficult to handle the radioactive tracer while working with such large amounts and with a unique laboratory container, the steps taken up to the end of iron precipitation are checked by determining lanthanides and natural actinides by ICP-MS measurements.

After centrifugation and solubilisation of the precipitate a known amount of tracer is added, usually when performing experiments with ^{244}Pu, 0.2pg of ^{242}Pu which is equal to $5 \cdot 10^5$ particles.

To remove iron and/or titanium, hydrofluoric acid is added to the previous solution and to promote the fluorides precipitation the mixture is left overnight at 8^{o}C or is cooled in an ice bath for a few hours.

Figure 4.6. Fluoride precipitation

After a good separation of the fluorides is achieved, the precipitate is recovered and centrifuged. Finally it is dissolved in an equal volume of 12M HNO_3 · 0.35M H_3BO_3 and a double volume of 2M $Al(NO_3)_3$.

4.1.4. Chemical processing of the Residue

Several different chemical procedures were used to investigate the residues remaining after the first reaction with nitric acid. A first procedure, which is like that applied to the supernatant and has been described previously, is implying the leaching of the residue with concentrated nitric acid (65%) for two weeks, the resulting supernatant is subjected to the same procedure of precipitation of iron hydroxides and fluorides.

Another procedure applied implies the digestion of the residue in aqua regia (1:3.6 = HNO_3 65%: HCl 57%) followed by either a direct precipitation using hydrofluoric acid or a precipitation of iron hydroxide with NaOH solution at pH=10.

After the recovery of the iron Hydroxide, it was solubilized with Hydrochloric acid and ultrapure water. To try to separate as much as possible the iron, that can affect the resin separation, calcium oxalate precipitation was performed (Wallner, 2000).

The first step was to evaporate the solution to dryness twice with nitric acid and then dilute it with water and add concentrated nitric acid to ensure a concentration of 1M and adding the needed amount of tracer. By using the quantity of NaOH solution added we could infer the quantity of iron in solution so we can be sure that for every 1g of Fe in the solution we add at least 10g of oxalic acid. The large amount of oxalic acid is needed because the iron present into the solution must be saturated before insoluble oxalates can be precipitated. The organic acid was added after the solution was heated at 70°C on a hotplate, after the solution became clear, NH_3 solution was added until pH 2 was achieved. The solution was kept on the hotplate for a few hours with continuous stirring and then cooled while the precipitating oxalates were forming; they were allowed to settle over a period of 48 hours.

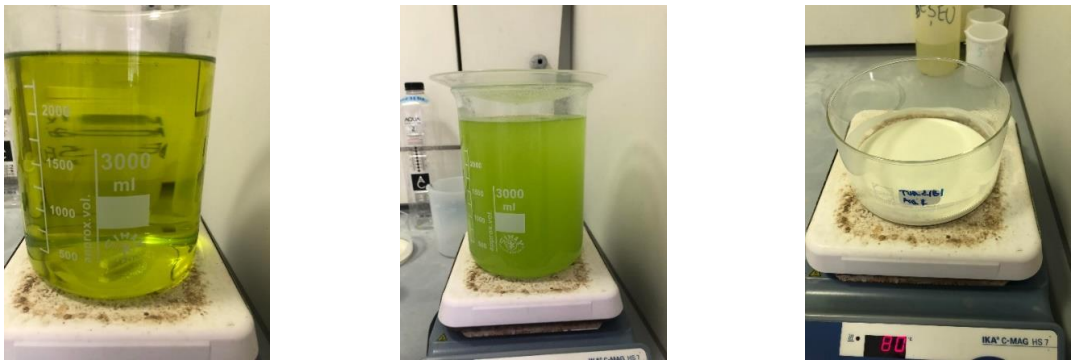

Figure 4.7. Precipitation of calcium oxalate

After sedimentation the oxalates are centrifuged and removed, the clear solution is again slightly acidified, then 2 grams of Ca in the form of $CaCl_2 \cdot 2H_2O$ and the steps for precipitation are repeated with the addition of 50g of oxalic acid.

The recovered oxalates were calcined for 10h at 450°C. At higher temperatures was avoided as plutonium can be oxidised into heavy complexes. After oxidation, CaO is dissolved in HNO_3 and a black precipitate is produced (Figure 4.8), which is caused by the remaining oxalate decomposed to carbon.

Figure 4.8. Black precipitate during Ca oxalate procedure

The black precipitation disappears by adding conc. H_2O_2 while heating to 70°C. The solution is then alternately concentrated and dissolved again in H_2O_2 until the development of brown gas (nitrogen oxides) is completed, as this still indicates the presence of oxalates and carbon. The elimination of the carbon in this way is important because carbon can adsorb plutonium. The residue was dissolved and evaporated twice in nitric acid 65% and finally dissolved in 3M $HNO_3 \cdot$0.25M $H_3BO_3 \cdot$1M $Al(NO_3)_3$.

4.1.5. TEVA separation

The chromatographic separation is a technique used to separate various elements from different type of matrixes. This technique combines the selectivity of the liquid-liquid extraction with the ease of operation of the chromatographic columns.

For the chromatographic separation of plutonium TEVA resin was used, which has an active part an aliphatic quaternary amine (Figure 4.9 b). Figure 4.9 a) shows the distribution coefficient (or k and is the ratio of the concentration of solute in the organic phase over the concentration of solute in the aqueous phase)

as a function of the molarity of the nitric solution used. This coefficient is related to the capture ability of the different elements by the resin, the maximum retention for plutonium occurs when a 3M HNO_3 solution is used. Boric acid and aluminium nitrate were used to complex fluoride ions, especially, as in this work case where high concentrations of lanthanides and calcium are involved, the nitrate and the boric acid are necessary to complex thorium for good chemical yields.

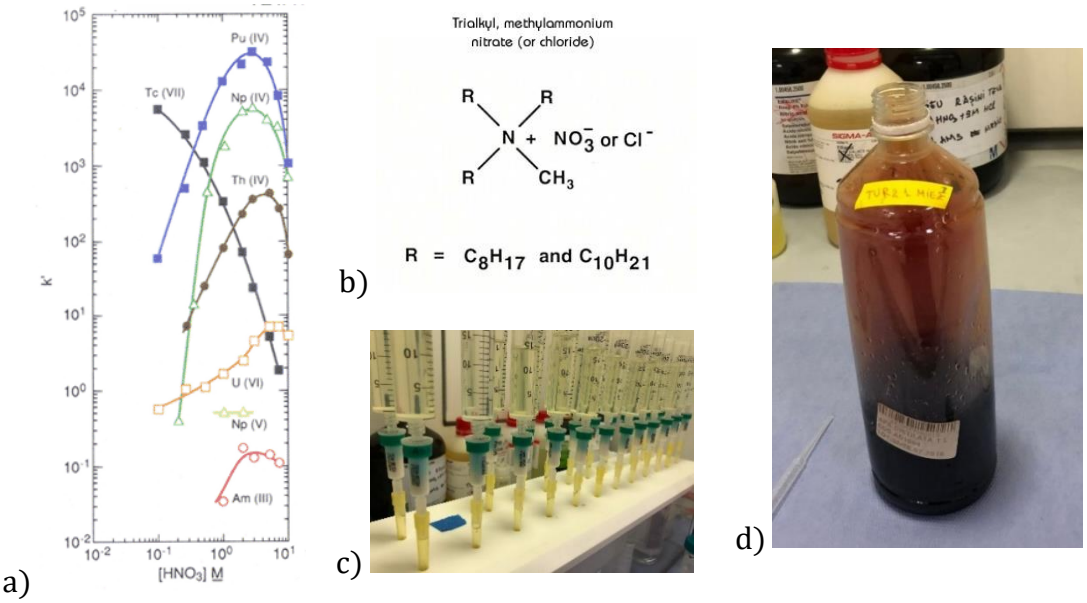

Figure 4.9. a) Actinide uptake as a function of the molarity of the nitric solution, b) The active component of the TEVA resin – trialkyl, methylammonium nitrate (or chloride), c) Vacuum box system from Eichrom and TEVA resins, d) Valence adjustment of Pu- Brown fumes resulted from $NaNO_2$ reaction with H_3NSO_3

The plutonium separation procedure started with the valance adjustment and was performed following the procedures described in Maxwell et al., 2006; 2011; 2014 and 2015. To the load solution sulfamic acid , iron nitrate and ascorbic acid was added with a 3-minute wait step to reduce plutonium present in solution to Pu^{3+}. The valence reduction of Pu isotopes is enhanced as a result of the reduction of ferric ions to ferrous ions by ascorbic acid. After the reduction step, 3.5M $NaNO_2$ was added to oxidize plutonium to Pu^{4+}, during this step, brown fumes evolve from the reaction of the nitrite with the sulfamic acid, and the solution turned dark (Figure 4.9 d), by continuing to add the sodium solution with swirling, the solution should clear. After the valance adjustment the solution is loaded onto the TEVA resin cartridge. The TEVA resin used in all the experiments are those the Eichrom offers ready to use as cartridges of 2mL with a grain size of 100-150 mesh. Samples and wash reagents were placed into 20mL reservoirs.

The plutonium extraction is carried out in 4 main steps. First, the resins are conditioned to the optimum working medium by washing it with 5mL of 3M HNO_3. The sample is then introduced, leaving mainly plutonium and thorium retained in the column. The uranium fraction is removed by washing with 20 ml of 3M HNO_3, and the thorium fraction with 20 ml of 9M HCl, after this strong solution another 5mL of 3M HNO_3 are added to reduce the bleed-off of the resin during Pu strip step. Finally, the plutonium is extracted with 0.1 M HCl/0.05M HF.

During the chemical preparation of the stromatolites and microbialites, several fractions, between 10 and 20, were obtained. In this case a second Ca/ Ce fluoride precipitation was performed, by adding several milliners of cerium Nitrate solution (1mg Ce/ 1mL solution) and calcium nitrate solution (40mg Ca/ 1 mL solution) and Hydrofluoric Acid 48%. After the recovery of the precipitate by centrifugation, it was dissolved in 3M HNO_3·0.25M H_3BO_3·1M $Al(NO_3)_3$ and plutonium was extracted again by using only one TEVA resin.

4.2. Chemical yield

The chemical yield for some of the procedures described before was determined directly by measuring ^{242}Pu tracer using alpha spectrometry and/or indirectly via other trace elements like lanthanides or natural actinides (uranium and thorium) by determining them before and after some specific steps during the chemical procedure.

4.2.1. ICP-MS

For the preconcentration step we have measured the chemical recovery for trace elements (REEs, Th and U) by determining the absolute quantity of each element in the solution after the digestion, in the precipitate and in the solution remained after precipitation. More specific, aliquots from each resulting solution or precipitate were collected and trace elements were measured by ICP-MS and corrected for the involved dilution factors. The results are presented in table 4.1 for Atacama Microbialite and in table 4.2 for Turkana stromatolite. The measurement relative standard deviation for all the elements measured is between 1 and 2%.

Table 4.1. Quantitative determinations of REEs, Th and U in different stages of the chemical procedure for Atacama Microbialite

	Solution BEFORE Precipitation [µg]	*Precipitate [µg]*	*Solution AFTER Precipitation [µg]*	*Chemical Recoveries*
La	60.5	57.8	< 2.8	95.6%
Ce	123.2	108.2	< 25.8	87.8%
Pr	15.8	14.6	< 2.6	92.2%
Nd	61.0	54.9	2.9	90.0%
Sm	13.9	11.7	0.9	83.9%
Eu	2.6	1.8	0.7	69.8%
Gd	11.5	10.7	< 0.6	92.9%
Tb	1.7	1.4	< 0.2	84.4%
Dy	8.6	8.2	0.5	94.9%
Ho	1.6	1.5	< 0.2	90.9%
Er	4.5	4.2	< 0.4	93.8%
Tm	0.7	0.6	< 0.2	78.1%
Yb	3.6	3.4	0.3	93.7%
Lu	0.7	0.52	< 0.47	76.6%
Th	10.2	10.1	< 2.52	99.7%
U	1813.5	1586.4	83.0	87.5%

Table 4.2. Quantitative determinations of REEs, Th and U in different stages of the chemical procedure for Turkana Stromatolite

	Solution BEFORE Precipitation [µg]	*Precipitate [µg]*	*Solution AFTER Precipitation [µg]*	*Chemical Recoveries*
La	308.8	14.6	247.5	80.2%
Ce	415.8	10.2	346.5	83.4%
Pr	93.0	1.4	65.2	70.1%
Nd	342.5	6.5	270.7	79.0%
Sm	88.2	0.9	63.7	72.3%
Eu	11.9	0.3	6.7	56.6%
Gd	112.4	11.8	76.4	68.0%
Tb	11.1	0.1	7.3	65.9%
Dy	98.6	0.8	71.9	73.0%
Ho	13.9	0.1	9.5	68.7%
Er	23.2	0.2	16.1	69.6%
Tm	6.9	0.1	5.4	79.4%
Yb	20.5	0.1	14.2	69.4%
Lu	5.9	<0.2	4.6	76.8%
Th	5.7	<0.1	5.7	99.1%
U	12.3	0.1	11.7	95.2%

The chemical recoveries are satisfactory, ranging from 60% to 99%, for concentrations that varies over three orders of magnitudes, showing that for elements with even lower concentrations the chemical recovery is in the same range, the results are comparable for both type of fossils.

4.2.2. Alpha Spectrometry

Prior to the AMS measurements it by alpha spectrometry the radiochemical recovery yield of the overall chemical procedure but also each major step that is involved during the AS target preparation was checked.

To assess the chemical yield for plutonium separation by alpha spectrometry (AS), it is needed to disperse/ distribute the analyte uniformly on a surface to obtain the alpha sources, for this work two obtaining methods were investigated: electrodeposition and microprecipitation.

The electrodeposition procedure (LaMont et al., 1998) starts with the elimination of the HF from the Pu solution by taking the sample to dryness, add 8 M HNO_3 and evaporate the sample to dryness again. This step was repeated two more times to ensure that all the hydrofluoric acid is removed. To remove any organic interference that may come from the TEVA resin, a sulfuric acid step is done, followed by evaporation to dryness and wet ashing the sample with nitric acid. After the sample cooled down, 9 mL of 0.75M H_2SO_4 and thymol blue-color indicator were added and transferred to the conical electrolytic cell where the pH was set to 2.1 using NH_4OH. The final step consisted in inserting the platinum wire anode to 1cm of the cathode. The current was set to 0.75 A for 1 hour. After this time, 1 ml of ammonia was added and, one minute later, the system was switched off. At the end, the disk was rinsed with MilliQ water and placed on a hotplate at 300^{o}C for 10 minutes.

The microprecipitation was performed following the procedures described in Maxwell et al., 2011 and 2014. The procedure begins with the addition of 50 µg of Ce (Single Element solution traceable to NIST, Merck) to the Pu solution. After adding 1mL of HF to the solution and waiting for 30 minutes, the solution was filtered using a 25mm polypropylene filter (0.1 µm pore size disposable ResolveTM filter funnel). The filters were washed with ethanol to displace the water. Finally, the filters were affixed to stainless steel disks using double sided adhesive tape and dried using a heat lamp for 10 minutes.

Alpha spectrometry was performed using the Mirion PIPS detectors. These detectors have an active area of 450 mm^2 and energy resolution of <18 keV with a

detector source spacing equal to the detector diameter. The planchets (Pu sources) were placed at 1.5 mm from the detector surface and for the evaluation of the spectrums and data analysis was used the Genie 2000 v.2.2 software (Canberra). For energy calibration and efficiency determination was used a Mixed Alpha source with a total activity of 6.5 Bq provided by Eckert & Ziegler Analytics.

Table 1 presents the results, which show that we obtained a very good recovery of plutonium by applying the chemical procedure to the sediment sample. Even if the uncertainties are quite large, between 10% and 20% due to small counting times in the order of a few hours and small quantity of the reference isotope, it was possible to check which preparation method of the AS planchets has more advantages, electrodeposition or microprecipitation. The result is better for microprecipitation, this method involves less steps and there is no need to evaporate or to transfer the solution from one beaker to another. Also, the spectrums (not shown) obtained for microprecipitation were cleaner. One reason could be that during electrodeposition more chemicals are added in relatively large quantities and can contaminate the solution used for electrolysis. Because of this all the other alpha spectrometry measurements were done using microprecipitation, and as expected when careful procedures are involved the recoveries of ^{242}Pu with or without TEVA separation have similar values (table 4.3).

Table 4.3. Radiochemical recoveries of Pu (ED – Electrodeposition, MP – Microprecipitation)

Sample	Chemical yield [%]	RSD [%]
AS2 ED, only ^{242}Pu	76.6	18.6
AS7 MP, only ^{242}Pu	94.9	17.2
AS10 MP, IAEA 410 spiked with ^{242}Pu and TEVA separation	85.7	15.9
AS16 MP, only ^{242}Pu and TEVA separation	94.3	11.9
AS11, Atacama Sample	96.1	17.2
AS19, Atacama Sample	94.3	16.6
AS15, Turkana Sample	50.9	15.7
AS18, Turkana Sample	63.6	18.4

With respect to the chemical recovery of plutonium when processing the fossils, table 4.3 is showing very good recovery of around 90% for the Atacama stromatolite. While for the turkana stromatolite the chemical yield is between 50 and 60%, which is satisfactory for our purposes.

4.3. Preparation of the cathodes

For the AMS measurement it is required to bring our samples in a suitable form for the ion source, for this it is needed to obtain the samples pressed in a cathode in such a way to guarantee a good thermal and electric conductivity. The first step is to add 1mg Fe/mL solution, purchased from High Purity Standards to each Pu solution resulted in the chromatographic separation process. Then Pu and Fe are coprecipitated with ammonia solution as hydroxides. The vials are centrifuged at 4500 rpm for 5 min and the supernatant liquid is removed and the precipitate is washed with ethanol 99.8% to remove any remaining supernatant liquid and centrifuged again.

Using a plastic Pasteur pipette, the hydroxides are transferred to quartz crucibles of approximately 0.8 ml volume and dried at 65^{o}C for 2 hours. Once the iron precipitate is completely dry, the crucibles are placed in a muffle furnace at 800^{o}C for 4 hours to oxidize the iron precipitate and the plutonium isotopes. This step is essential for efficient ionization in the ion source. The resulting iron oxide is usually conglomerated, and it is crushed using 50µL of ethanol 99.8% and a small plastic spatula and dried. The oxide powder is mixed with 3 mg of niobium 99.8% (Sigma Aldrich), by homogenizing the sample with this metal its thermal and electrical conductivity are improved. Finally, the mixture is pressed onto an aluminium cathode.

5. AMS setup and measurements

After the description of the target material preparation, this chapter describes the method used to measure plutonium isotopes, namely Accelerator Mass Spectrometry together with the description of the 1MV Tandem Accelerator from IFIN-HH, Romania and the measurement procedure.

5.1. Introduction to AMS

Accelerator mass spectrometry (AMS) is a highly sensitive method for detecting long-lived nuclides of very low concentration. When measuring actinides, it is usually sufficient to determine the mass of a nuclide to identify it, since isobars with comparably long lifetimes that can interfere with the detection of the targeted element rarely occur.

In general, the objective of mass spectrometry (MS) techniques is to determine the isotopic composition of the elements present in a sample. To do this, they take advantage of the fact that the trajectories described by the ions within electric and magnetic fields depend on certain relationships between their energy (E), mass (M) and charge (q). There are three stages involved in this process: a first in which the sample is transformed into an ion beam; a second in which the components of the beam are separated in space by a combination of kinematic filters; and a final one in which the particles of interest are quantified in a detector. Conventional MS techniques are usually classified according to the type of ion source used in each case. In ICP - MS (Inductively Coupled Plasma Mass Spectrometry) the sample, in solution, is ionized in an argon plasma; in TIMS (Thermal Ionization Mass Spectrometry) the beam of analysis is generated by heating a metallic filament (thermal ionization) that contains the sample. In RIMS (Resonance Ionization Mass Spectrometry) a laser is responsible for the selective ionization of the constituents of the sample, solid or liquid. In any case, the ions produced, always positive, are extracted from the source with a determined electrostatic potential. Therefore, those that have the same charge state will have the same energy and, in the next stage, their trajectories will basically depend on the mass.

However, these techniques have a series of limitations. This is mainly there are going to be ions with the same kinematic characteristics as the ions of interest, or that their trajectory is the same due to dispersive processes. When discriminating some ions from others based on the mass/charge (M/q) ratio, we

cannot differentiate those ions that have same M/q ratio. Furthermore, there may be molecules or isobars with a mass very close to that of the nucleus of interest. Although, in principle, with a suitable combination of kinematic filters the final mass resolution of the spectrometer could be improved, in practice, the achievable resolution is finite, and its improvement implies a transmission loss. On the other hand, isotopes with very long half-lives have very low concentrations, which means working with few atoms. Accelerator Mass Spectrometry (AMS) overcomes these limitations by incorporating an accelerator (usually tandem type) at an intermediate stage of the selection process for the isotopes of interest. This allows, on one hand, the destruction of the molecular background in a stripping process and, on the other hand, the acceleration of the particles thus allowing the use of nuclear detectors.

5.2. The AMS system of IFIN-HH

The 1 MV Tandetron™ AMS system from IFIN-HH is a compact system with a footprint of 3.8m × 6.3m, entirely dedicated to AMS analysis. Figure 5.1 shows the arrangement of the components of the installation (Klein et al., 2006). The arrangement of the facility is in U-shape, which is helpful for the ionic optics of the system.

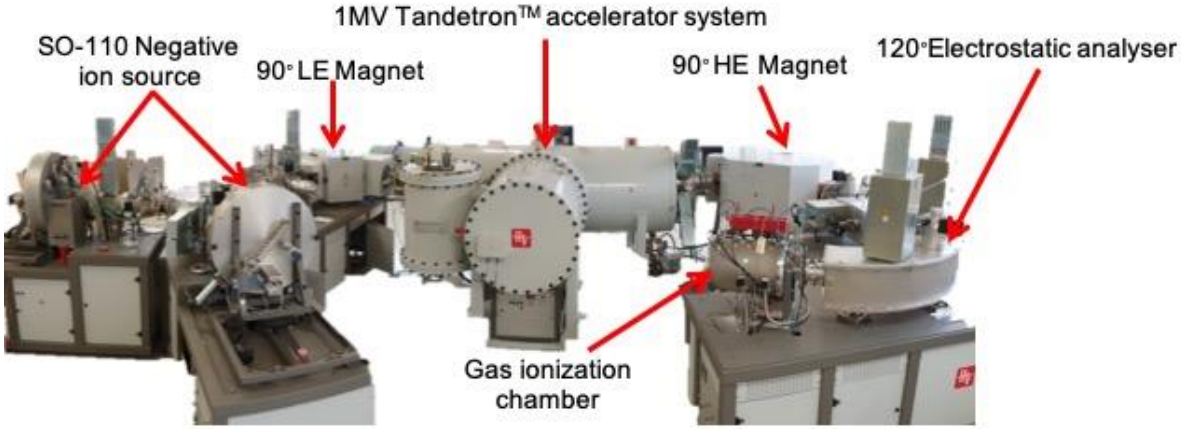

Figure 5.1. 1 MV Tandetron™ AMS system from IFIN-HH

Figure 5.2 shows the technical design with all the components of the system, two independently Cs-sputter Negative Ion sources (SO-110 HVE model) (1), a rotatable 54° low energy electrostatic analyser (LE ESA) (2), 90° Injection magnet with multi beam switcher (bouncer) (3), 1 MV tandetron accelerator system, with gas stripper channel (4), 90 ° high-energy analysing magnet (5), 120°

electrostatic analyser (6), 2 anode particle detection system (7) and Cockcroft-Walton high voltage generator (8).

1 MV Tandetron™ system can be divided into 3 sides. The first area is the low energy side, which consists of two negative ion sources, the electrostatic system for switching the beam from one source to another and the 90° magnetic analyser.

In the second area is the acceleration system, where the negative particles passing through the first analyser magnet are attracted by the positive voltage applied on the middle of the terminal, pass through the charge exchange channel becoming positive with different charge states and are further accelerated by the positive high voltage. Therefore, the acceleration system is called tandem, the particles are accelerated in two stages. The third area is the high energy side which consists of the 90 ° magnetic analyser, the 120° electrostatic analyser and the charged particle two anodes detection system.

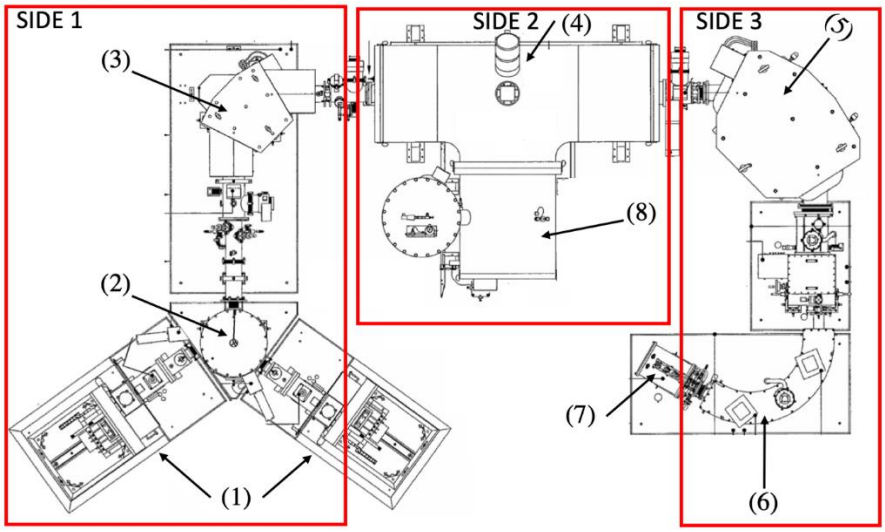

Figure 5.2. General scheme of the 1 MV AMS installation from IFIN-HH (Pacesila, 2019)

5.2.1. Cs-sputter Negative-Ion source

The 1MV particle accelerator is equipped with two identical negative ion sources model SO110, see Figure 5.2. The negative ion sources are based on the principle of sputtering; the target sample is bombarded with Cs ions. Two identical sources were bought at this facility, as one source was originally dedicated to ^{14}C dating experiments to avoid source or sample contamination issues, while the second source was used for other isotopes, such as ^{10}Be, ^{129}I, $^{239,240}Pu$ etc. With this

type of source, high-intensity negative ion beams can be extracted using almost any element from the periodic table.

Fig. 5.4 shows the basic components of the source: the cathode, in which the material of interest is pressed, the ionizer, the caesium reservoir and the extractor. The whole assembly is under 10^{-7}-10^{-8} mbar high vacuum obtained by a vacuum system composed of a preliminary vacuum pump and two turbo-molecular pumps.

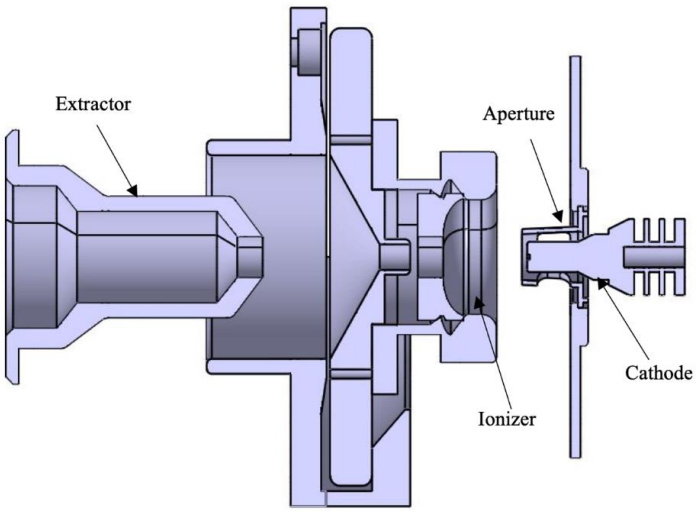

Figure 5.3. The main components of the Cs-sputter Negative-Ion source (Courtesy of D. Pacesila)

To avoid contamination from one sample to another, the source is equipped with a carousel that is under vacuum and is separated from the actual chamber of the source by a high-pressure valve. Inside the carousel there is a circular support in which 50 samples can be placed and a pneumatic piston that inserts or removes the samples in turn, see Fig. 5.4. The pneumatic piston can be actuated manually (in turn) or automatically from the system control program. This system of movement and change of samples shortens the measurement time, by the fact that several samples are introduced at the same time, but also when switching from one sample to another, the source parameters remain unchanged.

One of the essential parts of this type of source is the ionizer. It is a metal piece with a spherical surface, made of tungsten, because this material has a melting point of over 2500°.

The ionizer is heated to temperatures between 1000-1400° C by applying a current of up to 20 Ampers, provided by a stabilized power supply. The optimum operating value obtained by us is 18 A (see Figure 5.4).

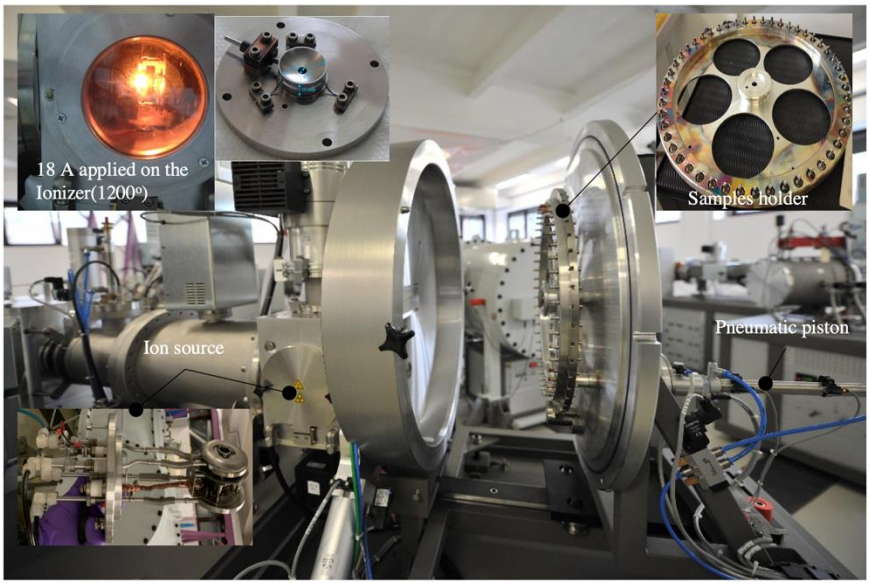

Figure 5.4. Ionizer heated to 1000-1400° C, the carousel for the 50 samples and the ion source

At the same time, the caesium reservoir is heated by a resistor, wrapped around it, to the optimum operating temperature of about 100ºC. The caesium vapours resulting from the heating leave the reservoir and reach the area between the cathode and the ionizer. Some atoms interact thermally with the hot surface of the ionizer and because of this interaction ionizations occur (Cs atoms lose an electron thus becoming positive ions). The ionization of atoms occurs since the energy for removing the last electron from the caesium electron shell, of 3.87 eV, is lower than the extraction energy of an electron from the metal volume of the tungsten ionizer which is 4.62 eV. At the same time a part of the neutral atoms condenses on the surface of the cathode, which is continuously cooled, thus forming a monoatomic layer of Cs on the surface of the material of interest (Mosu, 2013).

By applying a negative voltage to the cathode, a potential difference is generated between it and the ionizer, which is grounded, the positive ions are thus accelerated towards the material of interest. The geometry of the source and the spherical shape of the ionizer, help to have a very good focus and to direct the Cs^+ beam towards the centre of the cathode surface. Cs + ions bombard the sample surface in an extremely small area of 1.5 mm, penetrating the volume of material. Following this bombardment, the atoms in the sample begin to sputter. When the sputtered atoms pass through the neutral Cs layer deposited on the cathode surface, some of them will ionize by the addition of electrons, obtaining negative ions.

The sputtering rate of the atoms in the material is given by the ratio between the number of Cs + ions incident on the sample surface and the number of ions expelled from the material.

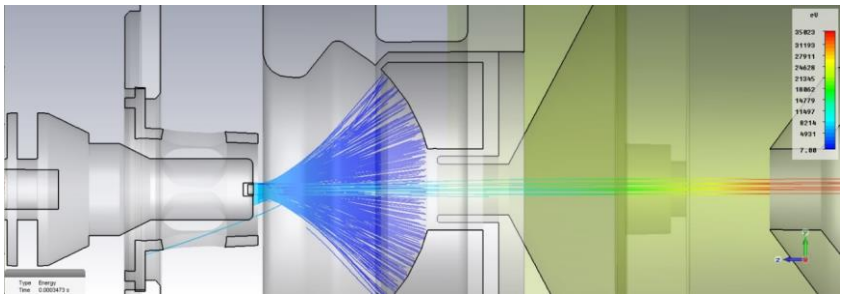

Figure 5.5. Simulation of the operating principle of the negative ion source; With blue: Cs beam positive, multi-coloured: extraction compound extracted as negative beam. In the upper right-hand corner is the intensity of the negative ion beam extraction energy (Courtesy of D. Pacesila and A. Rotaru)

Following the bombardment with heavy Cs ions, the negative ions are formed in a proportion of about 0.01-3%, in the same time also positive ions and other molecular fragments are formed. To extract only negative ions, a negative voltage of 28 kV is applied to the inner chamber of the source in the ionizer area. This leads to a pre-acceleration of the negative particles, thus forming the beam of negative ions leaving the source accelerated to a potential difference of 35 kV (7 kV applied on the cathode and the 28 kV applied on the ionizer area). Since the extracted ion beam is very divergent, it is focused with the help of an Einzel lens, positioned at the exit of the source.

During the measurements it is important that the beam produced is intense and stable. Thus, the heating of the ionizer must be done gradually, and the cooling must be done in a vacuum to avoid the oxidation of caesium on its surface. Oxidized caesium on the surface of the ionizer restrains the production of Cs positive ions leading to a very weak beam current or sometimes its absence. Even in the case of a good operation of the ionizer, for some elements with very low electronic affinity a very weak current can be obtained, that is why some species of ions are extracted from the source in the form of oxides, these having a higher electronic affinity.

5.2.2. Electrostatic deflector

The first component of the system is a 54° electrostatic deflector, found approximately at 400 mm from the two sources. It is a deflector in the shape of a circle sector of 54° and a radius of curvature of 469 mm, composed of two metal

plates, placed in parallel at 54 mm from each other. Its role is to deflect the ion beam on the optical axis of acceleration, directing it towards the entrance of the analyser magnet on the low energy side.

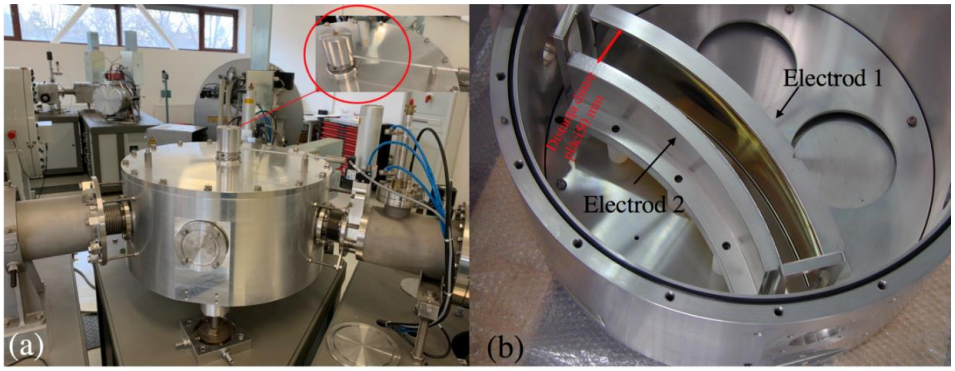

Figure 5.6. Electrostatic deflector: (a) in the circle you can see the lever that changes the position of the electrodes. (b) deflector electrodes and the distance between them

By applying a maximum electrical voltage of 3kV on each plate, but of opposite polarity, an electric field is formed, and a selection of particles is obtained according to the ratio between energy and charge state of the particles, E/q. In this case, all negative particles have the same energy of 35 keV (energy with which they are extracted from the ion source) and the same state of charge (-1), so the E / q ratio is the same for any negative particle. It turns out that on the low-energy path, this deflector does not act as an analyser but only deflects the beam extracted from one of the sources, at an angle of 54 °. This deviation is done by rotating a lever, from one position to another, depending on what source is used. Fig. 5.6. (a) shows this lever as an enlarged detail.

5.2.3. 90° Injection Magnet

The last part on the low energy side is the 90 ° magnetic analyser. This is a magnetic dipole with a radius of curvature of 400 mm and a distance between poles of 50 mm and has the role of bending the negative ion beam at 90 ° but at the same time selects particles based on their mass. The separation power of ions of different masses depends on the constructive characteristics of the analyser magnet and is generally given by a quantity called MEP (derived from Mass Energy Product), standing for the mass-energy product of the particle to be analysed. The particle cannot exceed the maximum value of this MEP (Enachescu, 2006; Chamizo, 2009).

To understand this quantity, the value for the $^{27}Al^-$ ions extracted from the ion source is presented. For ions having a charge state (q = -1) and an energy around 35 keV and a mass of 27 u.a.m., the corresponding MEP has the value of 0.945 u.a.m. × MeV. The MEP value of the magnetic analyser on the low energy path of this installation is 8.4 u.a.m. × MeV, a value that allows particles with an energy of 35 keV and masses of up to about 260 u.a.m. to be analysed.

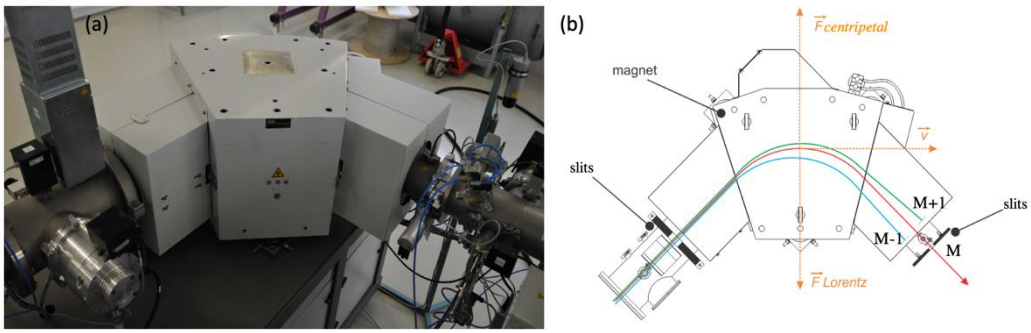

Figure 5.7. 90 ° magnetic analyser on the low energy side (a) and the forces acting on the trajectory of the ions (b)

The trajectory of the particles is given by the balance between the magnetic force Lorentz and the centrifugal force, so the scalar relation is:

$$qvB = \frac{mv^2}{R} => (BR)^2 = \frac{2mE}{q^2} \qquad \textit{Eq 5.1.}$$

where: q is the charge state (-1) in module, R is the radius curvature of the analyser magnet, E is the energy of the particle, which is constant on the low energy side, being equal to the product between the charge state (-1) and extraction voltage Uext (E = q × Uext). By varying the intensity of the magnetic field from a small value to a larger one, ion beams of different masses pass one by one through the magnet, and the currents are recorded at the output of the magnet in the Faraday Cup system. Knowing the magnetic field for which two maxima of the ion current are obtained, the corresponding masses can be figured out. Thus, from the relation below it is possible to calculate the magnetic field, B_2 for the particle of mass interest m_2, starting from a known value B_1, for a particle of mass m_1:

$$B_2 = \sqrt{\frac{m_2}{m_1}} B_1 \qquad \textit{Eq 5.2.}$$

However, the separation power of the magnet is not high enough to make the difference between an isotope and a molecule that have about the same mass. For example, the magnet cannot differentiate between $^{14}C^-$ (having an atomic

mass of 14.0032 u.a.m.) and 12CH2- molecules (having a molecular mass of 2 * 1.0078 + 12 = 14.0156 u.a.m.) because the relative difference in mass is ΔM / M = 1/680 which is well above the mass resolution of the magnet.

The 90° magnetic analyser is also equipped with a bouncing system. This system allows to switch between the rare and stable isotope by applying a voltage on the magnet chamber (which modifies the particle energy) and at the same time keep the same magnetic field value to avoid the hysteresis phenomenon. By changing the energy of the second particle, the condition is fulfilled for it to pass through the magnet (relation 5.3) without modifying the magnetic field to the corresponding value. Thus, the relation 5.3 becomes m × E = constant. This change is made by connecting the metal chamber of the magnet to a power supply, which polarizes the centre of the chamber with a medium voltage, the range being between (-3000V; +3000V). The sections at the ends of the chamber are connected to ground, so that an electric field is formed between the ends and the centre of the chamber. A specific voltage is applied to each isotope. The voltage is applied sequentially at a frequency of 100 Hz, and the period of application differs from one isotope to another, depending on the abundance of each.

$$V_{int} = \left(V_{sample} + V_{ext} + V_{REF}\right)\frac{m_{ref}}{m_{int}} - \left(V_{sample} - V_{ext}\right) \qquad \textit{Eq 5.3.}$$

where V_{REF} is the voltage applied to the reference isotope, usually zero, m_{ref} is the reference mass, m_{int} is the mass to be injected using the bouncing system, V_{int} is the required voltage to be applied to the magnet chamber, V_{sample} is the voltage applied on the cathode and V_{ext} is the extraction voltage applied to the ionizer area. For example, when carbon isotopes are measured (12C, 13C, and 14C), the reference voltage is 0 V, and is the calculated value for the mass of 13 u.a.m. When a positive voltage of 2869 V is applied, all the particles entering the magnetic field are accelerated and therefore gain more energy. The magnetic field is constant, so that only particles with a mass of 12 u.a.m., i.e., 12C, pass through the centre of the magnet, and particles with a smaller/larger mass are deviated from the optical axis, hitting the walls of the magnet. The same thing happens when the voltage applied to the magnet chamber changes its value, -2450 V, only in the opposite direction. The particles are decelerated, their energy decreases, and so when they enter the magnet chamber they are more strongly curved, so that only particles with a mass of 14 u.a.m pass through the centre of the magnet. These accelerations and decelerations take place only inside the magnet chamber, so that the voltage applied to the chamber, which initially breaks the particles, at the exit of the magnet the particles are accelerated, finally having the same energy as at the input.

5.2.4. Linear electrostatic accelerator system Tandetron™

The Tandetron™ acceleration system is a linear electrostatic accelerator that uses a Cockcroft-Walton voltage multiplier consisting of identical stages of diodes and capacitors to obtain the high voltage applied to its terminal.

It consists of acceleration columns, one on the low energy side and the other on the high energy side, the accelerator tubes which are installed inside the columns the terminal, the main electrode on which high positive voltage is applied, the charge exchange channel located in the center of the terminal together with the stripping gas recirculation system, the motor generator and the Cockcroft-Walton high voltage generation system.

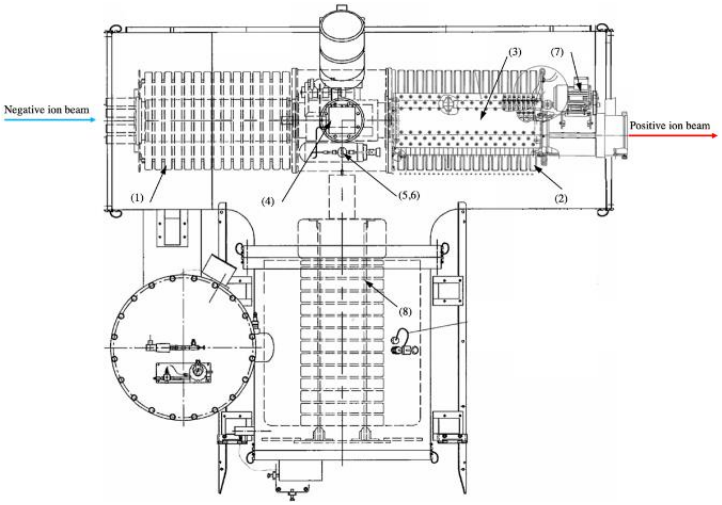

Figure 5.8. Technical drawing of the 1 MV TandetronTM acceleration system from IFIN-HH

After the first selection of the low-energy analyzer magnet, the negative ion beam is injected into the tandem accelerator. The first acceleration stage takes place in the low energy acceleration column.

The low and high energy acceleration columns are constructively identical, the only difference being the electric field distribution. In the low-energy column, the electric potential increases from the outer end of the column to the central area, where the terminal is found, while in the high-energy column the electric potential decreases from the central area to the outside of the acceleration column. Each column consists of 16 metal disks, insulated from each other by glass discs.

The high voltage generator is Cockcroft-Walton type. This system is a voltage multiplier, which converts the AC voltage applied to the input into a DC

voltage, but with a very low current (of the order of tens or hundreds of μA). The operating principle of the Cockcroft-Walton generator is exemplified in Figure 5.9:

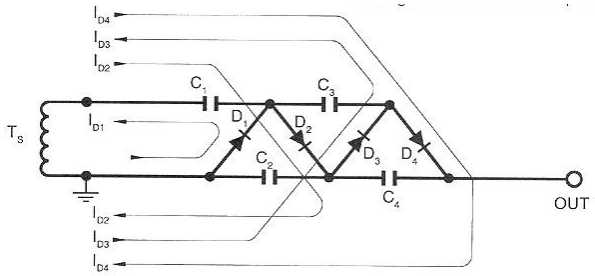

Figure 5.9. The operating principle of the Cockcroft-Walton generator (Pacesila, 2019)

Mainly, a Cockcroft-Walton generator is built from an AC high voltage source (Ts), capacitors for signal uniformity (C2 and C4), coupling capacitors (C1 and C3), diodes connected in series (D1, D2, D3 and D4) and the charging phases of the system (ID1, ID2, ID3, ID4) respectively. It takes several cycles to charge the generator. Figure 5.10 shows the order in which the capacitors are charged. In the first positive half of the input signal, capacitor C1 is charged. In the second half of the signal, C2 is charged. In the next positive half, C3 is charged and serialized with C1. Each capacitor can be charged with the maximum voltage provided at the input (ideally) and after a few cycles the charging is complete. The measured output voltage will be the input voltage multiplied by the number of stages, twice for each stage. Basically, the system loads the capacitors one by one and then they are serialized. The maximum possible voltage assumes that there is no current loss, no capacitor discharge and infinite output resistance (Mosu, 2013).

The output voltage can be described by the following equation:

$$U\ out = 2 \times N\ \times\ Epk - \left(\frac{Ic}{6fr \times Cap}\right)(4N^3 + 3N^2 - N) \qquad Eq\ 5.4.$$

where N is the number of stages, Epk is the maximum AC voltage applied to the input of the multiplier CW, Ic is the load current applied to the output of the multiplier CW, fr is the input frequency of the AC voltage and Cap is the capacitance of the capacitor. In formula 5.4, the first part is the maximum output voltage, and the second part is the potential drop that occurs when using a real load, so the final voltage is the difference between the two. The maximum output voltage decreases as the load current introduced into the accelerator increases. Generator fluctuations are described in formula 5.5:

$$dU = \frac{Ic}{2\,fr\,\times Cap} N(N+1) \qquad \textit{Eq 5.5.}$$

The final voltage applied to the acceleration column will be U output + dU. We can see from the formula that to reduce these fluctuations, we must introduce alternating voltage in the generator at a frequency as high as possible (from tens to hundreds of kH).

A gas exchange channel is installed in the centre of the terminal, where the process of charge exchange takes place, see Fig. 5.10 It has a cylindrical shape with a length of 30 cm and a uniform diameter of 6 mm. The gas used is argon and is stored in a small gas tank, installed inside the accelerator tank. The gas pressure is set with thermal valve, controlled from the control panel. To have a pure gas, it is continuously recirculated with a turbomolecular pump with a capacity of 400 l/s (Chamizo, 2009).

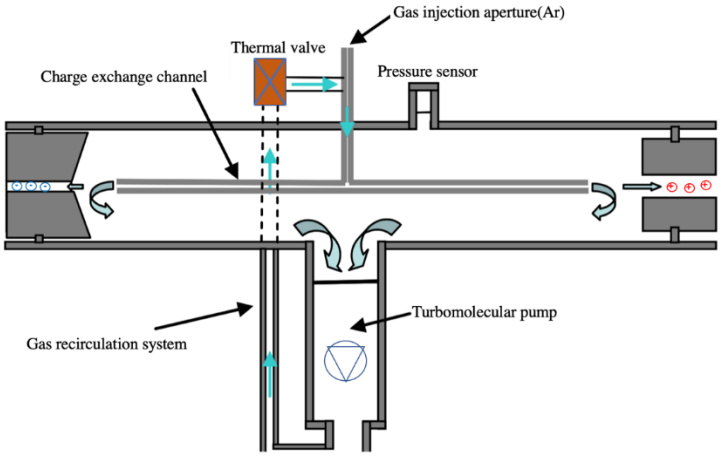

Figure 5.10. Charge exchange stripper gas and the gas recirculation system (Adapted from Chamizo, 2009)

Accelerated negative ions are passing through the stripper channel, where they collide with neutral argon atoms. As a result of these collisions the negative ions are losing electrons and become positive ions, with different charge states (q = 1 +, 2 +, 3 +, 4 +, 5 +, 6 +, 7 +, ...). The positive ions are further accelerated in the second half of the acceleration system, due to the potential difference between the terminal (high positive voltage) and the outlet area of the acceleration tube on the high energy side, which is connected to ground. Depending on the state of charge, the ions have different energies.

5.2.5. High energy 90° analysing magnet

After the acceleration stage the multitude of ions coming out of the acceleration system, with different masses, energies, and charge state, are passing through the second 90° dipole magnet, called the analysing magnet, which serves as a mass and charge separator. It only allows ions with a fixed magnetic rigidity p/q (ion momentum p and charge state q) to pass the magnet, so that one specific charge state produced in the stripping process can be chosen for the mass of interest. In addition to these ions of interest, other particles with the same impulse/charge state ratio (p/q or ME/q^2) pass through the magnetic field. This is possible due to the dissociation of molecules into fragments with different masses, energies, and charge state, but whose ratio (p/q) has the same magnetic rigidity as the ions of interest. The notations E, M, q, p stands for the energy, mass, charge, and momentum of the ion.

Due to the magnetic field the particle trajectory will be given by the equality of the two forces that appear, the Lorentz force and the centrifugal force, see Fig. 5.11:

$$qvB = \frac{mv^2}{R} \qquad \textit{Eq 5.6.}$$

where R is the analyser magnet radius, q is the charge, v is the velocity and m are the mass of the particle.

We then obtain the relation of magnetic rigidity, BR:

$$(BR) = \left(\frac{p}{q}\right) = ct. \qquad \textit{Eq 5.7.}$$

The kinetic energy is the same for all accelerated ions and is given by the relation:

$$E = E_{ext} + (q+1)U_T \qquad \textit{Eq 5.8.}$$

where E_{ext} is the extraction energy from the ion the source ($E_{ext} = e \times U_{ext}$), e is the elementary charge of the electron, and U_T is the high voltage applied on the terminal. In this case it means that particles that have the same ratio (m/q) can pass through the magnet even if they have different masses.

5.2.6. High Energy 120° Electrostatic Analyzer

To further remove unwanted particles that passed through the previous filters, it is necessary to use an additional filter. The most common are the speed filter (Wien filter), electrostatic analysers, energy attenuation foils, time of flight filters etc. The 1 MV Tandem™ is equipped with an electrostatic analyser which consists of two metal electrodes in the shape of a circle sector with a radius of curvature of 650 mm and a length of 2600 mm covering 120°. The electrodes are placed parallel to each other and positioned at 32 mm from each other. A voltage of the same value but of the opposite direction is applied to each electrode, thus forming a constant electric field.

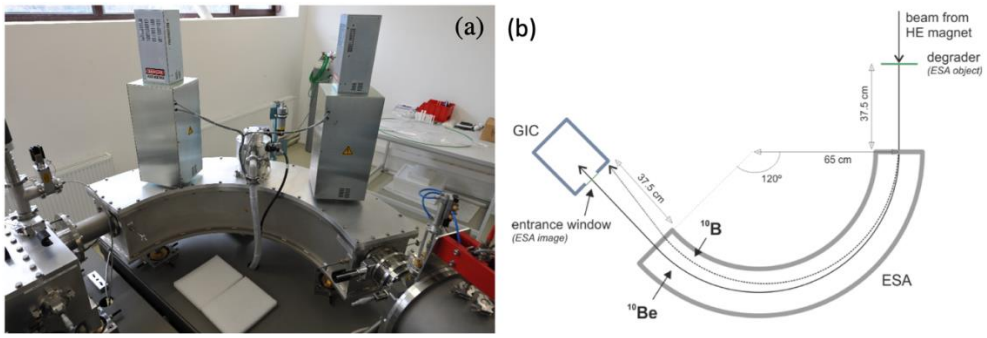

Figure 5.11. High Energy 120° Electrostatic Analyzer (Pacesila, 2019)

The trajectory of the particles passing through this electrostatic analyser is given by the balance of the electric force (qE) and the centrifugal force (mv^2/R). As in the case of the analyser magnet, the electrostatic analyser is also characterized by an electrical rigidity (E×R), given by the relation:

$$ER = 2\frac{E_{kin}}{q} \qquad \textit{Eq 5.9.}$$

where E is the electric field strength applied to the analyser plates, R is the curvature radius of the analyser, E_{kin} is its kinetic energy and q is the electric charge state of the particle.

5.2.7. Gas Ionization Chamber

The AMS method analyses an ion beam with a very low current intensity, ten particles per minute or even less. No instrument can measure this very small current, called the ion microscopic beam, except for the particle detector found at the end of the installation, which counts them one by one.

The detection system consists of a gas ionization chamber (GIC), a cylinder with a length of 46 cm and a radius of 16 cm, which is filled with gas, in this case the gas used is isobutane. The separation of the ionization chamber, in which

pressure of tens of mbar are set, from the vacuum of about 10^{-7}bar in the acceleration system, is done by means of a thin Si_3N_4 window. This window has thicknesses of the order of nm between 30 and 150 nm, an area of 8x8 mm^2 and can withstand pressures between 0 and 60 mbar, inside the ionization chamber.

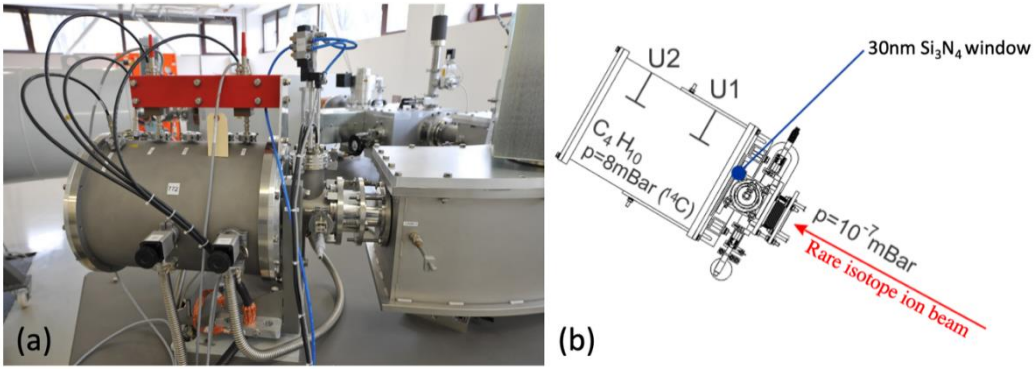

Figure 5.12. Gas ionization chamber (Pacesila, 2019)

The separation of ions at low energies (<3MeV) is based on the difference between their specific energy losses (dE/dx) as they pass through the gaseous medium. To measure these energies, the chamber is provided with two anodes, see Figure 5.13.

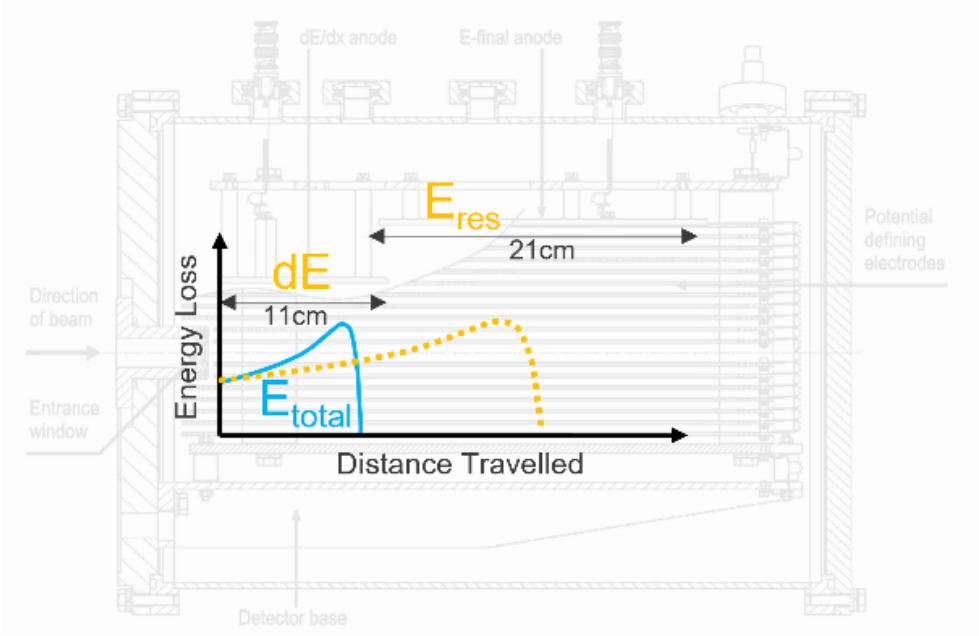

Figure 5.13. Schematic view of the Bragg curve and the GIC detector

The first anode is 11 cm long and is used to measure the energy lost by the particle when passing through the gas in its area and the second is 21 cm long, used to measure the residual energy of the particle. The electrical signal from these two

electrodes represents the current formed by the electrons that come from the ionization of the gas when the charged particle passes through it and is proportional to its energy loss. This proportionality is ensured by choosing proper operating conditions (nature and pressure of the gas, applied electric fields), which prevent recombination and/or uncontrolled multiplication of the load. Optimal ion separation is obtained when the intersection between the ion stops curves (dE/dx as a function of x, where x is the position along the way) takes place at the dividing margin between the electrodes. Using the two signals on the anodes, a bi-parametric graph is constructed (dE, Eres) that highlights the good separation between different ions, see Fig. 5.13. In figure 5.14 is shown a hand drawing of Prof. Shawn Bishop where can be seen how a bi-parametric spectrum is built when using a gas ionization chamber and how ions with different energies are identified.

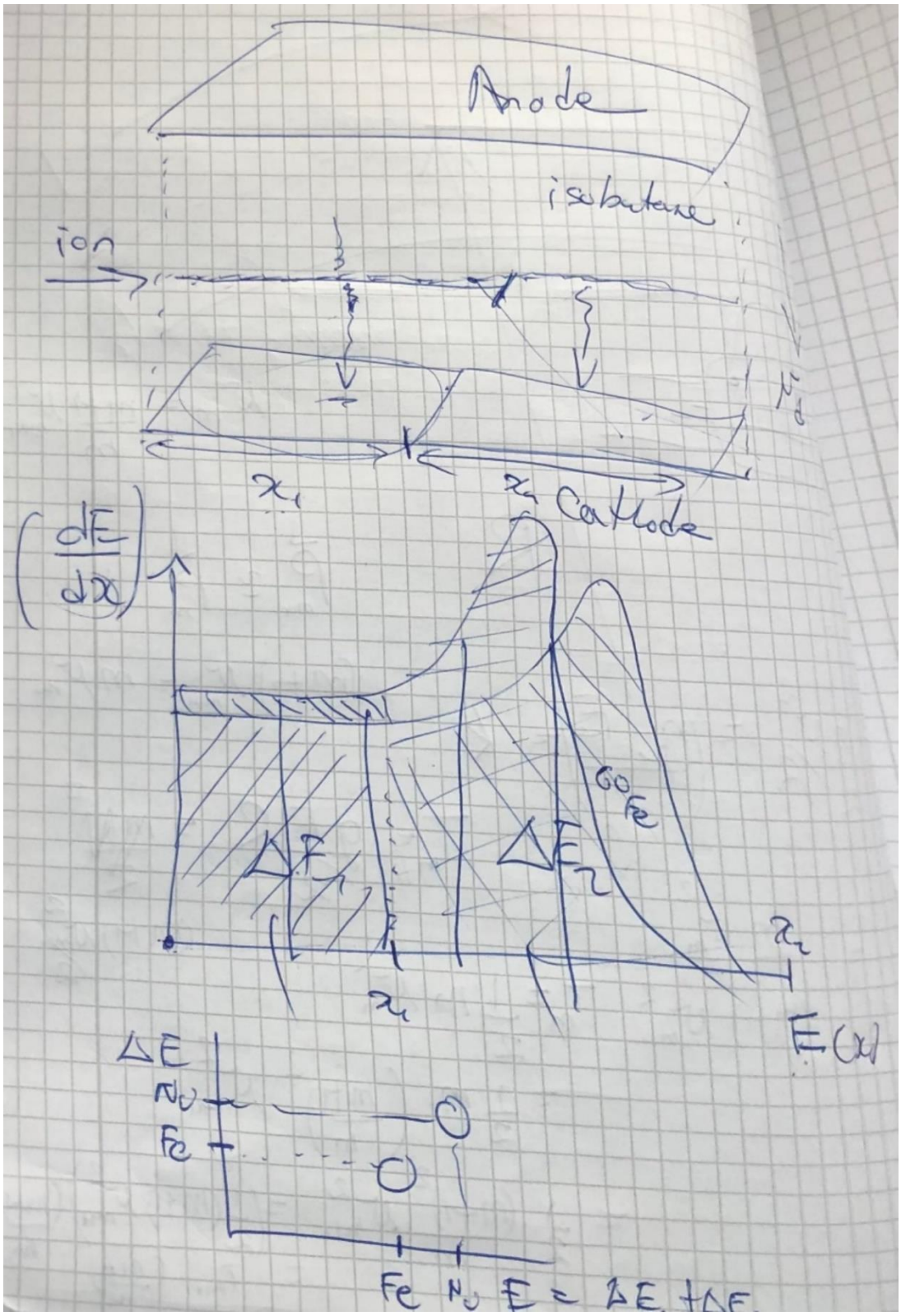

Figure 5.14. Schematic hand drawing by Prof. Shawn Bishop

5.3. Plutonium determination

Most of the AMS measurements were performed using the 1 MV Tandetron Accelerator installed at the Horia Hulubei National Institute for R&D in Physics and Nuclear Engineering (IFIN-HH) in Bucharest, Romania, while the 3 MV AMS Pelletron Tandem System installed at the CIRCE Laboratory, Caserta, Italy was used to test or to confirm several aspects, like the 0 background for the 244 mass.

The methodology followed while using the two accelerators is very similar and it will be presented unitarily and specific details for each accelerator are presented in table 5.1.

Table 5.1. Working parameters for 1MV HVE, IFIN-HH and for 3MV NEC, CIRCE when measuring ^{244}Pu

Accelerator/ Parameter	Injection Voltage [KV]	Terminal Voltage [MV]	q	T (%)	Positive Ion Energy [MeV]	time fraction AMS counting	Detector Window
1MV HVE, IFIN-HH	35	0.634	3+	10 - 11	2.53	82.8%	30nm (Si_3N_4)
3MV NEC, CIRCE	50	2.413	5+	3 - 5	14.37	71.4%	900nm (PETP)

5.3.1. Beam Tuning

The plutonium measurement by AMS is characterized by the fact that all the isotopes need to be quantified in the final detection system. Because Pu does not have any natural isotope, a reference isotope must be artificially added to the samples, ^{242}Pu in our case. The mass usually added is in the order of pg, which is insufficient to produce a beam of macroscopic intensity quantifiable currents in the Faraday cups. Therefore, we need to use another element as pilot beam to set up the ion beam trajectory through the AMS system from the ion source to the detector. In both laboratories ^{238}U is used as a pilot because it has a mass closer to that of plutonium isotopes and we can obtain ion beam intensities up to 10nA. All the optical and transport elements were optimized until a maximum intensity of the pilot beam current is achieved in the Faraday cup that is placed close to the detector.

As mentioned above, uranium and plutonium isotopes are extracted from the ion source as UO^- and PuO^-.

Usually, once the magnetic field of the low energy magnet has been set, we obtain a specific radius that the anion $^{238}U^{16}0$- is following, for a higher mass as the ones for plutonium isotope to follow the same trajectory the applied magnetic field should be changed. However, this is challenging as we would have to take hysteresis effects into account. To avoid this, the energy of the beam inside the low-energy magnet is temporarily modified, so that for a certain time interval the beam of a higher mass simulates the trajectory of the nucleus of lower mass and is injected into the accelerator. To fulfil this energy requirement a system known as a bouncer is used, which is basically a voltage source coupled to the magnetic sector, thus allowing the electrostatic potential of the magnet to be changed and, therefore, the energy of the beam.

The negative molecules are extracted from the ion source with an energy of 35 keV when using the 1 MV Accelerator, while for the 3 MV Accelerator the extraction energy is 50 keV, the uranium negative oxide is injected in the accelerator without using the bouncer, thus, to find out the vales of the bouncer system for the Pu negative molecules the following equation is used:

$$m(^{238}U^{16}O^-)\,V_0 = m(^{X}Pu^{16}O^-)\,(V + V_0) \rightarrow$$
$$V = \frac{V_0(m(^{238}U^{16}O^-) - m(^{X}Pu^{16}O^-))}{m(^{X}Pu^{16}O^-)} \qquad \textit{Eq 5.10.}$$

After the low energy magnet, the molecular ions are accelerated along the low energy column of the accelerator system reaching the stripper channel. In the stripper channel argon gas at low density is continuously flown. The collisions between the fast-negative particles and the argon atoms, leads to the breaking of negative molecules and stripping of electrons from the negative ions.

For the plutonium ions to be bent by the high energy magnet in the same way as the uranium ion without changing the magnetic field, the voltage applied on the accelerating tubes must be changed to ensure the same magnetic rigidity for all the positive ions of interest and the specific values for each isotope are listed in table 5.2.

Table 5.2. Accelerating voltages needed for all the Pu isotopes

Isotope (q=3+)	V_t (kV)	E (MeV)
^{238}U	650.5	2.561
^{239}Pu	647.7	2.550
^{240}Pu	644.9	2.539
^{242}Pu	639.6	2.518
^{244}Pu	634.3	2.498

Finally, the electrical field of the last kinematic filter (electrostatic analyser on the high energy side) must be changed for each isotope to compensate the energy differences introduced during the previous step and deliver all the masses into the detector. The values set for the electrostatic analyser are presented in table 5.3.

Table 5.3. The voltage applied on the electrodes of the electrostatic deflector

Isotope (q=3+)	HE ESA (kV)
^{238}U	33.561
^{239}Pu	33.421
^{240}Pu	33.281
^{242}Pu	33.006
^{244}Pu	32.736

After this step, to maximize the transport for the plutonium ions a fine tuning is performed using the reference isotope ^{242}Pu. The voltage applied on the terminal and on the ESA is changed inside a small range of values until a maximum of count rate is obtained into the detector.

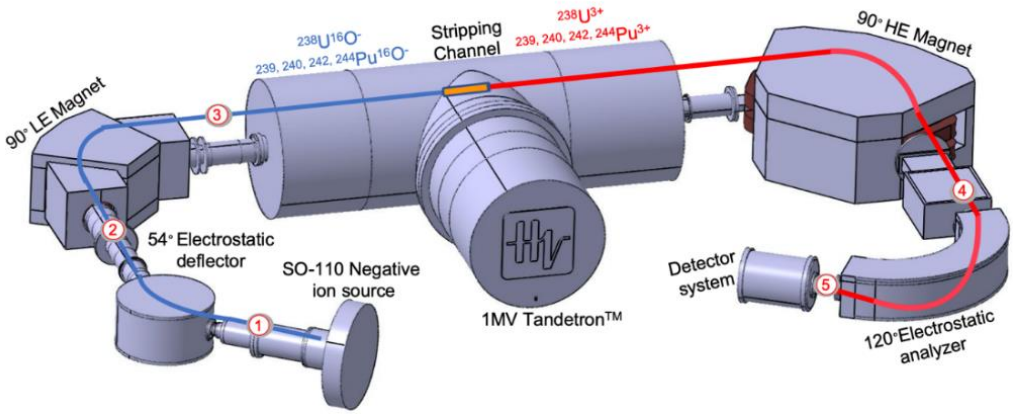

Figure 5.15. Transport of the pilot beam through the 1 MV system from IFIN-HH; The blue curve represents the trajectory of the negative ions $^{238}UO^-$, and the red curve represents the trajectory of the positive ions $^{238}U^+$. Faraday cups in which beam currents are measured are represented by red bullets (Courtasy of D. Pacesila)

For the 1MV Accelerator the ions are finally detected and measured in terms of total energy loss in a gas ionization chamber (GIC) provided with silicon nitride entrance window that has a thickness of 30nm to lower the energy loss straggling of the ions in the window. The $^{239, 240, 242, 244}$Pu isotopes are counted by using an automated slow sequential mode, that allows an injection time of ions in the range of hundreds of seconds.

5.3.2. Total efficiency

For high sensitive AMS measurements, especially for astrophysics application, a big challenge is to determine the overall detection efficiency of the system. This number quantifies what fraction of nuclides is transported from the target sample to the detector or to the movable faraday cup.

For the measurement of plutonium isotopes, we need a microscopic pilot beam that allows the identification of the right parameters for maximum ionic transport. In general, as pilot beam thorium– ^{232}Th (Hotchkis et al., 2019) or uranium – ^{238}U (Chamizo et al., 2008) is used.

Simultaneously with the detection efficiency study for plutonium we investigated which isotope is closer to the properties of the anthropogenic one. To do this we prepared several samples/cathodes with known quantities of each isotope, for the natural isotopes the quantities were in the order of tens of

micrograms and for Pu were a few picograms. The ^{238}U and ^{232}Th isotopes were measured as 3+ ion currents in the movable Faraday Cup. This Faraday cup is used because of its better sensitivity for nanoamperes beams and was positioned on the same trajectory of Pu isotopes. The current evolution in time was recorded and transformed to an expected number of particles for the time *t*, while plutonium isotopes were quantified in the Gas Ionization Chamber.

After the measurement of ^{238}U and ^{232}Th currents and subsequently obtaining the number of particles and the detected events of ^{242}Pu, the detection efficiencies were calculated by dividing the number of particles detected to the total number of particles in the target material. The results (table 5.4) are obtained as the mean for 2 or 4 cathodes and the uncertainty of the mean value was calculated as the standard deviation of the individual measurement from the mean.

Table 5.4. Detection efficiency of the 1MV Accelerator for ^{232}Th, ^{238}U, ^{242}Pu

Isotope	*Isotope quantity*	*Detection Efficiency from Ion source to FC3 (Movable Faraday Cup) / GIC (· 10^{-4})*
^{232}Th (2 cathodes)	~110 µg/cathode	1.43 ± 0.51
^{238}U (2 cathodes)	~60 µg/cathode	0.32 ± 0.03
^{242}Pu (4 cathodes)	~2pg/cathode	0.41 ± 0.07

The overall detection efficiencies of the 1MV Accelerator at IFIN-HH for three actinide species are listed in table 5.4 (Stanciu et al., 2022). The value for plutonium is closer to the one obtained for uranium, meaning that from the point of view of the chemical and physical properties the two isotopes are similar as stated, for example, in (Chamizo et al., 2008) and, in our case, for now on for Pu determination it will always be chosen as pilot beam. Based on the value obtained for ^{242}Pu and on the absence of background (at least for ^{242}Pu and for ^{244}Pu) we can estimate a limit of detection of ~10 atto-grams (10^{-17}g).

5.3.3. Sample order and isotope sequence

After the tunning procedure is completed, a routine AMS measurement can begin. The first step was to measure a plutonium standard with known isotopic ratios. Because is highly concentrated it was measured for much shorter times in the order of a few second until 100-200 counts of ^{244}Pu were recorded. Then, cathodes that contain only iron Oxide and Niobium are sputtered until no events

for ^{244}Pu mass are detected for several hours, also there are alternated cathodes with the blank mixture that is spiked with the reference isotope. In this manner we avoid any false positive events in the detector produced by the "memory effect" or the cross contamination of the ion source. After this cleaning step, the samples of interest are measured for 2-3 hours, with Pu-free samples in between the samples. At the end of the experiment, that usually can take up to 48 hours, the standard material is measured again. This step allows us to take into account any drift in transmission during the measurement. When dealing with very low statistic like in the case of ^{244}Pu determinations for astrophysics applications the time allocated for the measurement of this isotope is in the range of minutes. To ensure that it is taking in account any changes in the ion optics during the experiment the reference isotope is measured before and after as it follows: ^{242}Pu – 30s, ^{239}Pu – 30s, ^{240}Pu – 60s, ^{244}Pu – 725s and ^{242}Pu – 30s, this sequence is repeated until the sample material is exhausted.

For large number of events the uncertainty can be estimated as squared root of the number of events, where the number of events was larger than 20 as in the case of $^{239,\ 240\ \text{and}\ 242}$Pu isotopes, but for ^{244}Pu, for most of the samples the number of events is less than 20, therefore is used the confidence intervals and upper boundaries proposed by Feldman and Cousins, 1998 constructed using a likelihood ratio approach. More precisely, for all cases of <20 counts we calculate 2σ upper limits, that represent 95% confidence levels and they are listed in table.

Table 5.5. Confidence intervals depending on the number of events observed for 2σ intervals suggested by Feldman and Cousins (1998) for 0 background measurements

Events	U.L.	L.L.	Events	U.L.	L.L.
0	3.09	0.00	11	19.29	5.14
1	5.14	0.05	12	20.34	6.32
2	6.72	0.36	13	21.80	6.72
3	8.25	0.82	14	22.94	7.84
4	9.76	1.37	15	24.31	8.25
5	11.26	1.84	16	25.40	9.34
6	12.75	2.21	17	26.81	9.76
7	13.81	2.58	18	27.84	10.84
8	15.29	2.94	19	29.31	11.26
9	16.77	4.36	20	30.33	12.33
10	17.82	4.75			

After the measurement, all calculated isotopic ratios of the samples are corrected for any fractionation using the new plutonium standard ColPuS which is described in (Dittmann et al., 2015 and 2019) and it was kindly provided by Prof. Dr. Tibor Dunai and Dr. Erik Strub from Koln University. Although the plutonium isotopes are all counted in the same GIC, there can be introduced by an AMS system isotopic fractionation. This process introduces an uncertainty, which is much smaller than the statistical uncertainty. To correct for fractionation the measured isotopic ratios, during the ^{244}Pu experiments, we use at the beginning and at the end of the experiments the new plutonium standard.

The measurement efficiency is calculated using the total number of ^{242}Pu recorded and normalized by the time fraction of the AMS counting of this isotope and divided by the number of ^{242}Pu atoms added as spike to each sample (Wallner et al., 2015; Ludwig et al., 2016).

5.3.4. Plutonium Standard

After the successful measurement of the CNA Standard (Pacesila et al., 2020) which contains only ^{239,240,242}Pu, to advance with the plutonium measurements, especially for the examination of radionuclides of stellar origin, it was essential to measure the new plutonium Standard that includes ^{244}Pu.

For the isotopic ratios measurement, the plutonium isotopes were counted by using the Slow Sequential Injection method (SSI), the measurement sequence being ^{242}Pu 5s, ^{239}Pu 5s, ^{240}Pu 5s and ^{244}Pu 20s, each sequence was repeated 5x6 times.

The isotopic ratios were calculated according to Chamizo, 2008. For each 5 sequences an overall average of the total number of counts accumulated during the repetition for 5 times of the isotopes sequence was obtained as it follows:

$$r_j^X = \frac{n_j^X}{n_j^{242}} \cdot \frac{T^{242}}{T^X} \qquad \textit{Eq 5.10.}$$

Where $n_j^X = \sum_{i=1}^{5} N_i^X$, i is sequence, j is step, X is 242, 239, 240 or 244 and T^X – real measurement time in seconds. For each isotopic ratio is determined a statistical uncertainty (δ_j^X).

$$\delta_j^X = \sqrt{\frac{1}{n_j^X} + \frac{1}{n_j^{242}}} \cdot r_j^X \qquad \textit{Eq 5.11.}$$

The final isotopic ratios (r_{final}^{X}) are calculated as weighted mean of r_j^X, by giving more importance to the steps that had more counts of ^{242}Pu (reference isotope) by using a weighting factor (α_j).

$$r_{final}^{X} = \frac{\sum_{j=1}^{s} \alpha_j r_j^X}{\sum_{j=1}^{s} \alpha_j} \ , \alpha_j = n_j^{242} \cdot T_j^X \qquad \textit{Eq 5.12.}$$

The absolute error is the one that is greater between the statistical or internal error (δ^X), which is the result of applying error propagation, and the standard deviation of the weighted mean (σ^X) which informs about the stability of the experimental device, or external error.

$$\delta^X = \frac{\sqrt{\sum_{j=1}^{s} \left(\alpha_j \cdot \delta_j^X\right)^2}}{\sum_{j=1}^{s} \alpha_j} \qquad \textit{Eq 5.13.}$$

$$\sigma^X = \sqrt{\frac{\sum_{j=1}^{s} \alpha_j \cdot \left(r_j^X - r_{final}^X\right)^2}{\sum_{j=1}^{s} \alpha_j \cdot (N-1)}} \qquad \textit{Eq 5.14.}$$

The results (Stanciu et al., 2022) obtained for 7 sample targets measured in IFIN-HH are presented in table 5.6 together with the statistical or internal uncertainty (δ), and the standard deviation of the weighted mean or external uncertainty (σ).

Table 5.6. Isotopic results for individual cathodes of ColPuS Standard

	^{239}Pu/^{242}Pu			^{240}Pu/^{242}Pu			^{244}Pu/^{242}Pu		
Cathode number	ratio	σ (ext)	δ (int)	ratio	σ (ext)	δ (int)	ratio	σ (ext)	δ (int)
ColPuS1	1.033	0.053	0.017	1.039	0.054	0.028	0.0986	0.0063	0.0024
ColPuS2	1.025	0.042	0.016	1.042	0.043	0.014	0.0925	0.0048	0.0030
ColPuS3	1.029	0.045	0.025	1.052	0.046	0.023	0.0937	0.0052	0.0030
ColPuS4	0.955	0.047	0.013	1.001	0.049	0.017	0.0896	0.0056	0.0021
ColPuS5	1.034	0.038	0.015	1.077	0.039	0.021	0.0915	0.0042	0.0018
ColPuS6	0.991	0.049	0.021	1.004	0.049	0.016	0.0930	0.0057	0.0031
ColPuS7	0.985	0.048	0.008	1.008	0.048	0.012	0.0876	0.0054	0.0011

As expected, statistical error is smaller than the external one, because the latter one is expressing the stability of the AMS system during the extended measurement, and it should be always in the same way as this. The results show a

good precision, accuracy and consistency of our overall methodology, sample preparation and measurement, for both ratios $^{239}Pu/^{242}Pu$ and $^{240}Pu/^{242}Pu$ the external uncertainty is around 5%. For $^{244}Pu/^{242}Pu$ is slightly higher because the concentration of ^{244}Pu is one order of magnitude smaller and the measurement time was not scaled in accordance, it was only four times higher for ^{244}Pu compared to the time for the other three isotopes (Stanciu et al., 2022).

Table 5.7. Mean Isotopic Ratios for ColPuS Standard

Isotopic ratio	$^{239}Pu/^{242}Pu$	$^{240}Pu/^{242}Pu$	$^{244}Pu/^{242}Pu$
Measured, 1MV IFIN-HH 7 cathodes, this work	1.007 ± 0.030 (3.03%)	1.032 ± 0.028 (2.76%)	0.0924 ± 0.0035 (3.74%)
Mean normalized – 7 AMS LAB, [Dittmann et al., 2019]	1.067 ± 0.028 (2.62%)	1.076 ± 0.021 (1.95%)	0.1075 ± 0.0045 (4.18%)
Consensus values, [Dittmann et al., 2019]	1.058 ± 0.008 (0.08%)	1.066 ± 0.009 (0.83%)	0.1051 ± 0.0021 (2.0%)

The small differences between our ratios and the ones obtained by other AMS laboratories or the consensus values can be attributed to the fact that in our case, unlike the other centres, we did not have available the well-known UKAEA standard. In any case, the results obtained for the isotopic ratios considering a 2σ uncertainties (Table 5.7) show a good agreement with the values reported by 7 other AMS laboratories and with the consensus values of the standard reported in Dittmann et al., 2019.

5.3.5. Zero background

When dealing with the slow injection of the isotopes, the bouncer on low energy, the terminal voltage and ESA on high energy are adjusted for every mass analysed to gain the same kinetic energy and have the same magnetic rigidity. After setting the major and minor components of the AMS system with a beam of nanoamperes of ^{238}U, the terminal voltage and ESA are fine tunned using the reference isotope ^{242}Pu and check the region of interest of detection together with the other three isotopes of plutonium present in the plutonium ColPuS Standard.

In the case of the 1MV Accelerator the energies involved are low, the ions are stopped along the first anode of the two-anode detector, in figure 5.16 it is

shown the spectrums obtained for the reference isotope ^{242}Pu (green circles) and ^{244}Pu (red triangles) and with the rectangle is highlighted the region of interest.

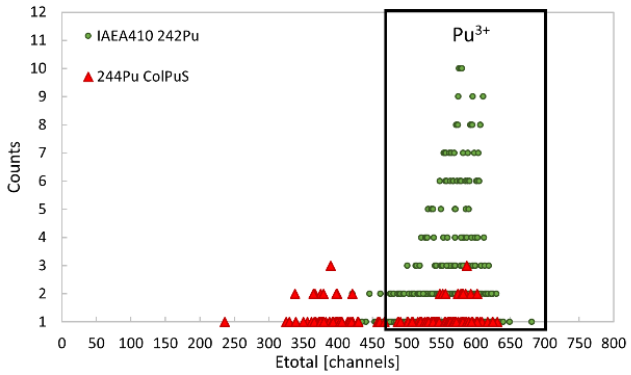

Figure 5.16. Total energy spectrum, obtained from GIC of the 1MV AMS system, for 2.53 MeV $^{242}Pu^{5+}$ (for IAEA 410 sediment sample, green circles) and $^{244}Pu^{5+}$ ions (for ColPuS Pu standard, red triangles)

Even if ^{244}Pu was present on earth 4.6 billion years ago, given its half-life it already decayed to undetectable levels therefore for mass 244 there is no natural background, also isobars are excluded based on the very short half-life from Neptunium to Mendelevium and the electronic noise for heavy ions is negligible since it has a contribution only to the resolution for the detection of light ions (Suter et al., 2007, Scognamiglio et al., 2016). Thus, the only aspect that can contribute to a false positive signal is the cross-contamination of the ion source. Therefore, special care was taken in order to examine the memory effect of the source after the sputtering of the concentrated standard by run a cathode that contains only iron oxide mixed with niobium for several hours with no background confirmed, the spectrum recorded being presented in figure 5.17, left side.

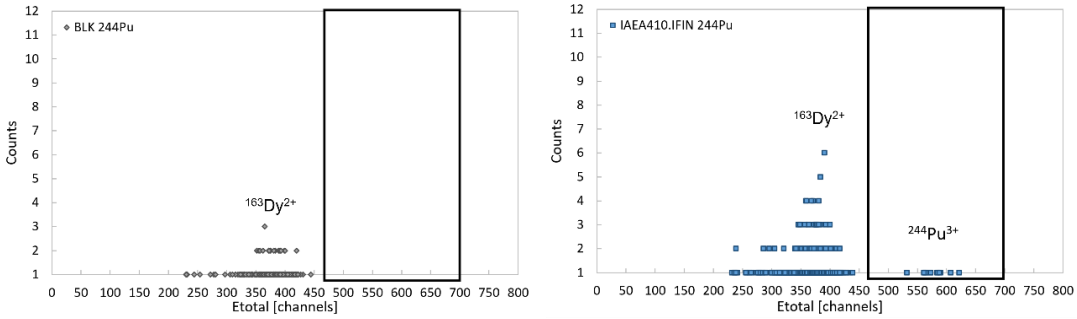

Figure 5.17. Total energy spectrums, obtained from GIC of the 1MV AMS system, for 2.53 MeV $^{244}Pu^{3+}$ ions and 1.69MeV $^{163}Dy^{2+}$, in the left side – blank sample measured for 3 hours before the sample and in the right side – IAEA 410 sediment sample measured for 2.5 hours

The plutonium ions arrive in the gas ionization chamber with an energy of 2.53MeV, but at the same time arrive also molecular fragments that have the same Mass/ charge ratio, in this case, for the ion with the mass 244 and 3+ charge, the interfering ion is the natural, stable Dysprosium isotope with the mass 163 and 2+ charge state. Fortunately, based on their energy, according to the Bethe-Bloch equation they can be distinguished because Dy arrive with a smaller energy, of 1.69MeV, and stopes quicker in gas compared to the plutonium Isotope that has a higher final energy. Another advantage of our system is the use of an extreme thin silicon nitride window of 30nm and the discrimination between $^{244}Pu^{3+}$ and the interfering $^{163}Dy^{2+}$ ions is very good, as shown in figure 5.18, right side spectrum that resulted from the measurement of the Bikini Atoll sediment. We suspect that the source of dysprosium is the cathode material because it was noticed that the count rate of it is increasing in time while the count rate of the reference plutonium isotope is decreasing during the exhaustion of the target material.

To further test the zero-background measurement for the mass 244, the measurement of the IAEA standard sediment was performed also at higher energy using the 3MV NEC Accelerator installed at CIRCE Laboratory, Italy.

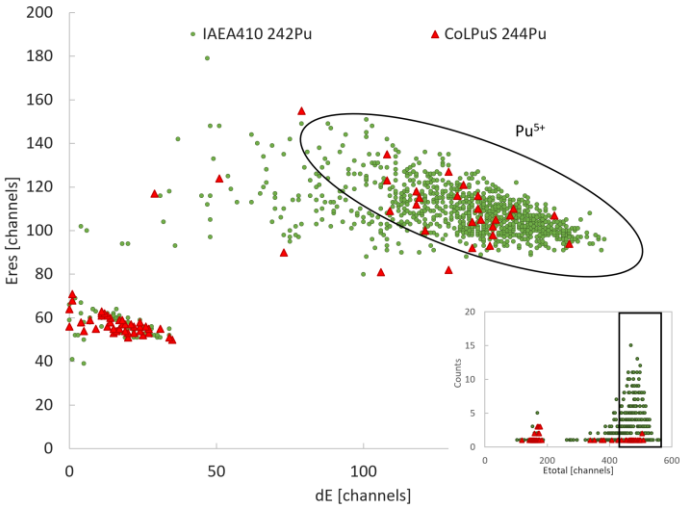

Figure 5.18. Two dimensional Eres – dE and Total energy (minimized) spectrums, obtained from GIC of the 3MV AMS system, for 14.37 MeV $^{242}Pu^{5+}$ (for IAEA 410 sediment sample) and $^{244}Pu^{5+}$ ions (for ColPuS Pu standard)

In figure 5.18 are presented the spectrums for the reference isotope and for ^{244}Pu while measuring IAEA sediment and ColPuS Standard with the corresponding spectrum that show the total loss of energy that is like the one obtained at lower energy at IFIN-HH.

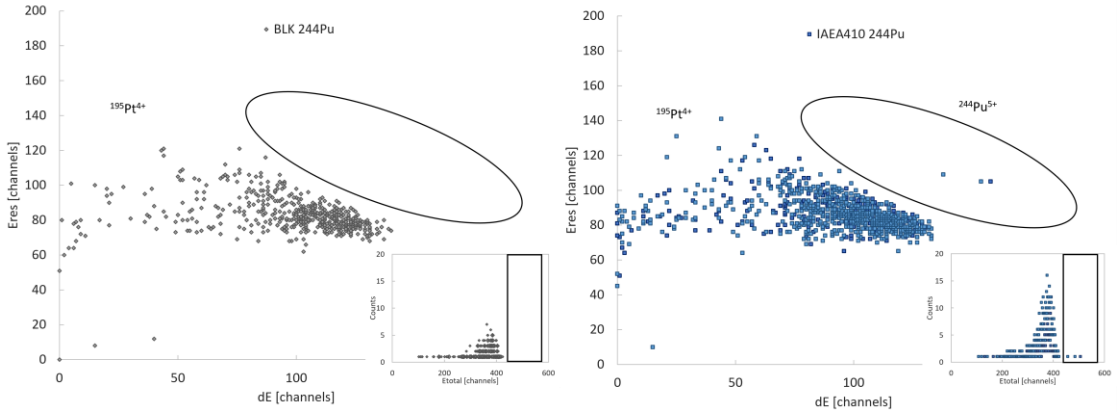

Figure 5.19. Two dimensional Eres – dE and Total energy (minimized) spectrums, obtained from GIC of the 3MV AMS system, for 14.37 MeV $^{244}Pu^{5+}$ ions and 11.50 MeV $^{195}Pt^{4+}$, in the left side – blank sample measured for 2 hours before the sample and in the right side – IAEA 410 sediment sample measured for 2.25 hours

The selected charge for plutonium measurement at CIRCE is 5+, thus the mass-charge ratio is 48.8, consequently the interfering ion being $^{195}Pt^{4+}$ that can be very well separated in the biparametric spectrum that plots dE-E_{res}. As expected, after running the measurement sequence several times while the cathode with blank material was used, in the marked region of interest no events were detected, though when the IAEA sediment was measure 3 events were recorded. These results plotted as total energy loss versus counts clearly demonstrate that either way is a useful instrument for the ultrasensitive, background free determination of ^{244}Pu (Pacesila et al., 2022).

6. Results and discussion

All biologically formed structures described in previous sections were analysed for plutonium context with AMS. The results for the microbialite, stromatolites and oncolites are presented in a quasi-chronological manner in connection with the accumulated knowledge concerning the sample preparation and measurement. Additionally, an overview is given of the results obtained for reference materials measured together with the samples of interest and the outcome of an Intercomparison exercise organized by IAEA (International Atomic Energy Agency). The samples received were chemically processed by using the part of the procedure developed as a part of this work.

For the samples analysed for the IAEA Intercomparison and for ^{239}Pu concentrations the error given is 1σ, while for all the other results, in terms of isotopic ratios, all uncertainties take only statistical errors into account and are given as 2σ confidence intervals.

To explain or to support some findings, for different samples some complementary analyses were performed, like Gamma Spectrometry, Scanning Electron Microscopy (SEM) and/or Energy-Dispersive X-ray analysis (EDX).

6.1. IAEA Reference Materials at IFIN and CIRCE

While performing the AMS ^{244}Pu experiments for nuclear astrophysics purposes almost every time one or two reference materials from IAEA was processed and measured. All the results obtained during the experiments performed for astrophysics are summarized in table 6.1 and 6.2.

A first observation that can be drawn is that for both AMS systems the measurement efficiency is in the order of 10^{-4}, with higher values when the measurement time was smaller. Another aspect, even if the ion sources designs are different, the Caesium temperature was much higher when using the 1MV Accelerator, around 120°C compared to the temperature used during the experiments at CIRCE which was 95-100°C, so the ionization process was different. From the data it seems that the detection efficiency is similar, but the sputtering process behaved differently. At IFIN in the first hour the count rate for the reference isotope was higher and in the second part of the measurement decreased by around 70 to 90% but we continued until the exhaustion of the cathode in 2.5 hours. At the same time, when keeping a lower flux of Caesium like we did during the experiments at CIRCE the count rate of ^{242}Pu was during the first cycle higher

(~1cps) and then, from the second cycle it has stabilized to around ~0.3cps until the measurement was stopped after 2.25 hours, because by continuing the measurement we would only improve slightly the uncertainty. This behavior of iron oxide mixed with niobium was also observed in (Zhao and Francisco, 2022) where it was stated that this type of mixture has low sputter rates and to measure efficiently the target material in around 2 hours high fluxes of Cs+ was needed.

Table 6.1. Detailed data for sediment samples (IAEA410 – Bikini atoll and IAEA412 – Pacific Ocean), obtained with the 1MV HVE Accelerator (IFIN) and 3MV NEC Accelerator (CIRCE)

Sample	^{242}Pu at added	Measurement time Total/^{244}Pu [sec]	^{244}Pu events	Measurement efficiency (10^{-4})	^{244}Pu [atto-gram/g]
IAEA410.1 IFIN	$1{\cdot}10^8$	4369/ 3495	27 ± 10.4	0.83	321.9 ± 123.9
IAEA410.2 IFIN	$6{\cdot}10^8$	6796/ 5631	$18^{+9.84}_{-7.16}$	0.33	$746.0^{+407.8}_{-296.8}$
IAEA410.3 IFIN			26 ± 10.19	0.57	499.1 ± 195.8
IAEA410.4 IFIN			$15^{+9.31}_{-6.75}$	0.39	$496.4^{+308.1}_{-223.4}$
IAEA410.5 IFIN		8495/ 7039	$11^{+8.29}_{-5.86}$	0.55	$264.5^{+199.3}_{-140.9}$
IAEA410.6 IFIN	$5{\cdot}10^8$		$7^{+6.81}_{-4.42}$	0.26	$352.3^{+342.8}_{-222.5}$
IAEA410.7 IFIN			$13^{+8.8}_{-6.28}$	0.33	$519.8^{+351.8}_{-251.1}$
IAEA410.1 CIRCE			$3^{+5.25}_{-2.18}$	0.22	$143.5^{+251.1}_{-104.3}$
IAEA410.2 CIRCE		8600/ 5600	$4^{+5.76}_{-2.63}$	0.17	$257.2^{+370.4}_{-169.1}$
IAEA412.1 IFIN	$1{\cdot}10^8$	4369/ 3495	$8^{+7.29}_{-5.06}$	0.62	$16.7^{+15.2}_{-10.6}$
IAEA412.2 IFIN			$8^{+7.29}_{-5.06}$	0.57	$21.4^{+19.5}_{-13.6}$
IAEA412.3 IFIN	$5{\cdot}10^8$	8495/ 7039	$14^{+8.94}_{-6.16}$	0.47	$40.6^{+25.9}_{-17.8}$
IAEA412.4 IFIN			$7^{+6.81}_{-4.42}$	0.51	$18.4^{+17.9}_{-11.6}$

In terms of ^{244}Pu concentration, the results showed levels of hundreds of atto-grams per gram of sediment and for the sediment from Pacific Ocean the level is in the order of few tens of atto-grams/g, one explanation could reside on the fact that during the nuclear test, the atomic bombs exploded on the Bikini Atoll island, while the Pacific Ocean received plutonium from several sources, like nuclear tests or local accidents therefore plutonium was diluted by the water body and subsequently deposited on the bottom of the ocean so is understandable the lower concentration.

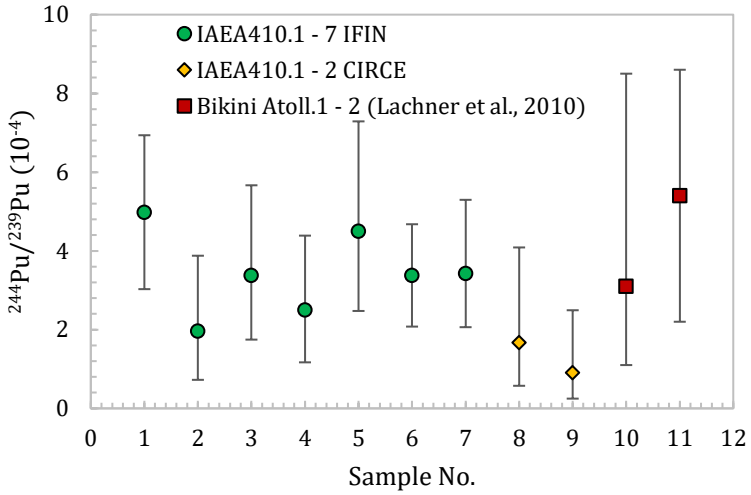

Figure 6.1. $^{244}Pu/^{239}Pu$ isotope ratios with 2σ uncertainties for the Bikini Atoll sediment measured at IFIN, Romania or at CIRCE, Italy and values from Lachner et al., 2010

In figure 6.1 the values for the isotopic ratio of $^{244}Pu/^{239}Pu$ for the IAEA410 samples processed and measured by two AMS systems for this work together with values from other representative project, for sediments samples extracted from different locations from Bikini Atoll Island are presented. In general, the results are in fine agreement inside the 2σ limits, and they validate the overall methodology. The same information can be extracted also from figure 6.2, where the results obtain at IFIN in comparison with a value given by Wallner et al., 2015 are presented and they are as well in good agreement.

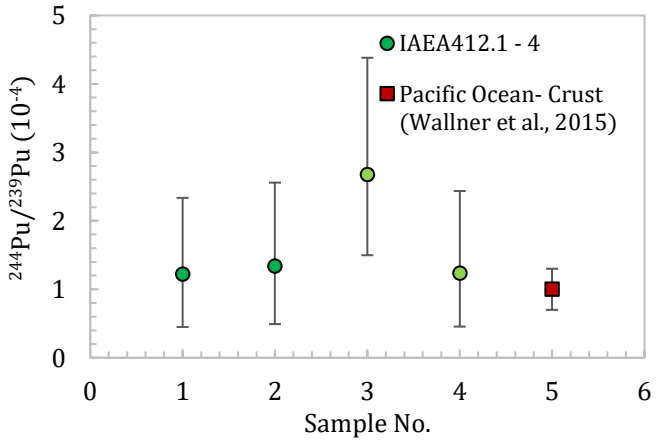

Figure 6.2. $^{244}Pu/^{239}Pu$ isotope ratios with 2σ uncertainties for the Pacific Ocean sediment measured at IFIN, Romania and values from Wallner et al., 2015

As a result of this study, an important information, in particular, for these reference materials a new information can be given, namely, the $^{244}Pu/^{239}Pu$ ratio

equal to $3.44^{+0.77}_{-0.59} \times 10^{-4}$ for IAEA-410, while for the other sediment, IAEA-412 is equal to $1.62^{+0.66}_{-0.45} \times 10^{-4}$.

Table 6.2. The isotopic ratios for $^{244}Pu/^{239}Pu$ with 2σ uncertainties (using the confidence level given in Feldman and Cousins, 1998) and $^{240}Pu/^{239}Pu$ with 1σ uncertainties

Sample/ Code	$^{244}Pu/^{239}Pu$ ($\cdot 10^{-4}$)	$^{240}Pu/^{239}Pu$
IAEA 410.1 IFIN-HH, this work	3.38 ± 0.65	0.250 ± 0.024
IAEA 410.2 IFIN-HH, this work	$3.42\ ^{+1.87}_{-1.36}$	0.265 ± 0.026
IAEA 410.3 IFIN-HH, this work	4.98 ± 0.98	0.259 ± 0.024
IAEA 410.4 IFIN-HH, this work	$4.50\ ^{+2.79}_{-2.02}$	0.218 ± 0.023
IAEA 410.5 IFIN-HH, this work	$2.50\ ^{+1.89}_{-1.33}$	0.226 ± 0.022
IAEA 410.6 IFIN-HH, this work	$3.38\ ^{+2.29}_{-1.63}$	0.290 ± 0.069
IAEA 410.7 IFIN-HH, this work	$1.97\ ^{+1.91}_{-1.24}$	0.265 ± 0.064
Bikini Atoll, Island, BL5 (Lachner et al., 2010)	$3.1\ ^{+5.4}_{-2.0}$	0.319 ± 0.026
Bikini Atoll, Island, BL6 (Lachner et al., 2010)	5.4 ± 1.6	0.323 ± 0.011
IAEA 410, CNA Seville, Spain (Chamizo et al., 2015)	/	0.257 ± 0.023
IAEA 412.1 IFIN-HH, this work	$1.22\ ^{+1.11}_{-0.77}$	0.194 ± 0.021
IAEA 412.2 IFIN-HH, this work	$1.34\ ^{+1.22}_{-0.85}$	0.191 ± 0.018
IAEA 412.3 IFIN-HH, this work	$2.65\ ^{+1.69}_{-1.17}$	0.156 ± 0.016
IAEA 412.4 IFIN-HH, this work	$1.23\ ^{+1.20}_{-0.78}$	0.168 ± 0.017
IAEA 412, CNA Seville, Spain (Chamizo et al., 2015)	/	0.182 ± 0.015
Pacific Ocean, deep-sea manganese crust (Wallner et al., 2015)	1.0 ± 0.3	/

As mentioned in previous sections, all the plutonium isotopes were measured, and the mean value for the isotopic ratio $^{240}Pu/^{239}Pu$ was inferred. For the Bikini Atoll sediment is 0.253 ± 0.015, while for Pacific Ocean is 0.177 ± 0.009. Individual values corresponding to each cathode can be found in Table 6.2.

6.2. ^{239}Pu AMS quantification – IAEA Intercomparison Exercise

The swipe sample idea appeared in the 1990s when a nuclear facility in Iraq was blasted and there was no possibility to collect regular samples from the devastated site (Szeles et al., 2010). Therefore, the IAEA inspectors had to be creative and used cotton wipes to "swipe" objects from the destroyed facility to test whether there were any remnants of the type of elements used in the facility before its destruction. Nowadays, swipe samples are not only used for nuclear forensics purposes but also for laboratory surface contamination when working with radioactive isotopes. In any case, IAEA performs regular proficiency tests or intercomparison exercises to test the capabilities of the designated laboratories.

In September 2021 the AMS laboratory in IFIN received several samples like water, bamboo and swipe samples. Since the control swipe sample (S8 Swipe) had a known concentration of ^{239}Pu, together with other two unknown swipe samples (S7a and S7b Swipe) were processed using the plutonium separation developed for the present project. For each sample two cathodes were produced, the individual results are presented in the following tables. For each cathode we obtained a value and its corresponding error, while each sample type we obtained the arithmetical average and the equivalent error and standard deviation by performing error propagation.

Table 6.3. AMS results for the control sample

Sample	^{239}Pu [Bq/sample]
S8.1 Swipe	5.71 ± 0.23
S8.2 Swipe	6.34 ± 0.34
Average	6.03 ± 0.31
Std. Deviation	0.40
Control Value	6.05 ± 0.25

The value obtained in our laboratory, 6.03 ± 0.31, for the control sample is in good agreement with the value reported in the introductory file of 6.05 ± 0.25.

Table 6.4. Radioactivity AMS results for the unknown samples

Sample	^{239}Pu [Bq/sample]
S7a.1 Swipe	7.22 ± 0.29
S7a.2 Swipe	7.79 ± 0.35
Average	7.51 ± 0.28
Std. Deviation	0.45
S7b.1 Swipe	8.21 ± 0.33
S7b.2 Swipe	7.64 ± 0.36
Average	7.93 ± 0.28
Std. Deviation	0.49
Average/ Reported Value	7.72 ± 0.67

For the unknow samples, S7a and S7b Swipe, as suggested by IAEA, an average value of 7.72 ± 0.67 was reported, the uncertainty is the standard deviation of the mean.

Following the data analysis of the results reported by all laboratories involved in the proficiency test, in Mauring et al., 2021 a target value for Sample 7 of 7.64 ± 1.34 is given. The result reported by our laboratory received a Z-score of 0.06, the z-score being calculated as following:

$$z = \left| \frac{Value_{reported} - Value_{target}}{target_{SD}} \right| \qquad \textit{Eq 6.1.}$$

This result represents an independent confirmation that, at least partially, the chemical procedure and AMS measurement are accurately performed.

6.3. Atacama Desert. Microbialite

Before the AMS measurement, the Atacama microbialite was investigated by gamma spectrometry to determine the gamma rays resulted from the decay chain of the natural actinides, 232 - Th, 238 and 235 – U or their daughters. The purpose of this analysis is to quantify Th and U isotopes and to check if the parent isotopes are in secular equilibrium with their daughters for this sample. In the following section the Gamma Spectrometry method and results are presented, as well the Pu AMS findings.

6.3.1. Gamma Spectrometry

When the solar system was formed, the earth incorporated 92 elements, among them ones of most important natural radioactive isotopes are ^{238}U, ^{235}U, ^{232}Th and ^{40}K.

Uranium and thorium are unstable isotopes; they mainly disintegrate by the emission of an alpha particle. Natural uranium is composed of three isotopes with very long half-lives, ^{238}U (99.25%), ^{235}U (0.72%) and ^{234}U (0,006%, product of ^{238}U decay series). Natural thorium has only one isotope which is ^{232}Th. Each of these isotopes disintegrates leading to the formation of a whole series of radioactive isotopes ending with the formation of a stable isotope of lead (figure 6.3, 6.4 and 6.5).

Under normal conditions, in a natural material, the activity ratio of $\Lambda_{235U}/\Lambda_{238U}$ will be fixed and all radioisotopes in each decay series will be in balance equilibrium, termed secular equilibrium.

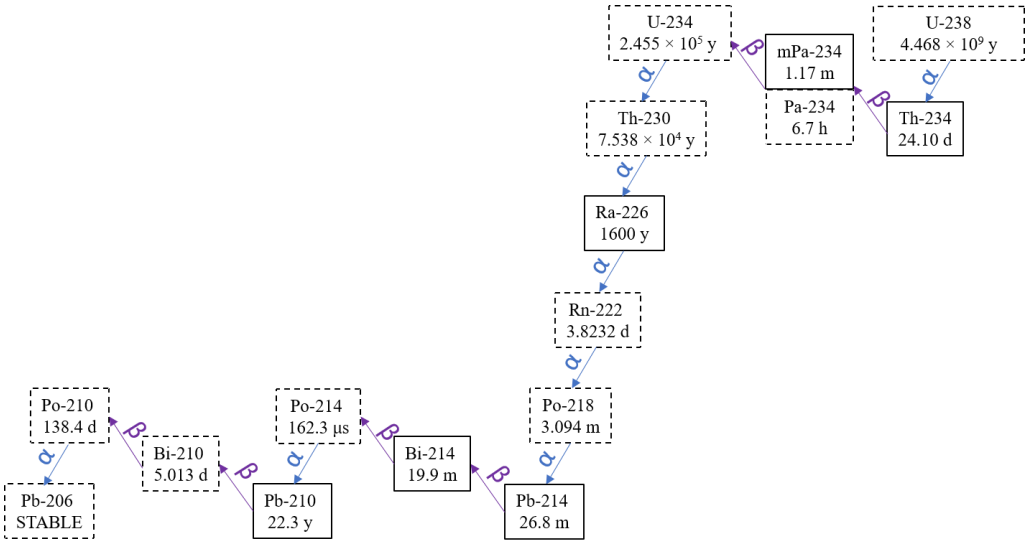

Figure 6.3. Uranium 238 decay series

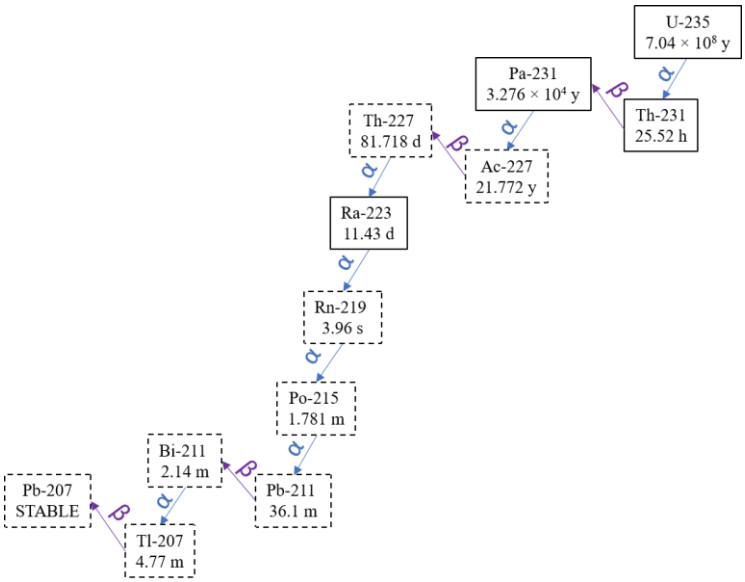

Figure 6.4. Uranium 235 decay series

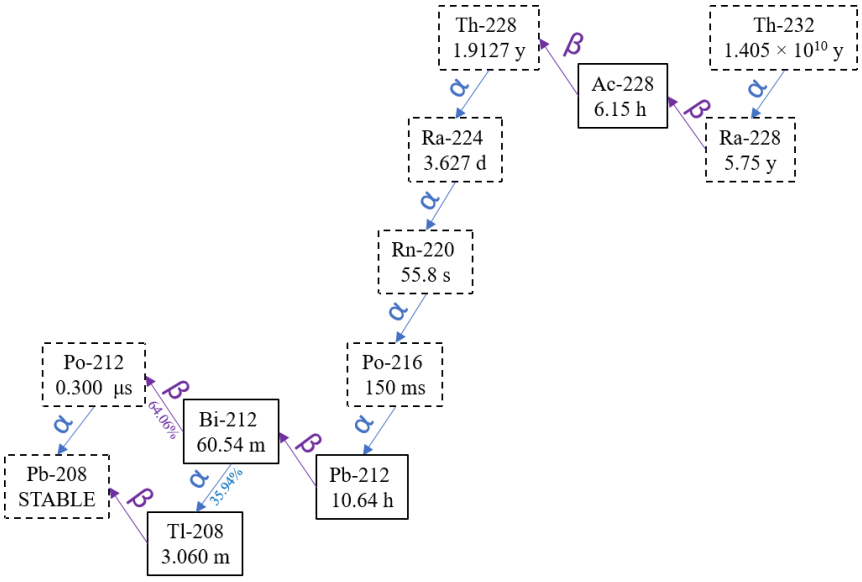

Figure 6.5. Thorium 232 decay series

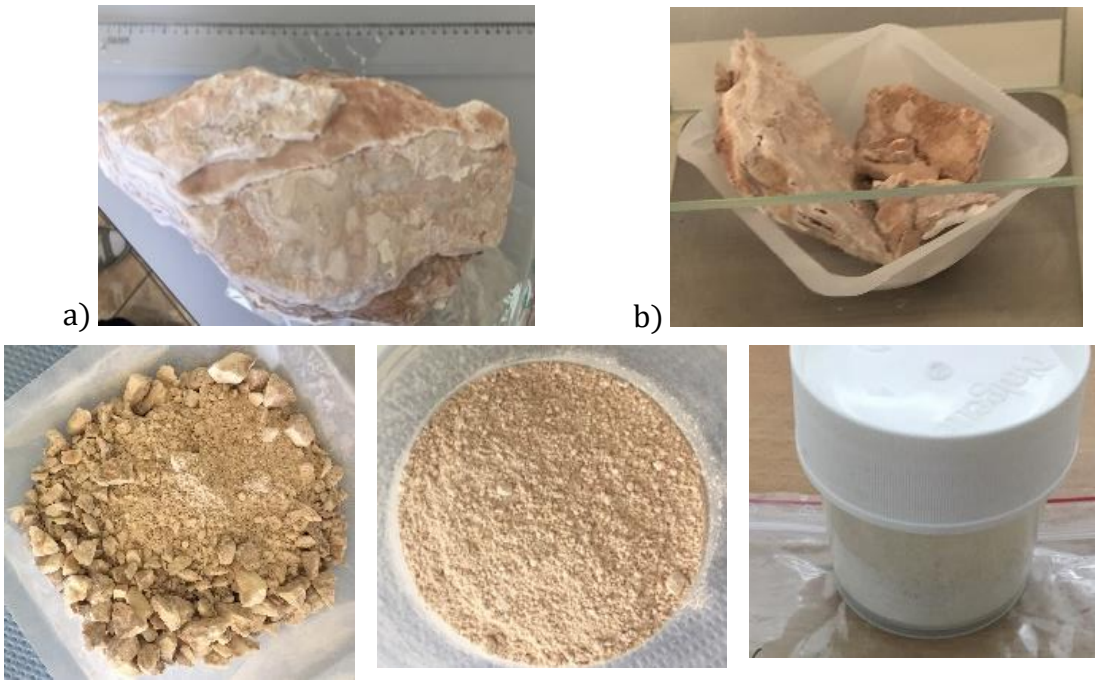

a) b)

a) b) c)

Figure 6.6. MFQBR36 sample analysed by Gamma Spectrometry. Sample preparation. One part of the MF QBR36 (a) sample was crushed with a hammer (b), smashed in a stainless-steel mortar (c) and finely ground by a ball mill (d). Finally, the powder obtained (118.5g) was transferred to a 125mL plastic container (e)

The sample was measured by high-resolution gamma spectrometry with a CAMBERRA detection system made up of the HPGe detector XtRa with a relative efficiency of 120% and energy resolution FWHM of 2.1 keV for the 1.33 MeV line of 60Co, HV 5000 V, U-type, housed in a radiation protection shield, Inspector 2000 plus a specialized software GENIE-2000 installed on a PC. The measurement was carried out in the underground microBq laboratory with ultralow radiation background, situated in the salt mine in Slanic-Prahova, Romania (Margineanu et al., 2008).

The radiation protection shield is made of (int.→ext.): 50mm electrolytic Copper OFHC, 100mm Lead containing < 25 Bq / kg of ^{210}Pb and 50mm recent Lead. The radiation background measured inside the protection shield is approx. 4000 times lower than the natural background measured with the same detector unshielded on ground on the energy range of between 40 keV and 3000 keV.

Calibration in efficiency was done with IAEA444 soil as standard material and Geometry Composer application from GENIE-2000 software. The software used for determining the efficiency calibration and the activity of all radionuclides

identified in the sample was Canberra ISOCS-LABSOCS mathematical calibration software.

To calculate the specific activity for each isotope identified in the obtained spectrum was used the following formula:

$$\Lambda = \frac{A_n}{mT_a\eta\varepsilon} \qquad \textit{Eq 6.1.}$$

Where: Λ – specific activity [Bq/kg].

A_n – net area of analysed peak [counts].

m – mass [kg].

T_a – acquisition time [s].

ε – efficiency.

The specific activities calculated for each isotope are listed in table 1.

Table 6.5. Specific activity of each isotope identified in the sample spectrum

Isotope	Activity [Bq/kg]	Uncertainty [Bq/kg]
^{40}K	60.68	1.78
^{234}Th	30.00	1.50
^{234m}Pa	39.41	3.33
^{226}Ra	33.94	4.69
^{214}Pb	29.79	0.70
^{214}Bi	27.16	0.27
^{210}Pb	19.01	2.54
^{235}U	1.83	0.18
^{231}Th	3.96	0.32
^{231}Pa	1.85	0.71
^{228}Ac	3.70	0.09
^{212}Pb	3.66	0.19
^{212}Bi	2.31	0.15
^{208}Tl	1.16	0.04

To calculate the concentration of each natural radioisotope, it must be checked if the secular equilibrium was kept for this sample. The empirical value of the activities ratio between ^{235}U and ^{238}U is equal to 0.0459. Under normal circumstances, in a natural material all nuclides in each decay series shuuld be in equilibrium. Since the activity of ^{235}U was determined, for ^{238}U the activity of ^{234m}Pa

was used, because it has the gamma rays in a range of energies where the efficiency of the detector is better compared with the energies of gamma rays of ^{234}Th. The activities ratio between ^{235}U (1.83 ± 0.18 Bq/kg) and ^{234m}Pa (39.41 ± 3.33) is equal to 0.0464 ± 0.0061. Once checked if the experimental value is close to the theoretical value, the concentrations were calculated with the following formula:

$$m_i = \frac{A_r \frac{\Lambda}{\lambda}}{L} \qquad \textit{Eq 6.2.}$$

Where: m_i – mass concentration of isotope [mg/kg, ppm].

A_r – relative atomic mass number [g/mole].

Λ – specific activity [Bq/kg].

λ – decay constant or decay rate [1/s].

$L = 6.022 \times 10^{23}$ is Avogadro's constant'[particle/mole].

The mass concentration for each natural radioactive nuclide is listed in table 6.6.

Table 6.6. Mass concentration of the natural radioactive nuclides

Isotope	Mass concentration [mg/kg, ppm]	Uncertainty [mg/kg, ppm]
^{238}U ($\Lambda_{238U} = \Lambda_{234mPa}$)	3.1612	0.2671
^{235}U	0.0229	0.0023
^{232}Th ($\Lambda_{232Th} = \Lambda_{228Ac}$)	0.9113	0.0222
^{40}K	0.2327	0.0068

The Gamma Spectrometry results, such as the concentrations for uranium and thorium, confirm the results obtained by performing ICP-MS analysis which are presented in table 3.2, for uranium ~3ppm while for thorium a concentration of around 0.9ppm was obtained. As mentioned before, for each parent isotope the activities of several daughters were measured, activities that are equal to the parents radioactivities.

In natural systems, exposed to atmosphere and precipitations, the secular equilibrium can be broken by selective dissolution and /or later precipitations. For example, if we consider the decay chain of ^{238}U, the radium isotope, ^{226}Ra, is much more soluble than the thorium isotope, ^{230}Th, therefore if the carbonate structure is not a closed system, these isotopes would be washed out from the structure differently, therefore the secular equilibrium would be broken. This aspect would be an issue for Pu measurement, for instance, if reprecipitations would happen

inside the carbonate structure there would be difficult to judge the anthropogenic contribution to the final result.

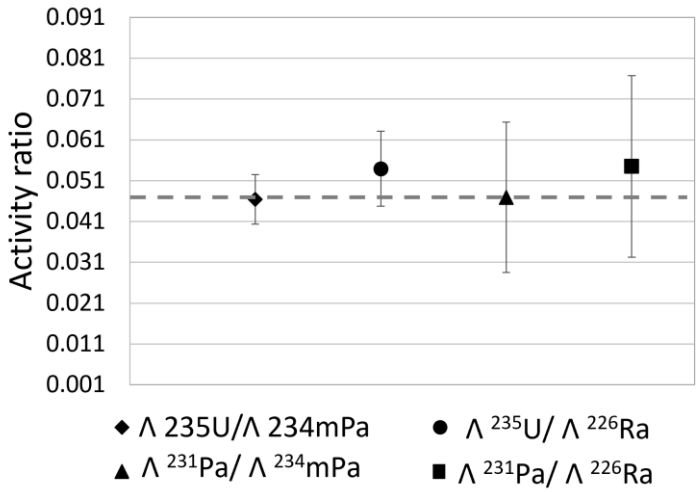

Figure 6.7. Experimental values for activity ratios and the empirical value (dotted line

In order to check if the natural uranium isotopes determined by measuring the Atacama Microbialite are in secular equilibrium across their decay chains, in figure 6.7 various activities ratios are represented by using different combinations of daughter-parent activities ratios. The empirical value is inside 1σ for all the ratios plotted in figure 6.7. This result supports the assumption that the Atacama microbialite is a closed system.

6.3.2. Plutonium isotopic ratios

The microbialite presents a laminated structure formed both by biological and evaporation processes. In figure 6.8 a thin section of the Atacama sample is presented where different layers that form the microbialite are highlighted, like primary calcite, secondary silica that could precipitated from the water body and detritial input that was trapped during the growth of the microbialite.

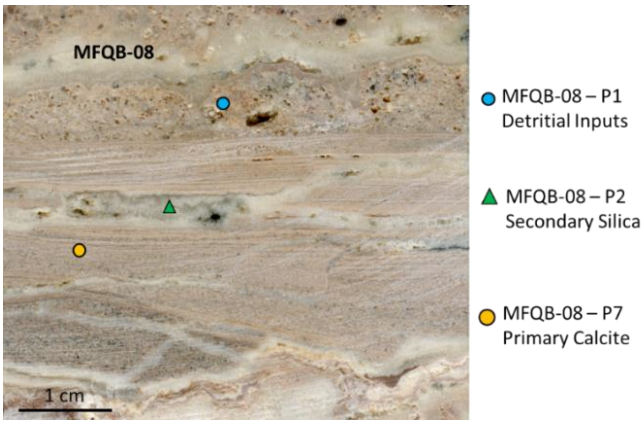

Figure 6.8. Thin section of Atacama Microbialite

To further examine the microstructure and composition of this sample, scanning electron microscopy together with elemental determination by EDX were performed, targeting to confirm the regions with primary calcite and secondary silica.

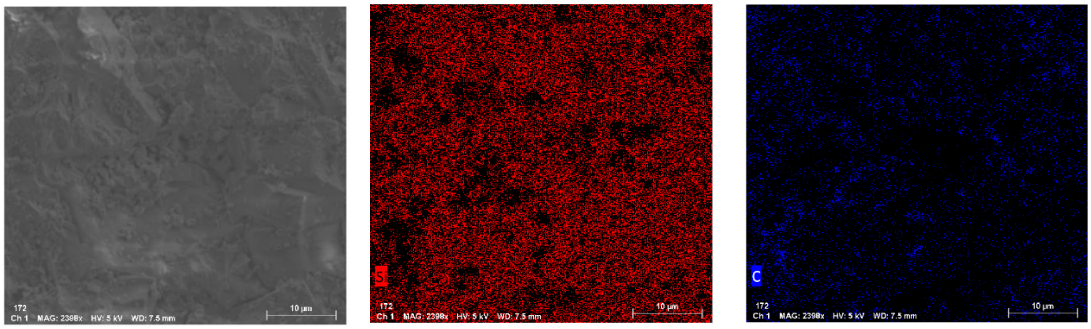

Figure 6.9. SEM Images and EDX maps of secondary silica

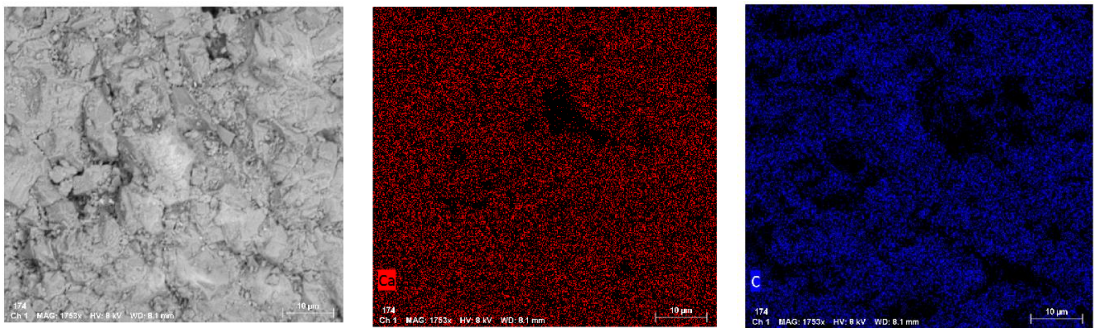

Figure 6.10. SEM Images and EDX maps of primary calcite

In figure 6.9 the secondary silica microstructure and the elemental maps for silicon are presented, which is shown to be the abundant element for the region analysed, while the Carbon is much less abundant. In comparison with figure 6.10 where the primary calcite is shown, mineral that is characterized by high

concentrations of calcium and carbon as proved by the elemental maps resulted from the EDX analysis.

Since the Atacama microbilite has mainly a carbonaceous structure, the chemical procedure used included a first step of digestion in nitric acid solution and continued only with the supernatant for Pu separation using the special resin TEVA.

Table 6.7. AMS plutonium results for Atacama microbialite (MFQB 8.2)

Sample/ Code	Sample mass [g]	^{244}Pu detected events	Total detection eff. (δ) 10^{-4}	$^{244}Pu/^{239}Pu$	$^{240}Pu/^{239}Pu$
MFQB 8.2 AC180	4480	$12\ ^{+8.34}_{-5.68}$	0.33	$2.07 \cdot 10^{-4}\ ^{+1.44\,10^{-4}}_{-0.98\,10^{-4}}$	0.113 ± 0.028

In table 6.7. the main results with respect to plutonium AMS determinations are presented. The sample mass analysed was in the order of a few kg, the total detection efficiency, that takes in account the chemical procedure and the actual AMS measurement processes, is equal to $0.33 \cdot 10^{-4}$ and it indicates a good chemical yield.

An unexpected result was the detection of the anthropogenic plutonium, by detecting ^{239}Pu and ^{240}Pu, even if Atacama Desert is the driest place on earth, it seems that plutonium from atomic bombs cannot be avoided while analysing environmental samples exposed on the Earth surface or close to it. As shown in the previous sections where the anthropogenic isotopic ratios were discussed, the ^{244}Pu to ^{239}Pu ratios result appears to indicate only the nuclear bomb test as a source for ^{244}Pu, given also its age, of about 4 Ma, well outside the CCSN time-window. Anyway, further tests are needed to investigate the source of plutonium isotopes, for example, to measure carbonates with different ages from the same area.

6.4. Laguna Negra. Sediments and Oncolite

To assess an uptake factor of plutonium in the fossilised reservoirs, contemporary stromatolites (known also as oncolites) from Argentina were sampled, one of the few places on Earth where they are still growing. These will be investigated for their plutonium concentration from global fallout resulted during the nuclear bomb tests. The terrestrial fluence is determined by investigating sediments sampled from the same areas as the stromatolites.

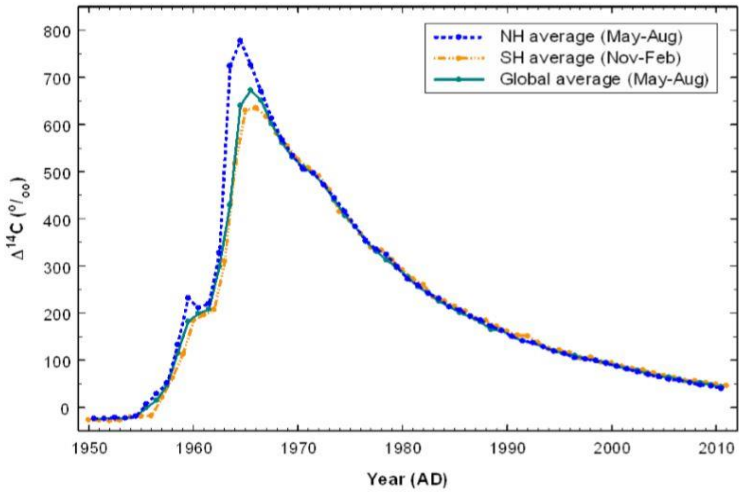

Figure 6.11. ^{14}C concentrations measured in tree rings for different years uncovering the Bomb Peak for the Southern Hemisphere (SH) and the Northern Hemisphere (NH) is visible (taken from Q. Hua et al., 2013)

In Figure 6.11. the sudden increase of ^{14}C during the nuclear atmospheric test is shown, for this reason, radiocarbon dating measurements of modern oncolites from Argentina, Laguna Negra, were performed to localize the layer with the highest ^{14}C concentration and to determine a growth rate of such structures, currently not known. The method and the results are extensively presented in Baikalov, 2019.

Briefly, the modern stromatolites from Laguna Negra in the Argentinian Andes (Figure 6.12a) yielded radiocarbon ages in the age range of 15000-30000 yr Before Present-BP (Figure 6.12b), casting doubt on the validity of the sampling procedure, because the results showed much older ages than expected.

The radiocarbon results were confirmed by independent measurements at CIRCE AMS Laboratory in Italy, the results are indicated in figure 6.12b.

Tests for possible sources of contamination in the sampling procedure were therefore performed, but no contaminants were found: the measured radiocarbon ages seemed to truly stand for the ^{14}C content of the stromatolites. The radiocarbon dating results therefore suggest that the stromatolites have not acted as closed systems to extraneous carbon since the time of their formation, or these erroneous ages might be caused by some local environmental contamination or reservoir effect.

a) 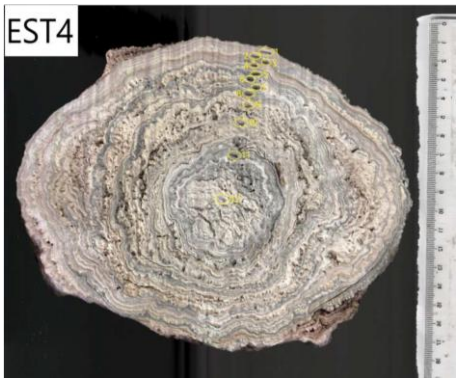

b) 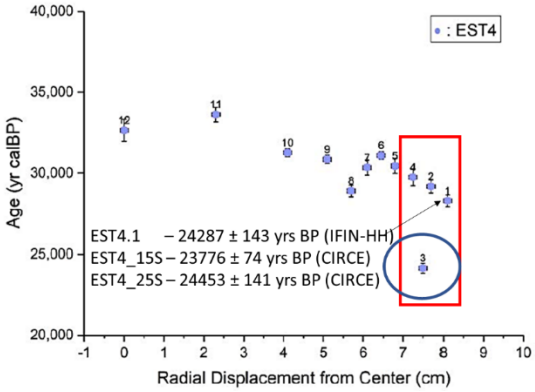

Figure 6.12. (a) Photo of Argentinian stromatolite – EST4 and the sampling points (b) Radiocarbon dating results for EST4 (taken from Baikalov, 2019)

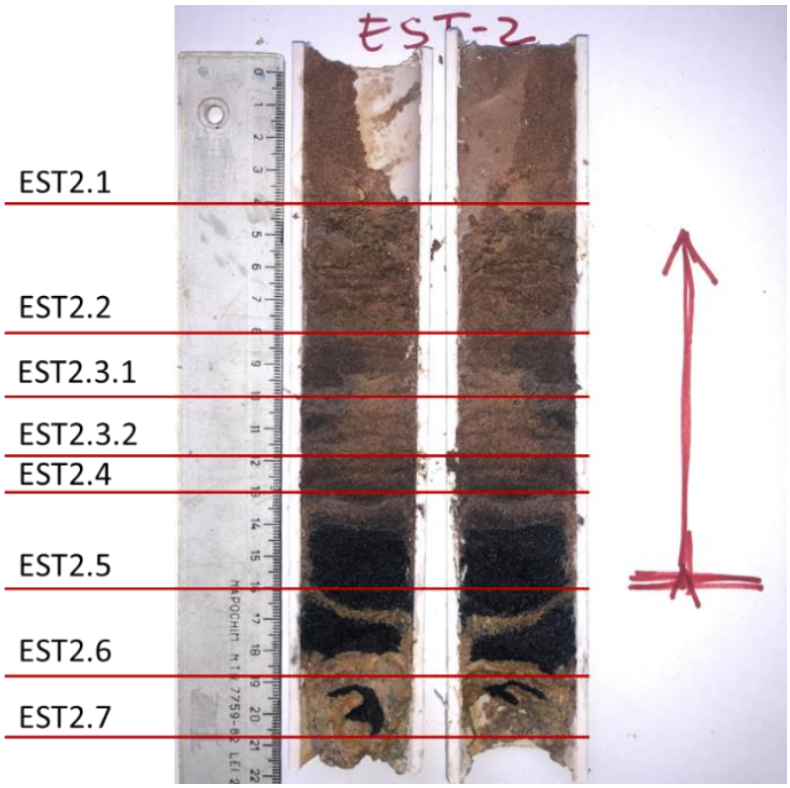

Figure 6.13. Sediment core sampled from Laguna Negra, Argentina

The mass of chemically treated sediments was of the order of a few grams, while for oncolite was a few thousand grams (figure 6.12a). Initially half of the oncolite was digested and later only one aliquot was processed for plutonium measurement. The concentration of plutonium isotope for the stromatolite seems small compared to the sediment samples, but the explanation, corroborated with the radiocarbon results, could be that this stromatolitic structure was not growing during the nuclear test and what we measured was only on its exterior. Exterior

was washed with water and leached with nitric acid, because was cut in half by an automated pressurized jet of water and sand. Anyway, by performing this experiment the chemical procedure was tested and it an overall detection efficiency of $0.51 \cdot 10^{-4}$ was obtained, a relatively encouraging one for further analysis of this type of sample.

Table 6.8. Plutonium results for Oncolite, Laguna Negra Argentina

Sample/ Code	Sample mass [g]	^{239}Pu/ g sample	$^{240}Pu/^{239}Pu$
EST 4/ AC209	600	$3.04 \cdot 10^6 \pm 0.31 \cdot 10^6$	0.038 ± 0.012

Table 6.9. Obtained ^{239,240}Pu results (atomic ratios and inventories) for Argentinian sediment core and total Pu fluence

Sample/ Code	^{240}Pu $\cdot 10^7$/g	^{239}Pu $\cdot 10^8$/g	$^{240}Pu/^{239}Pu$	^{239}Pu $\cdot 10^{11}$ at/m^2	A ($^{239+240}$Pu) Bq/m^2
EST 2.1/AC 164	0.67 ± 0.10	0.83 ± 0.16	0.081 ± 0.020	31.08 ± 6.21	3.68 ± 0.91
EST 2.2/ AC165	0.71 ± 0.08	1.65 ± 0.28	0.043 ± 0.008	82.38 ± 13.52	8.69 ± 1.79
EST 2.3.1/ AC187	1.72 ± 0.32	1.10 ± 0.24	0.077 ± 0.022	27.51 ± 6.21	3.95 ± 1.15
EST 2.3.2/ AC186	0.94 ± 0.18	1.23 ± 0.24	0.156 ± 0.046	30.62 ± 5.78	3.58 ± 0.98
EST 2.4/ AC191	0.11 ± 0.04	0.06 ± 0.02	0.174 ± 0.100	0.79 ± 0.34	0.12 ± 0.06
EST 2.5/ AC192	$< 2.21 \cdot 10^3$				
EST 2.6/ AC193	$< 1.20 \cdot 10^3$				
EST 2.7/ AC194	$< 2.26 \cdot 10^3$				
Pu fluence				$\mathbf{172.37 \pm 17.13}$	20.02 ± 2.52

Before measuring the sediment samples, the expectation was that plutonium is residing only in the first ~10 cm in depth, but later the AMS result showed us (table 6.9) that plutonium is detectable much more deeply inside the core. The choice of dividing the sediment cores was according to the change of colour and structural appearance. By taking in account the detection efficiency for each sample and the initial mass the concentration of atoms per gram of sediment was calculated. After that by using the structural/ physical characteristics of the sediment core like top area (9.61 cm^2) and density of the sediment (1.25g/cm^3, Andersen et al., 2005; Stringer et al., 2016) the fluence of ^{239}Pu atoms per m^2 and activity fluence as a sum of the activities for ^{240}Pu and ^{239}Pu is inferred.

The resulting fluence for the analysed area in Argentina is $172.37 \cdot 10^{11}$ ($\pm 9.94\%$) ^{239}Pu at/m^2, result that will be used to calculate the uptake factor after identifying a more appropriate stromatolite sample.

Our final anthropogenic plutonium inventory result is supported by the findings reported in Chamizo et al., 2011, where sediments from Chile and Argentina (studied area between 36^{o}S and 72^{o}W) were analysed also by AMS. The sediment core analysed for this work is sampled from the same geographical region, and the result obtained, 20.0 ± 2.5 Bq/m^2, for the cumulated radioactivity for ^{240}Pu and ^{239}Pu agrees within the interval found in Chamizo et al., 2011 of 38.4 and 0.7 Bq/m^2.

6.5. Turkana Basin. Stromatolite and Oncolite

Trukana stromatolite has the proper age for searching ^{244}Pu that could have been produced in CCSNe, consequently most of the experiments were dedicated to this sample type.

The reason for the low detection efficiency of the first target is mainly explained by the fact that measurement was stopped to verify the detection of 240 and 239 masses in the detector. After it was confirmed that the sample contained the two isotopes, the measurement was continued, the data used for data analysis is from the second run.

Table 6.10. Individual detailed data for Turkana stromatolite (TUR2) subsamples

Sample / Code	sample mass [g]	^{244}Pu detected events	total detection eff. (δ) 10^{-4}	^{244}Pu/^{239}Pu ($\cdot 10^{-4}$)	^{240}Pu/^{239}Pu
TUR2/ AC169	3400	$3\ ^{+5.25}_{-2.18}$	0.06	$6.75\ ^{+11.80}_{-4.91}$	0.222 ± 0.156
TUR2/ AC176	370	$2\ ^{+4.72}_{-1.64}$	0.26	$3.87\ ^{+9.14}_{-6.51}$	0.213 ± 0.068
TUR2/ AC175	370	0 (< 3.09)	0.23	<34.8	$0.174\ ^{+0.095}_{-0.071}$
TUR2/ AC174	1280	0 (< 3.09)	0.06	<160	$0.252\ ^{+0.284}_{-0.159}$
TUR2/ AC181	1880	$2^{+4.72}_{-1.64}$	0.12	$38.4\ ^{+90.7}_{-31.5}$	$0.142\ ^{+0.123}_{-0.073}$

The detection of $^{240 \text{ and } 239}$Pu isotopes during the first AMS measurement (AC169) of the Turkana Stromatolite prompted more investigations of the anthropogenic contamination by sequential leaching of the samples. Basically,

carbonate layers of the samples were digested, and the solutions resulted were used to extract plutonium. In table 6.11 the ^{239}Pu concentrations of the layers going from the outside (AC176) into the middle (AC175, AC174) and finally, the interior (AC181) of stromatolites are presented, showing a decrease of the anthropogenic isotope which indicates that the samples could be decontaminated.

Another observation that can be made, is that, while the isotopic ratio of ^{240}Pu/^{239}Pu is kept within the limits no matter the type of sample analysed (exterior or interior), the isotopic ratio of ^{244}Pu/^{239}Pu is changing, culminating with the result for the cleanest sample (AC181) that is equal to $38.4 \cdot 10^{-4}\ ^{+90.7\cdot10^{-4}}_{-31.5\cdot10^{-4}}$ and indicates an excess of ^{244}Pu compared to the global fallout that is in the order of 10^{-4}.

Table 6.11. ^{239}Pu concentrations resulted after the sequential leaching procedure

Sample/ Code	^{239}Pu ($\cdot10^{-4}$) atoms/g sample
TUR2/ AC176	79.4 ± 20.4
TUR2/ AC175	15.5 ± 8.60
TUR2/ AC174	$4.01\ ^{+2.79}_{-1.90}$
TUR2/ AC181	1.86 ± 1.36

The next round of investigations was made on a bigger sample mass aiming to improve the statistics and in addition, the Holocene stromatolite (AC260/ TUR12) was chemically pre-treated. Given its age, in the order of a few thousands of years, well outside the supernova time window of 2.6-1.6 Ma it should not have any excess of ^{244}Pu, and any plutonium detected would come from the nuclear bomb tests.

Table 6.12. Individual detailed data for the Turkana 2Ma stromatolite (TUR2) and the Holocene Oncolite (TUR12)

Sample/ Code	Sample mass [g]	^{244}Pu detected events	Total detection eff. (δ) 10^{-4}	^{244}Pu/^{239}Pu ($\cdot10^{-4}$)	^{240}Pu/^{239}Pu
TUR2/ AC259	7390	$9^{+7.77}_{-4.64}$	0.18	$1.49^{+1.28}_{-0.76}$	0.185 ± 0.062
TUR12/ AC260	5730	$7^{+6.81}_{-4.42}$	0.33	$0.83^{+0.81}_{-0.53}$	0.176 ± 0.068

The two samples have the same isotopic ratio, within the errors, for ^{240}Pu/^{239}Pu, which is expected since these two isotopes have only and the same source, the global fallout. Regarding the ^{244}Pu/^{239}Pu, it is slightly bigger for the 2Ma old stromatolite, but close enough to the ratio for the Holocene one, and

surprisingly it is within the interval obtained for the environmental samples – the certified materials presented earlier; and it is not supporting, inside the 95% confidence interval, the first result, more precisely the one obtained for sample AC181. Another information obtained from this experiment is that, even though the samples were washed with ultrapure water using ultrasound bath, the anthropogenic contamination could not be totally removed.

In parallel to the previous measurement, a blind preparation starting with the resin separation was performed, that included the stromatolite samples, reference materials (presented in previous section) and blank solution – only the spike material. The starting quantity was around 25 kg of Turkana Stromatolite that was again, leached in steps with nitric acid resulting three types of samples – Exterior, Middle and Interior. Before the resin separation each supernatant was divided in two, one to be measured at IFIN-HH and the other one to be measured at CIRCE laboratory.

Table 6.13. Plutonium results for Turkana stromatolite, measured with the 1MV HVE Accelerator at IFIN-HH and 3MV NEC Accelerator at CIRCE

Sample/ Code	Sample mass [g]	^{244}Pu detected events	Total detection eff. (δ) 10^{-4}	^{244}Pu/^{239}Pu (·10^{-4})	^{240}Pu/^{239}Pu
IFIN_INT/ AC244	5770	$1^{+4.14}_{-0.95}$	0.36	$1.22^{+5.06}_{-1.16}$	0.158 ± 0.084
CIRCE_INT/ AC236	5770	$0(< 3.09)$	0.11	< 17.87	0.272 ± 0.182
IFIN_MID/ AC241	3090	$7^{+6.81}_{-4.42}$	0.77	$1.63^{+1.59}_{-1.03}$	0.203 ± 0.094
CIRCE_MID/ AC240	3480	$5^{+6.26}_{-3.16}$	0.22	$3.43^{+4.30}_{-2.17}$	0.193 ± 0.110
IFIN_EXT/ AC246	3630	$4^{+5.76}_{-2.63}$	0.33	$0.46^{+0.67}_{-0.31}$	0.184 ± 0.088
CIRCE_EXT/ AC235	3630	$11^{+8.29}_{-5.86}$	0.12	$3.51^{+2.64}_{-1.87}$	0.203 ± 0.116

The results are summarized in table 6.13 and in figures 6.14 a and b, and all of them agree within the 95% confidence interval. But again, the ^{244}Pu/^{239}Pu ratio is not showing an excess of ^{244}Pu. In terms of detection efficiency, the values are in the same order of magnitude, a little smaller the ones obtained using the 3MV Accelerator.

During the first experiments, as stated before, only the supernatant resulted from the digestion of the carbonate was analysed, while the residue that resulted from the reaction was not analysed. Therefore, it was needed to check the plutonium content in this part of the sample.

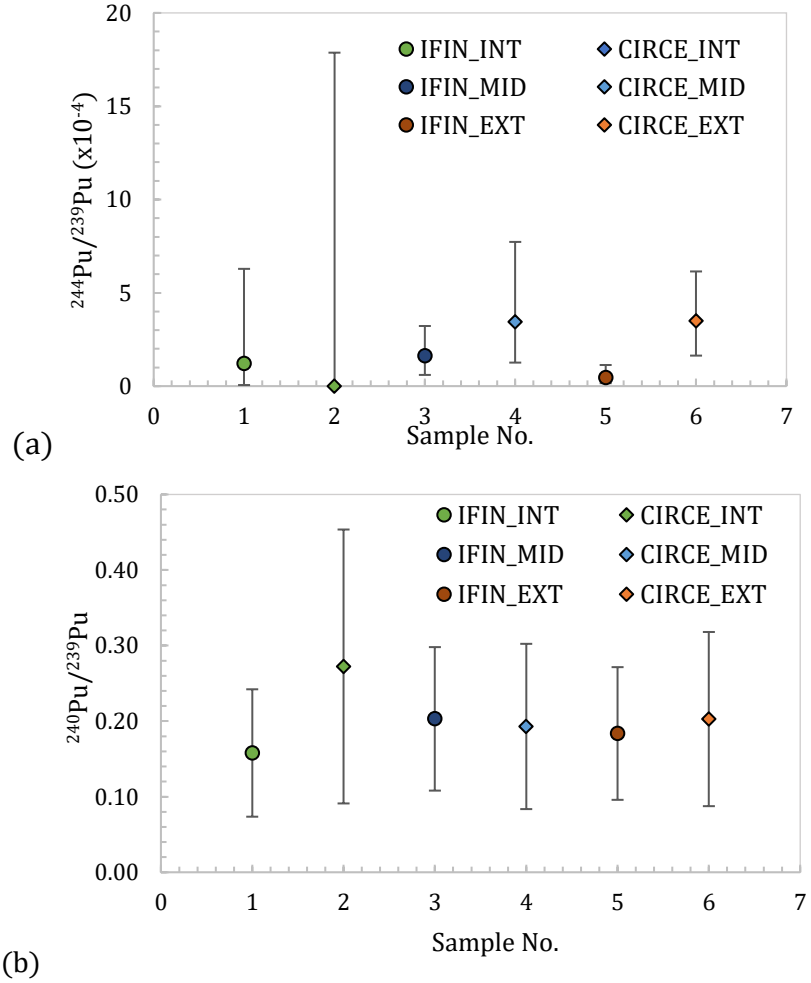

Figure 6.14. The isotopic ratios (a – $^{244}Pu/^{239}Pu$, b – $^{240}Pu/^{239}Pu$) obtained for Turkana stromatolite by measuring it in two laboratories (IFIN-HH, Romania and CIRCE, Italy)

Table 6.14. Turkana Stromatolite, residue undigested by nitric acid, detailed results for Pu AMS measurements

Sample/ Code	Sample mass [g]	^{244}Pu detected events	Total detection eff. (δ) 10^{-4}	$^{244}Pu/^{239}Pu$ ($\cdot 10^{-4}$)	$^{240}Pu/^{239}Pu$
TUR2_AqR/AC295	150	0(< 3.09)	0.11	< 9.16	0.153 ± 0.052
TUR2_AqR/AC294	940	0(< 3.09)	0.02	< 556	< 0.530
TUR12_AqR/AC296	1170	0(< 3.09)	0.09	< 3.87	0.185 ± 0.082
TUR2_NH_3_CaOx/ AC298	310	0(< 3.09)	0.19	< 149	$0.074^{+0.176}_{-0.061}$
TUR2_NaOH_1/ AC299	1220	$8^{+7.29}_{-5.06}$	0.25	$1.37^{+1.25}_{-0.87}$	0.192 ± 0.042
TUR2_NaOH_2/ AC301	2170	$19^{+10.31}_{-7.74}$	0.29	$1.01^{+0.59}_{-0.45}$	0.181 ± 0.032

The sample mass analysed for the residue samples (table 6.14) are the initial mass of stromatolites. The data for $^{244}Pu/^{239}Pu$ seems to indicate that its source is only the anthropogenic plutonium, the different chemical procedures applied give results that are in agreement one to another, as well as for the $^{240}Pu/^{239}Pu$, even if the detection efficiencies are different, the reason for this being the fact that different chemical steps were employed to obtain the hydroxides or fluoride precipitates.

6.6. Interpretation and analysis of Pu results

The plutonium AMS measurement started with a promising result that indicated an excess of ^{244}Pu relative to the anthropogenic plutonium isotopic ratios. Also, when comparing the result for the whole sample result (AC169) with the sample with partially leached surface (AC181), the isotopic ratio of $^{244}Pu/^{239}Pu$ seems to be reduced showing the reducing impact of the anthropogenic concentration. But when the sample mass was increased the atomic ratio got smaller, no matter where the measurement was performed, instead of supporting the initial findings.

During each round of experiments a blank target containing only the reference isotope, starting with TEVA separation was used. Figure 6.15 shows an example of cumulated spectrum during the sputtering of two cathodes spiked with 0.2 pg each and the parameters were set for mass 244. Therefore, any contamination contained in the spike material can be excluded, because in the spectrum only the $^{163}Dy^{2+}$ (in the green region) and 0 counts in the region of interest (ROI) marked with red are detected.

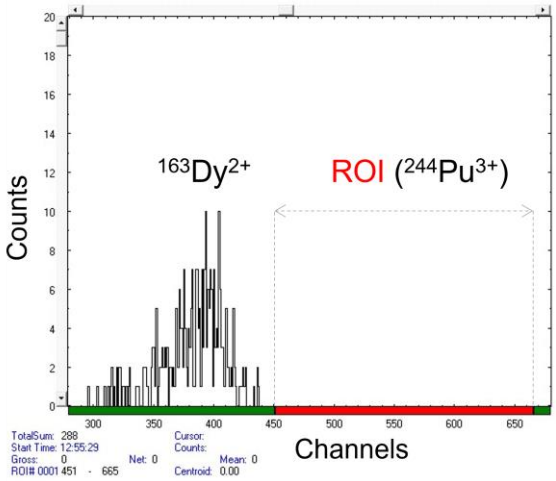

Figure 6.15. Cumulated spectrum for ^{244}Pu while measuring 2 cathodes spiked with 0.2pg of ^{242}Pu each

As done for the Atacama microbialite, the Turkana stromatolite was analysed from the microstructural and compositional point of view. In figure 6.16 the Scanning electron microscopy is revealing the microscopic open pores that contains sediment that filled the empty spaces in time. This aspect is emphasised by the EDX analysis – elemental maps that shows that the main elements in these pores are iron and silicon. It seems that the anthropogenic plutonium is also found in these pores, but at the same time, given their dimension it shows that when dealing with kg of material it is impossible to remove it completely.

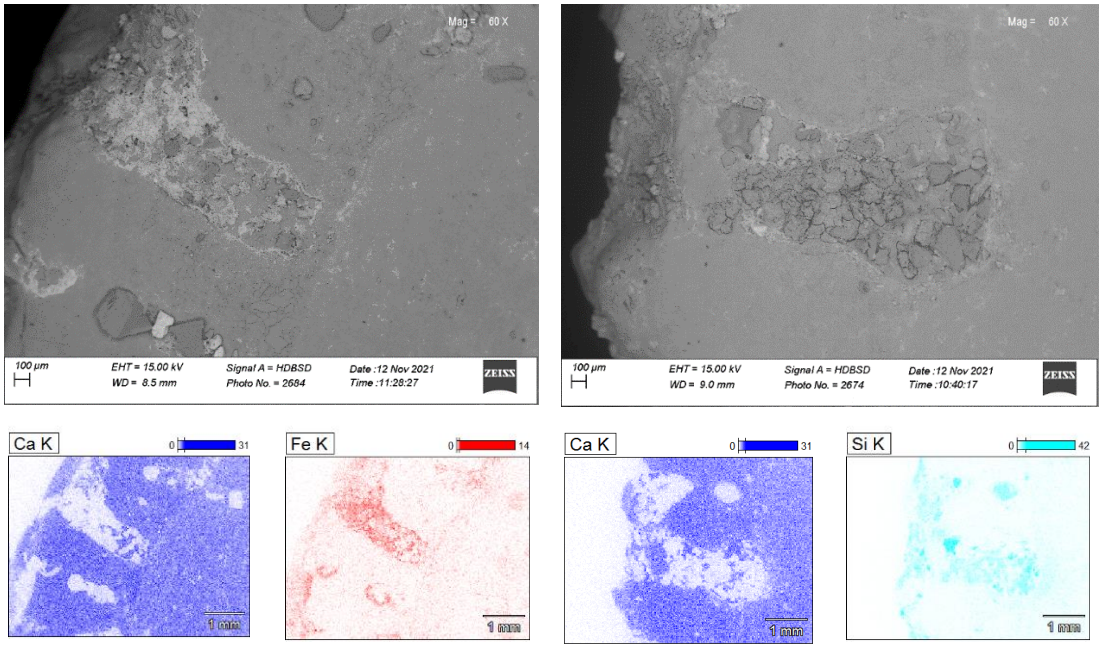

Figure 6.16. SEM images and elemental maps of Turkana Stromatolite

Consequently, an explanation for the different results obtained is that when using large quantities of sample, the concentration of anthropogenic ^{239}Pu is increased (Figure 6.17 the concentration of ^{239}Pu of the Turkana samples measured at IFIN-HH and CIRCE)) and it covers completely any excess of ^{244}Pu. Thus in order to have a definitive answer when analysing this type of sample the detection efficiency should be increased with at least one order of magnitude and keep the sample mass around 2-3 kg, quantity that can be easily manageable during extensive cleaning steps.

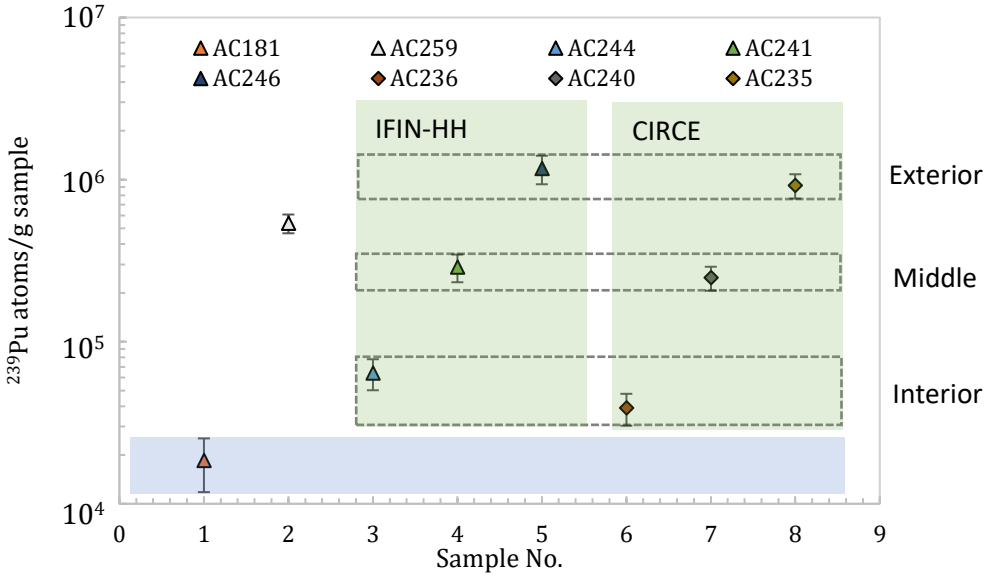

Figure 6.17. ^{239}Pu Concentration for Turkana Stromatolite (atoms/g of sample)

Since the measurement of AC181 does not seems corrupted in any way, as presented in figure 6.18 where are presented the cumulated spectrum for the blank sample run for around 3 hours before (figure 6.18a) the stromatolite sample, for which the 2 counts detected are shown in figure 6.18b, respectively.

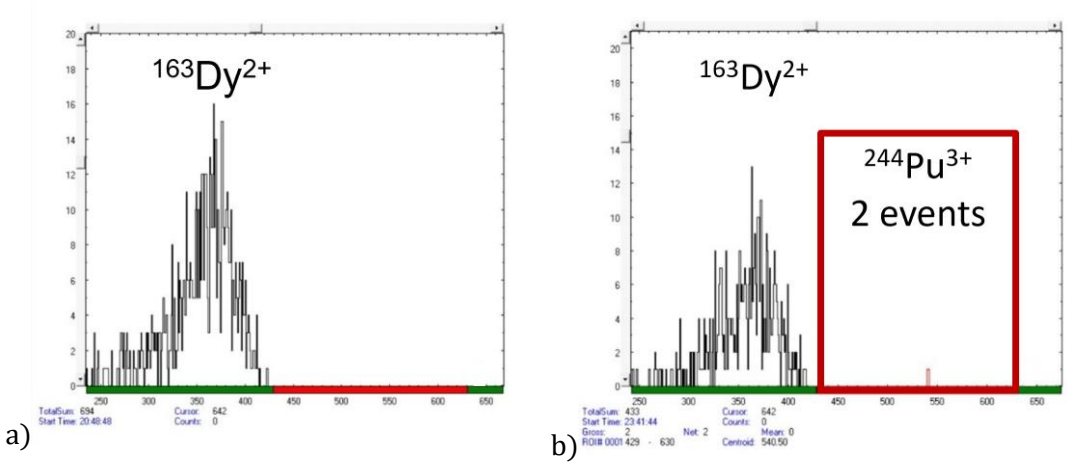

Figure 6.18. ^{244}Pu spectrum for the blank material measured before the real sample and for the Turkana Stromatolite (AC181)

The SEM imagine together with the sketched plutonium atoms presented in figure 6.19 are showing the simplified hypothesis regarding the incorporation of plutonium in the stromatolite pores and carbonate structure. So, the measured ^{244}Pu plutonium would have two sources the nuclear bomb and an extra-terrestrial injection of Earth. But the detected ^{239}Pu isotope is characteristic only to the global fallout, because given its half-life if it arrived 2Ma ago on earth it already decayed to undetectable levels. Then, in table 6.15 the results are listed by analysing the

data for the measurement for which it seems that a balance between anthropogenic contribution and the sample mass was kept therefore, it was obtained a less diluted signal for ^{244}Pu.

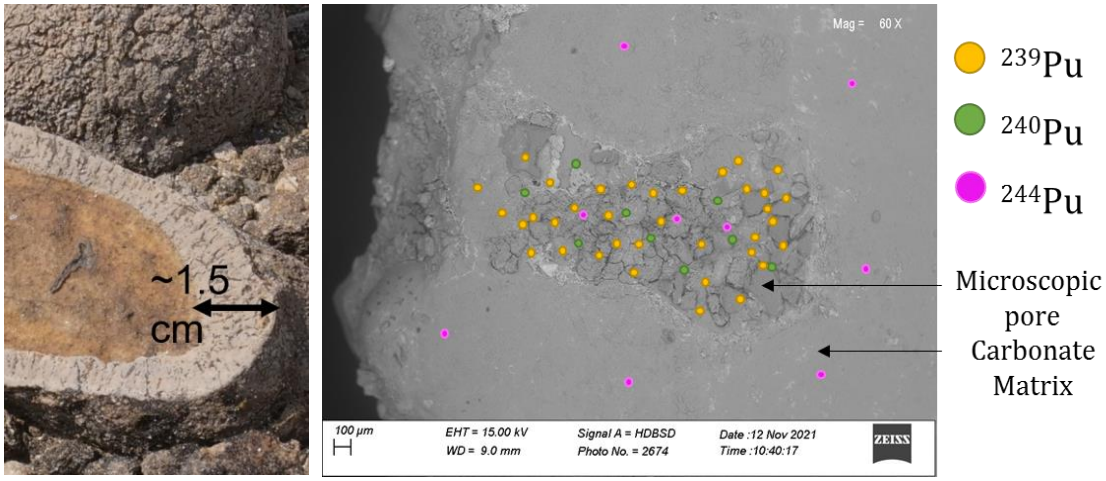

Figure 6.19. Photo and SEM imagine of Turkana stromatolite and the presumably situation of plutonium incorporation into the stromatolite pores and structure

Table 6.15. ^{244}Pu detector events and corresponding Interstellar fluence data for the Turkana stromatolite sample considering an injection of extra-terrestrial ^{244}Pu on earth

Sample Code	^{244}Pu detected events	Total ^{244}Pu in analysed mass [10^5 atoms]	Extra-terrestrial ^{244}Pu [atoms/g stromatolite]	^{244}Pu interstellar fluence [10^3 atoms/cm^2]
AC181	$2^{+4.72}_{-1.64}$	$1.31\ ^{+3.14}_{-1.13}$	$69.79\ ^{+166.80}_{-60.04}$	$5.39\ ^{+12.84}_{-4.63}$

As a reference for the anthropogenic isotopic ratio, that obtained for the Holocene stromatolite of $0.83^{+0.81}_{-0.53}(\cdot 10^{-4})$ was taken into consideration. This value was used to quantify the ^{244}Pu produced and released into the atmosphere in the 1960s and then the concentration for the ^{244}Pu extra-terrestrial (calculated as ^{244}Pu$_{excess}$/m_stromatolite) was obtained by using the analysed sample mass.

Since it is known that stromatolites can mass concentrate trace elements in their structure, to find out the concentration of plutonium in the water in which the stromatolites grew a biological uptake factor by using the concentrations for uranium and thorium measured in the stromatolite and water was obtained. The average value that is expressing the concentration in the water relative to the concentration measured in the biological reservoir is $6.17 \cdot 10^{-3}$.

Lake Turkana presents a ratio for Surface (6405 km^2) to Volume (203.6 km^3) of $32\ km^{-1} = 3.2 \cdot 10^{-4}\ cm^{-1}$, the terrestrial flux of ^{244}Pu can be calculated

and finally the fluence at Earth orbit ($\Phi_{ISM^{244}Pu}$, *Eq* 6.3.) is inferred by assuming a unidirectional and homogeneous interstellar fluence relative to the Solar System the value obtained is scaled by a factor of 4 to account for the four times larger Earth surface compared to its cross section (Wallner et al., 2015; Wallner et al., 2021).

$$\Phi_{ISM^{244}Pu} = \frac{\frac{^{244}Pu_{excess}}{m\_stromatolite} \cdot Av\left(\frac{water_{Ac}}{stromatolite_{Ac}}\right)}{A/V} \cdot 4 \qquad \text{Eq 6.3.}$$

If we consider only the sample mentioned before, the data obtained show an influx of interstellar material by the detection of an excess of ^{244}Pu and the result seems to agree, inside a large interval, with other results reported by Wallner and his collaborators (figure 6.19). During their work they succeeded to greatly improve the statistic when measuring ^{244}Pu, but their time resolution is yet not satisfactory, because the sedimentation rate for oceanic sediments or ferromanganese crust is extremely small.

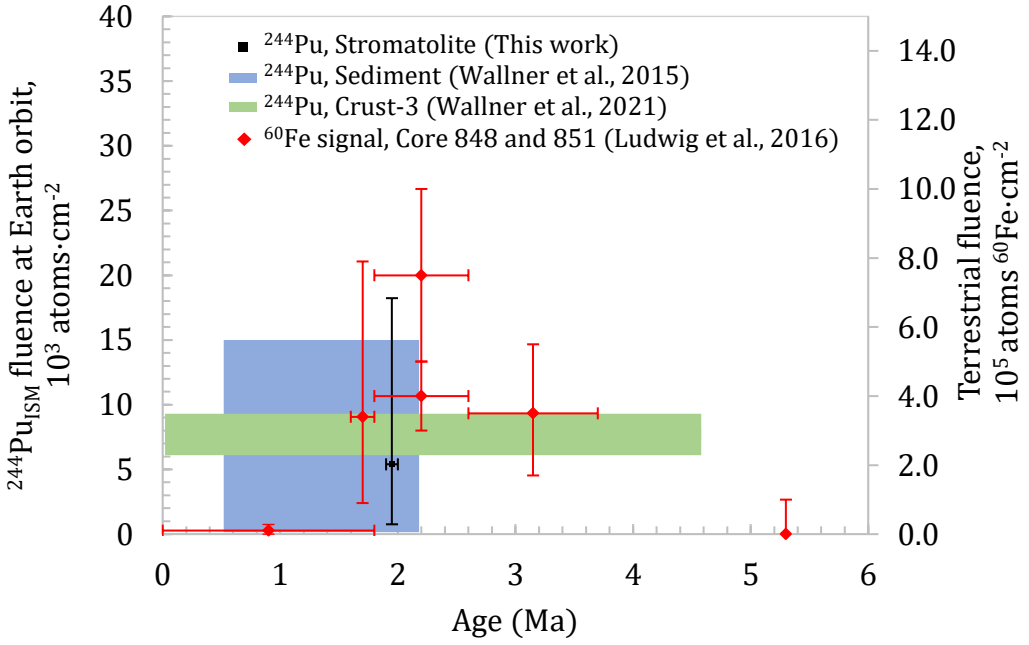

Figure 6.20. Comparison of the measured ^{244}Pu flux at earth orbit using stromatolite samples from Turkana Basin with results obtained using crust and sediment samples

In our case, we can deduce that, by detecting what seems to be an extra-terrestrial excess of the long-lived isotope of plutonium on earth by analysing stromatolites from Turkana Basin, Kenya that grew within a very well time-constrained interval coincident in time with the ^{60}Fe signal (marked with red in Fig. 6.20), that they could have the same origin, core-collapse supernova, the same conclusion was obtained as a result of the work performed in Wallner et al. 2021.

7. Conclusions

In the context of this project, AMS measurements of plutonium isotopes were performed using different type of samples collected from several places around the world.

The radioisotope ^{244}Pu has been chosen for searching evidence to the r-process occurring in CCSNe, as it is an r-process only isotope and has a very long half-live, providing the same conditions as for ^{60}Fe, that has been already found on Earth between 2.6 - 1.6Ma. Unfortunately, ^{244}Pu is less abundantly produced than ^{60}Fe, therefore, reservoirs with a natural mechanism of mass concentration enhancement of trace elements had to be found.

Such reservoir are the fossilized stromatolites from the Turkana Basin (Kenya) and Atacama Desert, Chile. These were investigated by mass spectrometry determinations of the concentrations of lanthanides and natural actinides. The results showed a mass-concentration enhancement of these elements in the stromatolites compared to the water samples from the same geological areas. The mass concentration enhancement for the Atacama Desert sample for REEs is ranging from 10^4 to 10^7 and for the Kenya Basin sample is ranging from 10^3 to 10^4. For thorium and uranium, the mass concentrations are ranging from 10^3 to 10^4 for the Atacama microbialites and from 10^2 to 10^3 for the Turkana stromatolites.

Also, to improve the chances to detect this extremely rare isotope ^{244}Pu developed complex and challenging chemical procedures were developed to extract and concentrate plutonium from a few kg of carbonaceous rock for each sample that was analysed using accelerator mass spectrometry to mg range of AMS material.

Another type of samples (contemporary stromatolites) has been obtained from the Argentine Andes. These samples were used to determine the biological uptake factor by measuring the uptaken atmospheric Pu isotopes released during the period of atmospheric nuclear weapons testing and comparing it to the global fallout.

The plutonium AMS measurements were performed using two AMS systems, 1MV Accelerator from HVE of IFIN-HH, Magurele, Romania and 3MV Accelerator from NEC of CIRCE, Caserta, Italy. We proved zero background when measuring mass 244 by Accelerator Mass Spectrometry at low and high energies and a total measurement efficiency by using each system in the order of 10^{-4}.

The modern stromatolites from Laguna Negra in the Argentinian Andes yielded radiocarbon ages in the age range of 15,000 - 30,000yr Before Present

(BP), casting doubt in the validity of the sampling procedure. Tests for possible sources of contamination in the sampling procedure were therefore performed, but no contaminants were found: the measured radiocarbon ages seemed to truly represent the ^{14}C content of the stromatolites, therefore other method for dating needs to be investigated and applied for these samples. While a plutonium AMS measurement did not seem successful for the stromatolite, by measuring a sediment core from the same area a fluence for anthropogenic ^{239}Pu of 172.37 ± 17.13 (10^7 atoms/cm^2) could be determined successfully. It can be used in future investigations to obtain the biologically uptake factor for the stromatolites.

The first AMS investigations, when Pu was extracted from 2-3 kg of Turkana stromatolite, show an excess of ^{244}Pu relative to the, only anthropogenic, ^{239}Pu isotope. These results prompted further studies by increasing the mass chemically treated, but even if cleaning was attempted all the samples showed high concentrations of ^{239}Pu which seems to dilute any extra-terrestrial ^{244}Pu that could have been present in samples.

To obtain an astrophysical quantity for the excess seen in the first investigation, a Holocene stromatolite was processed, and Pu isotopes were analysed to subtract the anthropogenic contribution. These results were used to obtain a ^{244}Pu interstellar fluence at Earth orbit of $5.39\ ^{+12.84}_{-4.63} \cdot 10^3$ atoms/cm^2 for the sample measured with good detection efficiency. This result agrees with earlier ^{244}Pu searches (Wallner et al., 2015; Wallner et al., 2021) that targeted and showed that Core-collapse supernovae could be a source of r-process elements.

Mainly due to the scarcity of the ^{244}Pu isotope sought and to the technical limitations, the results have high uncertainties, which can be reduced only by improving the statistics. Among the solutions I foresee is to change the final chemical form of the AMS target material, instead of oxides, plutonium could be extracted as fluorides, this chemical compound can improve the ionisation process (Zhao and Francisco, 2022). Another one is to upgrade the ion source to the latest version that HVE company offers. While the first suggestion is only time consuming because everything must be tested all over again the second one is financially expensive (Klein and Dirk, 2016).

A. Appendix. Main gamma rays of the natural long-lived radioisotopes

In the following tables are presented the main gamma rays of the natural long-lived radioisotopes together with the half-lives of the isotopes and type of decay (alpha or beta).

Table A.1. Main gamma rays of daughters of U-238

	Eg (keV)	Iγ (%)	Decay mode
^{234}Th (24.10 d)	63.29	4.80	β^-
	92.38	2.81	β^-
	92.80	2.77	β^-
	112.81	0.28	β^-
^{234}mPa (1.17 m)	258.23	0.07	β^-
	742.81	0.08	β^-
	766.38	0.29	β^-
	1001.03	0.84	β^-
^{226}Ra (1600 y)	186.21	3.59	α
	262.27	0.01	α
	414.60	0.0003	α
	600.66	0.0005	α
^{214}Pb (26.8 m)	53.23	1.20	β^-
	242.00	7.43	β^-
	295.22	19.30	β^-
	351.93	37.60	β^-
	785.96	1.07	β^-
	839.04	0.587	β^-
^{214}Bi (19.9 m)	609.31	46.10	β^-
	768.36	4.94	β^-
	806.17	1.22	β^-
	934.06	3.03	β^-
	1120.29	15.10	β^-
	1155.19	1.63	β^-
	1238.11	5.79	β^-
	1377.67	4.00	β^-
	1407.98	2.15	β^-
	1729.59	2.92	β^-
	1764.49	15.40	β^-

	1847.42	2.11	β^-
	2204.21	5.08	β^-
^{210}Pb (22.3 y)	46.54	4.25	β^-

Table A.2. Main gamma rays of daughters of U-235

	Eg (keV)	Iγ (%)	Decay mode
^{235}U (7.04×10^8 y)	109.16	1.54	α
	143.76	10.96	α
	185.71	57.20	α
	205.31	5.01	α
^{231}Th (25.52 h)	25.65	14.50	β-
	81.23	0.89	β-
	84.22	6.60	β-
	89.94	0.94	β-
^{231}Pa (32760 y)	27.36	10.30	α
	300.07	2.46	α
	330.06	1.40	α
	283.69	1.7	α
	302.65	2.20	α

Table A.3. Main gamma rays of daughters of Th-232

	Eg (keV)	Iγ (%)	Decay mode
^{228}Ac (6.15 h)	129.06	2.24	β-
	209.25	3.89	β-
	270.25	3.46	β-
	328.00	2.95	β-
	338.32	11.27	β-
	463.00	4.40	β-
	794.95	4.25	β-
	911.20	25.80	β-
	964.77	4.99	β-
	968.971	15.80	β-
	1588.19	3.22	β-
^{212}Pb (10.64 h)	115.18	0.59	β-
	238.63	43.30	β-

	300.09	3.28	β-
	415.2	0.14	β-
^{212}Bi (60.55 m)	39.86	1.09	β-
	727.33	6.58	β-
	785.37	1.10	β-
	1078.62	0.564	β-
	1620.50	1.49	β-

Table A.4. Main gamma ray of K-40

^{40}K (1.277×10^9 y)		
Eg (keV)	Iγ (%)	Decay mode
482.49	10.72	β^+
1311.07	89.28	β-

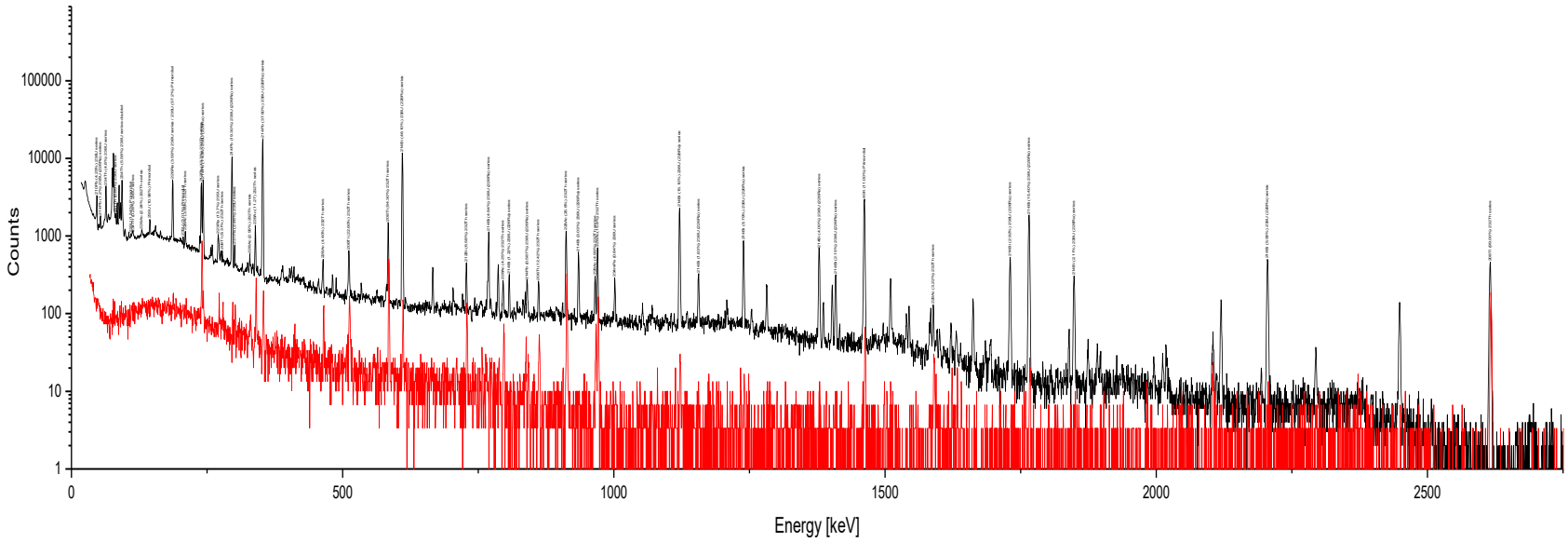

Figure A.1. Sample spectrum (black line) and background spectrum (red line), each gamma line is identified, and they are listed in the tables

Index

Abbreviations employed in this work:

AMS – Accelerator Mass Spectrometry
AS – Alpha Spectrometry
CCSN – Core-Collapse supernova
EDX – Energy Dispersive X-Ray Analysis
ESA – Electrostatic Analyzer
ESS – Early Solar System
GIC – Gas Ionization Chamber
IAEA – International Atomic Energy Agency
ICP-MS – Inductively Coupled Plasma Mass Spectrometry
ISD – Interstellar Dust
ISM – Interstellar Medium
REEs – Rare Earth Elements or Lanthanides
r-process – Rapid neutron capture process
SEM – Scanning Electron Microscopy
SN – Supernova
s-process – Slow neutron capture process

List of Figures

List of Tables

Bibliography

Abbott B. P. et al. (LIGO Scientific Collaboration and Virgo Collaboration), 2017, GW170817: Observation of Gravitational Waves from a Binary Neutron Star Inspiral, Physical Review Letters, 119, https://doi.org/10.1103/PhysRevLett.119.161101

Abell P. I., Awramik S. M., Osborne R. H., Tomellini S., Abell P. I, 1982, Plio-Pleistocene lacustrine stromatolites from Lake Turkana, Kenya: morphology, stratigraphy and stable isotopes. Sedimentary Geology, 32, Pages 1-26, https://doi.org/10.1016/0037-0738(82)90011-2

Andersen, T. J., Lund-Hansen, L. C., Pejrup, M., Jensen, K. T., and Mouritsen, K. N., 2005, Biologically induced differences in erodibility and aggregation of subtidal and intertidal sediments: a possible cause for seasonal changes in sediment deposition, J. Mar. Syst., 55, https://doi.org/10.1016/j.jmarsys.2004.09.004

Anderson C. R., Pedersen, K., 2003, In situ growth of Gallionella biofilms and partitioning of lanthanides and actinides between biological material and ferric oxyhydroxides, Geobiology, 1, Pages 169-178 https://doi.org/10.1046/j.1472-4669.2003.00013.x

Argast D., Samland M., Thielemann F.-K., Qian Y.-Z., 2004, Astronomy & Astrophysics, 416, Stellar structure and evolution, 416, Pages 997 – 1011, https://doi.org/10.1051/0004-6361:20034265

Arp G., Reimer, A. & Reitner, J., 2003, Microbialite formation in seawater of increased alkalinity, Satonda Crater Lake, Indonesia, Journal of sedimentary research, 73, https://doi.org/10.1306/071002730105

Baikalov, A, 2019, Radiocarbon Dating Analysis of Andean and Kenyan Stromatolites, B.Sc. Thesis. Technical University of Munchen.

Beasley T.M., Kelley J.M. , Orlandini K.A., Bond L.A., Aarkrog A. , Trapeznikov A.P., Pozolotina V.N., 1998, Isotopic Pu, U, and Np signatures in soils from Semipalatinsk-21, Kazakh Republic and the Southern Urals, Russia, Journal of Environmental Radioactivity, 39, Pages 215-230, https://doi.org/10.1016/S0265-931X(97)00050-7

Binns W. R., Israel M. H., Christiana E. R., Cummingsg C., DE Nolfo A., Lave K.A., Lesker R.A., Mewaldt R.A., Stonet A., Von Rosenvingeand T., Wiedenbeck E., 2016, Observation of the 60Fe

nucleosynthesis-clock isotope in galactic cosmic rays, SCIENCE, 352, Pages 677-680, https://doi.org/10.1126/science.aad6004

Bowen V.T., Noshkin V.E., Livingston H.D., Volchok H.L., 1980, Fallout radionuclides in the Pacific Ocean: Vertical and horizontal distribution, largely from geosecs stations, Earth and Planetary Science Letters, 49, Pages 411-434, https://doi.org/10.1016/0012-821X(80)90083-7

Bromley S. T., Goumans T. P. M., Herbst E., Jones A. P, Slater B., 2014, Challenges in modelling the reaction chemistry of interstellar dust, Physical Chemistry Chemical Physics, 16, https://doi.org/10.1039/C4CP00774C

Burbidge E. M., Burbidge G. R., FowlerW. A. & Hoyle F., 1957, Synthesis of the elements in stars, Reviews of Modern Physics, 29, Pages 547–650 (1957).

Burrows A., 1990, Neutrinos from Supernova Explosions, Annual Review of Nuclear and Particle Science, 40, Pages 181-212, https://doi.org/10.1146/annurev.ns.40.120190.001145

Cameron A. G. W., 1957, On the origin of the heavy elements, The Astronomical Journal, 62, 9–10.

Cameron A. G. W., 1982, The heavy element yields of neutron capture nucleosynthesis. Astrophys Space Sci, 82, https://doi.org/10.1007/BF00651468

Chamizo E., 2009, Medida de isótopos de plutonio, 239Pu y 240Pu, mediante espectrometría de masas con aceleradores de baja energía, Universidad de Sevilla

Chamizo E., Enamorado S. M., García-León M., Suter M., Wacker L.,2008, Plutonium measurements on the 1MV AMS system at the Centro Nacional de Aceleradores (CNA), Nuclear Instruments and Methods in Physics Research Section B, 266, https://doi.org/10.1016/j.nimb.2008.08.001

Chamizo E., García-León M., Peruchena J.I., Cereceda F., Vidal V., Pinilla E., Miró C., 2011, Presence of plutonium isotopes, 239Pu and 240Pu, in soils from Chile, Nuclear Instruments and Methods in Physics Research Section B, 269, https://doi.org/10.1016/j.nimb.2011.04.021

Chamizo E., Jiménez-Ramos M.C., Enamorado S.M., García-León M., García-Tenorio R., Mas J.L., Masqué P., Merino J., Sanchez-Cabeza J.A., 2010, Characterisation of the plutonium isotopic composition of a sediment core from Palomares, Spain, by low-energy AMS and alpha-

spectrometry, Nuclear Instruments and Methods in Physics Research Section B, 268, Pages 1273-1276, https://doi.org/10.1016/j.nimb.2009.10.151

Chamizo E., López-Lora M., Villa M., Casacuberta N., López-Gutiérrez J. M., Khanh Pham M., Analysis of 236U and plutonium isotopes, 239,240Pu, on the 1 MV AMS system at the Centro Nacional de Aceleradores, as a potential tool in oceanography, 2015, Nuclear Instruments and Methods in Physics Research Section B, 361, http://dx.doi.org/10.1016/j.nimb.2015.02.066

Cowperthwaite P.S. et al., 2017, The Electromagnetic Counterpart of the Binary Neutron Star Merger LIGO/Virgo GW170817. II. UV, Optical, and Near-infrared Light Curves and Comparison to Kilonova Models, The Astrophysical Journal, 848, https://doi.org/10.3847/2041-8213/aa8fc7

De Cesare M., Guan Y., Quinto F., Sabbarese C., De Cesare N., D'Onofrio A., Terrasi F., 2010, Optimization of 236U AMS at CIRCE. Radiocarbon, 52, Pages 286-294, https://doi.org/10.1017/S003382220004532X

De Cesare M., Fifield L.K., Sabbarese C., Tims S.G., De Cesare N., D'Onofrio A., D'Arco A., Esposito A.M., Petraglia A., Roca V., Terrasi F., 2013, Actinides AMS at CIRCE and 236U and Pu measurements of structural and environmental samples from in and around a mothballed nuclear power plant, Nuclear Instruments, and Methods in Physics Research Section B, 294, Pages 152-159, https://doi.org/10.1016/j.nimb.2012.05.020

De Cesare M., De Cesare N., D'Onofrio A., Fifield L.K., Gialanella L., Terrasi F., 2015, Uranium beam characterization at CIRCE for background and contamination determinations, Applied Radiation and Isotopes, 103, Pages 166–172, https://doi.org/10.13140/RG.2.1.4938.2560

Dittmann B.A., Dunai T.J., Dewald A., Heinze S., Feuerstein C., Strub E., Fifield L.K., Froehlich M.B., Tims S.G., Wallner A., Christl M., 2015, Nuclear Instruments and Methods in Physics Research Section B, 361, https://doi.org/10.1016/j.nimb.2015.04.030

Dittmann B.A., Buompane R., Chamizo E., Christl M., Dewald A., Dunai T., Feuerstein C., Fifield K., Fröhlich M., Heinze S., Marzaioli F., Münker C., Petraglia A., Sirignano C., Strub E., Synal H.A., Terrasi F., Tims S., Wallner A., 2019, ColPuS, a new multi-isotope plutonium standard for Accelerator Mass Spectrometry, Nuclear Instruments and Methods in Physics Research B, 438, https://doi.org/10.1016/j.nimb.2018.04.032

Donnelly J., Thompson A., O'Sullivan D., Daly J., Drury L., Domingo V., Wenzel K.-P., 2012, Actinide and ultra-heavy abundances in the local galactic cosmic rays: an analysis of the

results from the LDEF ultra-heavy cosmic-ray experiment, The Astronomical Journal, 747, https://doi.org/10.1088/0004-637X/747/1/40

Dupraz C. and R. Pamela Reid and Olivier Braissant and Alan W. Decho and R. Sean Norman and Pieter T. Visscher, 2009, Processes of carbonate precipitation in modern microbial mats, Earth-Science Reviews, 96, https://doi.org/10.1016/j.earscirev.2008.10.005

Dupraz C. and Visscher C. T., 2005, Microbial lithification in marine stromatolites and hypersaline mats, Trends in Microbiology, 13, https://doi.org/10.1016/j.tim.2005.07.008

Dupraz, C., Visscher, P. T., Baumgartner, L. K., & Reid, R. P, 2004, Microbe–mineral interactions: early carbonate precipitation in a hypersaline lake (Eleuthera Island, Bahamas). Sedimentology, 51, https://doi.org/10.1111/j.1365-3091.2004.00649.x

Ellis J., Fields B. D., Schramm D. N., 1996, Geological Isotope Anomalies as Signatures of Nearby Supernovae, Astrophysical Journal, 470, https://doi.org/10.1086/177945

Enachescu M., 2006, Aplicații ale spectrometriei de masă cu ioni accelerați, Doctoral Dissertation, Polytechnic University of Bucharest

Enachescu M., Stan-Sion C., Petre A. R., Postolache C., Fugaru V., 2018, 3H and 14C measurements of the irradiated graphite from the decommissioned VVR-S reactor in NIPNE Bucharest, J. Anal. At. Spectrom., 33, Pages 431-436, https://doi.org/10.1039/C7JA00397H

Enachescu M., Stan-Sion C., Petre A.R., 2019, The Bucharest 1 MV HVEE Accelerator Mass Spectrometer extended for measurements of hydrogen isotopes, Nuclear Instruments and Methods in Physics Research Section B, 461, Pages 149-153, https://doi.org/10.1016/j.nimb.2019.09.033

Evans A., 1994, The dusty universe, Ellis Horwood series in science and technology, John Wiley

Evenstar L. A., Hartley A. J., Archer S. G., Neilson J. E., 2015, Climatic and halokinetic controls on alluvial—lacustrine sedimentation during compressional deformation, Andean forearc, northern Chile, Basin Res., 28, Pages 634-657, https://doi.org/10.1111/bre.12124

Fahey A. J., Goswami J. N., McKeegan K. D., Zinner E., 1987, Aluminum-26, plutonium-244, titanium-50, rare earth elements, and trace element abundances in hibonite grains from CM and CV meteorites. Geochim. Cosmochim. Acta, 51, Pages 329–350, https://doi.org/10.1016/0016-7037(87)90245-6

Farías, M. E., Rascovan, N., Toneatti, D. M., Albarracín, V. H., Flores, M. R., Poiré, D. G., ... & Polerecky, L., 2013, The discovery of stromatolites developing at 3570 m above sea level in a high-altitude volcanic lake Socompa, Argentinean Andes. *PloS one, 8*, https://doi.org/10.1371/journal.pone.0053497

Feibel G.S., Brown F.H., McDougall I., 1989, Stratigraphic Context of Fossil Hominids from the Omo Group Deposits: Northern Turkana Basin, Kenya and Ethiopia, American Journal of Physical Anthropology, 78, https://doi.org/10.1002/ajpa.1330780412

Feldman G. J., Cousins R. D., 1998, Unified approach to the classical statistical analysis of small signals, Phys. Rev. D, 57, https://doi.org/10.1103/PhysRevD.57.3873

Feldmann, M., & McKenzie, J. A., 1997, Messinian stromatolite-thrombolite associations, Santa Pola, SE Spain: an analogue for the Palaeozoic? Sedimentology, 44, https://doi.org/10.1046/j.1365-3091.1997.d01-53.x

Fimiani L., Cook D. L., Faestermann T., Gómez-Guzmán J. M., Hain K., Herzog G., Knie K., Korschinek, Ludwig P., Park J., Reedy R. C., Rugel G., 2016, Interstellar ^{60}Fe on the Surface of the Moon, PHYSICAL REVIEW LETTERS, 116, https://doi.org/10.1103/PhysRevLett.116.151104

Flynn G.J., 1997, Collecting interstellar dust grains, Nature, 387, Pages 323-325, https://doi.org/10.1038/387248a0

Fuller G. M., Kusenko A., Takhistov V., 2017, Primordial Black Holes and r-Process Nucleosynthesis, Physical Review Letters, 119, https://doi.org/10.1103/PhysRevLett.119.061101

Goriely, S., Janka H. Th., 2016, Solar r-process-constrained actinide production in neutrino-driven winds of supernovae, Monthly Notices of the Royal Astronomical Society, 459, Pages 4174–4182, https://doi.org/10.1093/mnras/stw946

Grotzinger, J. P., and Rothman, D. R., 1996, An abiotic model for stromatolite morphogenesis, Nature, 383, https://doi.org/10.1038/383423a0

Grun E., Gustafson B., Mann I., Baguhl M., Morfill G.E., Staubach P., Taylor A., Zook H.A., 1994, Interstellar dust in the heliosphere, Astronomy and Astrophysics, 286, Pages 915-924,

Hardy E.P., Krey P.W., Volchok H.L., 1973, Global inventory and distribution of fallout plutonium, Nature, 241, Pages 444-445, https://doi.org/10.1038/241444a0

Hargrave J.E., Hicks M.K., Scholz C.A., 2014, Lacustrine carbonates from Lake Turkana, Kenya: A depositional model of carbonates in an extensional basin, Journal of Sedimentary Research 84, https://doi.org/10.2110/jsr.2014.22

Harley J.H., 1980, Plutonium in the environment-a review, Journal of Radiation Research, 21, Pages 83-104, https://doi.org/10.1269/jrr.21.83

HICKS H.G., BARR D.W., 1984, Nevada Test Site fallout atom ratios: 240Pu/239Pu and 241Pu/239Pu, UCRL-53499/1 (Lawrence Livermore National Laboratory).

Hofmann H. J., Grey K., Hickman A. H., Thorpe R. I., 1999, Origin of 3.45 Ga coniform stromatolites in Warrawoona Group, Western Australia, GSA Bulletin, 111(8), Pages 1256–1262, https://doi.org/10.1130/0016-7606(1999)111<1256:OOGCSI>2.3.CO;2

Hotchkis M.A.C., Child D.P., Froehlich M.B., Wallner A., Wilcken K., Williams M., 2019, Actinides AMS on the VEGA accelerator, Nuclear Instruments and Methods in Physics Research Section B 438, https://doi.org/10.1016/j.nimb.2018.07.029

Hotokezaka K., Piran T., Paul M., 2015, Short-lived 244Pu points to compact binary mergers as sites for heavy r-process nucleosynthesis. Nature Physics, 11, Pages 1042–1044, https://doi.org/10.1038/nphys3574

Hua, Q., Barbetti, M., & Rakowski, A. Z., 2013, Atmospheric radiocarbon for the period 1950–2010, Radiocarbon 55, https://doi.org/10.2458/azu_js_rc.v55i2.16177

Hutcheon I. D., Price P. B., 1972, Plutonium-244 fission tracks. Evidence in a lunar rock 3.95 billion years old. Science 176, Pages 909–911, https://doi.org/10.1126/science.176.4037.909

Iliadis, C., 2007, 2007, Nuclear physics of stars, https://doi.org/10.1002/9783527618750.ch4

Janka H. T., 2012, Explosion Mechanisms of Core-Collapse Supernovae, Annual Review of Nuclear and Particle Science, 62, Pages 407-451, https://doi.org/10.1146/annurev-nucl-102711-094901

Johannesson, K. H. Telfeyan K., Chevis D. A., Rosenheim B. E., Leybourne M. I., 2013, Rare Earth Elements in Stromatolites—1. Evidence that Modern Terrestrial Stromatolites Fractionate Rare Earth Elements During Incorporation from Ambient Waters, volution of Archean Crust and Early Life, Pages 385–411, https://doi.org/10.1007/978-94-007-7615-9_14

Joordens J. C., Dupont-Nivet G., Feibel C. S., Spoor F., Sier M. J., van der Lubbe J. H.J.L., Nielsen T. K., Knul M. V., Davies G. R., Vonhof H. B., 2013, Improved age control on early Homo fossils from the upper Burgi Member at Koobi Fora, Kenya, Journal of human evolution, 65, Pages 731-745, https://doi.org/10.1016/j.jhevol.2013.09.002

Kelley J.M., Bond L.A., Beasley T.M., 1999, Global distribution of Pu isotopes and 237Np, Science of the Total Environments 237/238, https://doi.org/10.1016/s0048-9697(99)00160-6

Klein M., Dirk M., Technical improvements and performance of the HVE AMS sputter ion source SO-110, Nuclear Instruments and Methods in Physics Research Section B, 406, https://doi.org/10.1016/j.nimb.2016.10.032

Klein, M.G., Mous, D.J.W., & Gottdang, A., 2006, A compact 1 MV multi-element AMS system. Nuclear Instruments and Methods in Physics Research Section B, 249, http://dx.doi.org/10.1016/j.nimb.2006.03.135

Knie K., Korschinek G., Faestermann T., Wallner C., Scholten J., Hillebrandt W., 1999, Indication for supernova produced 60Fe activity on Earth, Physical Review Letters, 83, https://doi.org/10.1103/PhysRevLett.83.18

Kobayashi C., Karakas A. I., Lugaro M., 2020, The Origin of Elements from Carbon to Uranium, The Astrophysical Journal, 900, https://doi.org/10.3847/1538-4357/abae65

Koll D., Korschinek G., Faestermann T., Gómez-Guzmán J. M., Kipfstuhl S., Merchel S., Welch J. M., 2019, Interstellar ^{60}Fe in Antarctica, Physical Review Letters, 123, https://doi.org/10.1103/PhysRevLett.123.072701

Korschinek G., Faestermann T., Knie K., Schmidt C., 1996, ^{60}Fe, A promising AMS isotope for many applications, Abstracts of the 7th International AMS Conference, Radiocarbon, 38, https://doi.org/10.1017/S0033822200061579

Lachner J., Christl M., Bisinger T., Michel R., Synal H.-A., 2010, Isotopic signature of plutonium at Bikini atoll, Applied Radiation and Isotopes, 68, Pages 979-983, https://doi.org/10.1016/j.apradiso.2010.01.043

LaMont S.P., Glover S.E., Filby R.H., 1998, Determination of plutonium-240/239 ratios in low activity samples using high resolution alpha-spectrometry, Journal of Radioanalytical and Nuclear Chemistry 234, https://doi.org/10.1007/bf02389771

Linde T. J., Gombosi T. I., 2000, Interstellar dust filtration at the heliospheric interface, Journal of Geophysical Research: Space Physics, 105, Pages 10411-10417, https://doi.org/10.1029/1999JA900149

Livingston H.D., Anderson R.F., 1983, Large particle transport of plutonium and other fallout radionuclides to the deep ocean, Nature, 303, Pages 228-231, https://doi.org/10.1038/303228a0

Lopez-Lora M., 2014, Medida de isótopos de uranio y plutonio por Espectrometría de Masas con Aceleradores de baja energía y sus aplicaciones en estudios oceanográficos, Master Dissertation, Universidad de Sevilla

Lowe D. 1980, Stromatolites 3,400-Myr old from the Archean of Western Australia. Nature, 284, Pages 441-443, https://doi.org/10.1038/284441a0

Lowe D. R., 1994. Abiological origin of described stromatolites older than 3.2 Ga. Geology, 22, Pages 387–390, https://doi.org/10.1130/0091-7613(1994)022<0387:AOODSO>2.3.CO;2

Ludwig P., Bishop S., Egli R., Chernenko V., Deneva B., Faestermann T., Famulok N., Fimiani L., Gómez-Guzmán J. M., Hain K., Korschinek G., Hanzlik M., Merchel S., Rugel G., 2016, Time-resolved 2-million-year-old supernova activity discovered in Earth's microfossil record, PNAS, 113, https://doi.org/10.1073/pnas.1601040113

Margineanu R., Simion C., Bercea S., Duliu O. G., Gheorghiu D., Stochioiu A., Matei M., 2008, The Slanic-Prahova (ROMANIA) underground low-background radiation laboratory, Applied radiation and isotopes, 66, https://doi.org/10.1016/j.apradiso.2008.04.002

Mathews G. J. & Cowan J. J., 1990, New insights into the astrophysical r-process, Nature 345, https://doi.org/10.1038/345491a0

Mauring A., Patterson S., Seslak B., Tarjan S., and A. Trinkl A., 2021, IAEA-TEL-2021-03WorldWide Open Proficiency Test Exercise, Individual Evaluation Report Part I

Maxwell S., Culligan B., 2006, Rapid column extraction method for actinides in soil, Journal of Radioanalytical and Nuclear Chemistry, 270, https://doi.org/10.1007/s10967-006-0449-2

Maxwell S., Culligan B. K., Kelsey-Wall A., Shaw P. J., 2011, Rapid radiochemical method for determination of actinides in emergency concrete and brick samples, Analytica Chimica Acta 701, https://doi.org/10.1016/j.aca.2011.06.011

Maxwell S., Culligan B.K., Hutchison J.B., Utsey R.C., McAlister D.R., 2014, Rapid determination of actinides in seawater samples, Journal of Radioanalytical and Nuclear Chemistry, 300, https://doi.org/10.1007/s10967-014-3079-0

Maxwell S., Hutchison J.B., McAlister, D.R., 2015, Rapid fusion method for the determination of refractory thorium and uranium isotopes in soil samples. Journal of Radioanalytical and Nuclear Chemistry 305, https://doi.org/10.1007/s10967-015-3972-1

McLaughlin G.C., Surman R., 2005, Prospects for obtaining an r process from Gamma Ray Burst Disk Winds, Nuclear Physics A, 758, Pages 189-196, https://doi.org/10.1016/j.nuclphysa.2005.05.036

Merz-Preiß M. and Riding R., 1999, Cyanobacterial tufa calcification in two freshwater streams: ambient environment, chemical thresholds and biological processes, Sedimentary Geology, 126, https://doi.org/10.1016/S0037-0738(99)00035-4

Mosu D., 2013, Modernizari şi dezvoltari metodice la acceleratorul electrostatic de tip tandem Van de Graaff al IFIN-HH, Doctoral Dissertation, Polytechnic University of Bucharest

Naranjo J., Ramirez C. F., Paskoff, R., 1994, Morphostratigraphic evolution of the northwestern margin of the Salar de Atacama basin, Revista Geologica de Chile, 21, Pages 91-103, https://dx.doi.org/10.5027/andgeoV21n1-a05

Pacesila D., Bishop S., **Stanciu I.**, Enachescu M., Petre A., Virgolici M., Iancu D, Ţugulan L., Done L., Petraglia A., Terrasi F., Marzaioli F., Porzio G., Buompane R., Gialanella L., 2022, Ultrasensitive detection of ^{244}Pu in environmental samples by Accelerator Mass Spectrometry, Journal of Analytical Atomic Spectrometry, Journal of Analytical Atomic Spectrometry, Accepted

Pacesila D.G., Petre A. R., Chamizo E., Rotaru A. I., State A. N., Daniel Mosu V., Virgolici M., Căta-Danil G., 2020, Preliminary results on the measurement of plutonium isotopic ratios at the 1MV AMS facility in IFIN-HH, U.P.B. Sci. Bull., Series A, 82

Pacesila D.G., 2019, Accelerator Mass Spectrometry in the Actinides Field, Doctoral Dissertation, Polytechnic University of Bucharest

Panov I. V. and Janka H.-Th., 2008, On the dynamics of proto-neutron star winds and r-process nucleosynthesis, Astronomy & Astrophysics, 494, Pages 829–844, https://doi.org/10.1051/0004-6361:200810292

Paul M., Valenta A., Ahmad I., Berkovits D., Bordeanu C., Ghelberg S., Hashimoto Y., Hershkowitz A., Jiang S., Nakanishi T., Sakamoto K., 2001, Experimental Limit to Interstellar 244Pu Abundance. Astrophys. J., 558, Pages 133–135, https://doi.org/10.1086/323617

Paul M., Valenta A., Ahmad I., 2007, An upper limit to interstellar 244Pu abundance as deduced from radiochemical search in deep-sea sediment: An account. J Radioanal Nucl Chem, 272, Pages 243–245, https://doi.org/10.1007/s10967-007-0508-3

Ratzel U., Arlandini C., Käppeler F., Couture A., Wiescher M., Reifarth R., Gallino R., Mengoni A., Travaglio C., 2004, Nucleosynthesis at the termination point of the s-process, PHYSICAL REVIEW C, 70, https://doi.org/10.1103/PhysRevC.70.065803

Reed S. J. B., Smith D. G. W., Long J. V. P., 1983, Rare earth elements in chondritic phosphates - implications for plutonium-244 chronology, Nature, 306, Pages 172–173, https://doi.org/10.1038/306172a0

Riding R., 2011, Microbialites, stromatolites, and thrombolites. In J. Reitner and V. Thiel (eds), Encyclopedia of Geobiology. Encyclopedia of Earth Science Series, Springer, Heidelberg, Pages 635-654.

Riding R., Microbial carbonates: the geological record of calcified bacterial–algal mats and biofilms, 2002, Sedimentology, 47, Pages 179-214, https://doi.org/10.1046/j.1365-3091.2000.00003.x

Riding, R. E., & Awramik, S. M., 2000, Microbial sediments Springer Science & Business Media

Riding, R., & Liang, L., 2005, Geobiology of microbial carbonates: metazoan and seawater saturation state influences on secular trends during the Phanerozoic, Palaeogeography, Palaeoclimatology, Palaeoecology, 219, https://doi.org/10.1016/j.palaeo.2004.11.018

Robinson, J. R., Rowan, J., Campisano, C. J., Wynn, J. G., & Reed, K. E. (2017), Late Pliocene environmental change during the transition from Australopithecus to Homo, Nature ecology & evolution 1, https://doi.org/10.1038/s41559-017-0159

Roche, H., Delagnes, A., Brugal, J. P., Feibel, C., Kibunjia, M., Mourre, V., & Texier, P. J., 1999, Early hominid stone tool production and technical skill 2.34 Myr ago in West Turkana, Kenya, Nature 399, https://doi.org/10.1038/19959

Saito-Kokubu Y., Yasuda K., Magara M., Miyamoto Y., Sakurai S., Usuda S., Yamazaki H., Yoshikawa S., Nagaoka S., Mitamura M., Inoue J., Murakami A., 2008, Depositional records of

plutonium and 137Cs released from Nagasaki atomic bomb in sediment of Nishiyama reservoir at Nagasaki, Journal of Environmental Radioactivity, 99, Pages 211-217, https://doi.org/10.1016/j.jenvrad.2007.11.010

Sanz-Montero M. E., Rodríguez-Aranda, J. P., & Garcia Del Cura, M. A., 2008, Dolomite–silica stromatolites in Miocene lacustrine deposits from the Duero Basin, Spain: the role of organotemplates in the precipitation of dolomite, Sedimentology, 55, https://doi.org/10.1111/j.1365-3091.2007.00919.x

Scognamiglio G., Chamizo E., López-Gutiérrez J.M., Müller A.M., Padilla S., Santos F.J., López-Lora M., Vivo-Vilches C., García-León M., 2016, Recent developments of the 1 MV AMS facility at the Centro Nacional de Aceleradores, Nuclear Instruments and Methods in Physics Research B, 375, http://dx.doi.org/10.1016/j.nimb.2016.03.033

Serban A., Albota F., Vîrgolici M., Erhan I., Tuta C., Stanciu I.M., Fugaru V., Sima O., 2021, Validation of in-house procedure for monitoring rare earth elements and lead elemental impurities in uranium materials, Journal of Radioanalytical and Nuclear Chemistry, 330, Pages 91-101, https://doi.org/10.1007/s10967-021-07926-2

SERNAGEOMIN, 2016, Reconstruction of Chaitén town, southern Chile, in a high-hazard zone. What can we do from the geological perspective? [artículos de congresos], Publicado en: Conference Cities on Volcanoes 9o., Puerto Varas, Chile, November 20-25, 2016, digital (S1.5)

Siegel D. M., Barnes J., Metzger B. D., 2019, Collapsars as a major source of r-process elements, Nature, 569, Pages 241-244, https://doi.org/10.1038/s41586-019-1136-0

Spadafora A., Perri E., Mckenzie J. A., Vasconcelos C., Microbial biomineralization processes forming modern Ca:Mg carbonate stromatolites, Sedimentology 57, https://doi.org/10.1111/j.1365-3091.2009.01083.x

Spoor, F., Leakey, M. G., Gathogo, P. N., Brown, F. H., Antón, S. C., McDougall, I., ... & Leakey, L. N., 2007, Implications of new early Homo fossils from Ileret, east of Lake Turkana, Kenya, Nature 448, https://doi.org/10.1038/nature05986

Stanciu I. M., Sava, T.B. Pacesila D.G., Gaza O., Simion C. A., Stefan B. M., Sava G. O., Ghita D.G., Mosu V., 2017, Influence of thermal treatments on radiocarbon dating of groundwater samples, AIP Conference Proceedings, 1852, Pages 080010-1-080010-5; https://doi.org/10.1063/1.4984884

Stanciu I., Pacesila D., Bishop S., Enachescu M., Petre A., Virgolici M., Serban A., Albota F., Erhan I., Fugaru. V., Iancu D., Vasile M., 2022, Status report on AMS measurements of plutonium isotopes using the 1MV Tandetron Accelerator at IFIN-HH, Nuclear Instruments and Methods in Physics Research Section B, 529, Pages 1-6, https://doi.org/10.1016/j.nimb.2022.08.006

Stan-Sion C., Enachescu M., Petre A. R., 2015, AMS analyses of I-129 from the Fukushima Daiichi nuclear accident in the Pacific Ocean waters of the Coast La Jolla – San Diego, USA, Environmental Sciences: Processes and Impacts 17, Pages 932-938, https://doi.org/10.1039/c5em00124b

Stringer, C. E., Trettin, C. C., and Zarnoch, S. J., 2016, Soil properties of mangroves in contrasting geomorphic settings within the Zambezi River Delta, Mozambique, Wetlands Ecol. Manage, 24, https://doi.org/10.1007/s11273-015-9478-3

Sukhbold T., Ertl T., Woosley S. E., Brown J. M., Janka H.-T., 2016, Core-collapse supernovae from 9 to 120 solar masses based on neutrino-powered explosions, The Astrophysical Journal, 821, https://doi.org/10.3847/0004-637X/821/1/38

Suter M., Dobeli M., Grajcar M.l, Muller A., Stocker M., Sun G., Synal H. A., Wacker L., 2007, Advances in particle identification in AMS at low energies, Nuclear Instruments and Methods in Physics Research B, 259, https://doi.org/10.1016/j.nimb.2007.01.244

Szeles E., Varga Z. and Stefank Z., 2010, Sample preparation method for analysis of swipe samples by inductively coupled plasma mass spectrometry, Journal of Analytical Atomic Spectrometry, 25, http://dx.doi.org/10.1039/b926332b

Takahashi Y., Châtellier X., Hattori K. H., Kato K., Fortin D., 2005, Adsorption of rare earth elements onto bacterial cell walls and its implication for REE sorption onto natural microbial mats, Chemical Geology, 219, Pages 53-67, https://doi.org/10.1016/j.chemgeo.2005.02.009

Tissot F. L. H., Dauphasand N., Grossman L., 2016, Origin of uranium isotope variations in early solar nebula condensates, SCIENCE ADVANCES, 2, https://doi.org/10.1126/sciadv.1501400

Trichet, J., Défarge, C., Tribble, J., Tribble, G., & Sansone, F., 2001, Christmas Island lagoonal lakes, models for the deposition of carbonate–evaporite–organic laminated sediments. Sedimentary Geology, 140, https://doi.org/10.1016/S0037-0738(00)00177-9

UNSCEAR 1982 REPORT, 1982, United Nations Scientific Committee on the Effects of Atomic Radiation. Annex E: Exposures resulting from nuclear explosions

Walker, A., Leakey, R. E., Harris, J. M., & Brown, F. H., 1986, 2.5-myr Australopithecus boisei from west of Lake Turkana, Kenya, Nature 322, https://doi.org/10.1038/322517a0

Wallis M.K., 1987, Penetration of charged interstellar dust into the solar system. Monthly Notices of the Royal Astronomical Society, 227, Pages 331–339, https://doi.org/10.1093/mnras/227.2.331

Wallner A., Faestermann T., Feige J., Feldstein C., Knie K., Korschinek G., Kutschera W., Ofan A., Paul M., Quinto F., Rugel G., Steier P., 2015, Abundance of live 244Pu in deep-sea reservoirs on Earth points to rarity of actinide nucleosynthesis, Nature Communications, 6, https://doi.org/10.1038/ncomms6956

Wallner A., Feige J., Kinoshita N. et al., 2016, Recent Near-Earth supernovae probed by global deposition of interstellar radioactive ^{60}Fe. Nature, 532, Pages 69-72, https://doi.org/10.1038/nature17196

Wallner A., Froehlich M. B., Hotchkis M. A. C., Kinoshita N., Paul M., Martschini M., Pavetich S., Tims S. G., Kivel N., Schumann D., Honda M., Matsuzaki H., Yamagata H., 2021, 60Fe and 244Pu deposited on Earth constrain the r-process yields of recent nearby supernovae, NUCLEAR ASTROPHYSICS, 372, Pages 742-745, https://doi.org/10.1126/science.aax3972

Wallner C., 2000, Beschleunigermassenspektrometrie mit Supernova-erzeugten Aktiniden, Doctoral Dissertation, Tehnical University of Munich

Wallner C., Faestermann T., Gerstmann U., Hillebrandt W., Knie K., Korschinek G., Lierse C., Pomar C., Rugel G., 2000, Development of a very sensitive AMS method for the detection of supernova-produced longliving actinide nuclei in terrestrial archives, Nuclear Instruments and Methods in Physics Research Section B, 172, Pages 333-337, https://doi.org/10.1016/S0168-583X(00)00138-5

Wallner C., Faestermann T., Gerstmann U., Knie K., Korschinek G., Lierse C., Rugel G., 2004, Supernova produced and anthropogenic 244Pu in deep sea manganese encrustations, New Astronomy Reviews, 48, Pages 145-1504, https://doi.org/10.1016/j.newar.2003.11.020

Wasserburg G.J., Busso M., Gallino R., 1996, Abundances of actinides and short-lived nonactinides in the interstellar medium: diverse supernova sources for the r-process. The Astrophysical Journal, 466, https://doi.org/10.1086/310177

Wendel C. C., Fifield L. K., Oughton D. H., Lind O. C., Skipperud L., Bartnicki J., Tims S. G., Høibråten S., Salbu B., 2013, Long-range tropospheric transport of uranium and plutonium

weapons fallout from Semipalatinsk nuclear test site to Norway, Environment International, 59, Pages 92-102, https://doi.org/10.1016/j.envint.2013.05.017

Winkler S., 2007, Accelerator mass spectrometry of heavy radionuclides with special focus on Hf-182, PhD-thesis-Canberra

Winteler C., Käppeli R., Perego A., Arcones A., Vasset N., Nishimura N., Liebendörfer M., Thielemann F.-K., 2012, Magnetorotationally driven supernovae as the origin of early galaxy r-process elements?, The Astrophysical Journal, 750, https://doi.org/10.1088/2041-8205/750/1/l22

Woosley S., Janka T., 2005, The physics of core-collapse supernovae, Nature Physics, 1, Pages 147-154, https://doi.org/10.1038/nphys172

Yamamoto M., Hoshi M., Takada J., Tsukatani T., Oikawa S., Yoshikawa I., Takatsuji T., Sekerbaev A.KH., Gusev B.I., 2001, Some aspects of plutonium in and around the former Soviet Union´s Semipalatinsk nuclear test site, Radioactivity in the Environment, 1, Pages 375-399, https://doi.org/10.1016/S1569-4860(01)80025-5

Zhao X.L., Francisco B.B.A., 2022 Matrix-assisted production of actinide molecular anions for AMS, Nuclear Instruments and Methods in Physics Research Section B 510, https://doi.org/10.1016/j.nimb.2021.10.013

Acknowledgments

At the end of this chapter, I would like to thank Prof. Shawn Bishop, as I told him in July last year, for trusting me with the responsibility of this PhD project.

We lost Shawn far too soon. He was a talented, brave, and passionate scientist that always searched for the evidence and never afraid of the unknown and unconventional ideas, like the ones necessary for this work.

I would like to thank to many other people that helped us during the last years to make this project possible:

ICP-MS group, especially to Marian Virgolici and Cosmin Pintilie for initiate me in the field of classical Mass Spectrometry and sample preparation in a clean room.

Romulus Margineanu for scientific enlightenment about natural radioactivity of actinides and secular equilibrium.

Albert Cabre-Cano, Ramon Egli and Craig Feibel, bright geologists, and friends, for helping collect the samples in the most remote places on earth and for the useful discussion in debugging the mysteries of geological structures.

Maria Farias for sampling and discussions about the modern stromatolites from Argentina.

Paul Mereuta for performing the scanning electron microscopy.

Angela, Samuel and Petra Z. for help with paperwork.

Petra Riedel for lots of help with administrative work and for always having a nice word to say.

Corina Simion for always sharing knowledge and chemicals.

Alex Baikalov, Shawn's bachelor student, for asking the right questions about everything in AMS.

Mihaela Enachescu for useful discussions about sample preparation and AMS method.

Doru Pacesila, Alex Petre, Dan Ghita, Decebal Iancu, Vasile Mosu, Mihai Straticiuc for providing support during beamtimes and help with many technical challenges.

Antonio Petraglia, Fillipo Terasi, Fabio Marzaioli, Lucio Gialanella and the rest of the AMS team of the CIRCE Laboratory, Italy for the AMS experiments.

Even if he did not contribute to this work, I am thankful to Zeno Ghizdavet, my former Master and Bachelor supervisor.

Profs. Elisa Resconi and Livius Trache for stepping in and push me in the right direction when needed.

Grandparents, Parents, and my sister, Ionela for supporting me.

I will always be grateful to Doru, my friend, husband, beamtime colleague and lab partner for always believing in me and offering unconditional support.